UNIVERSITÀ DEGLI STUDI DI TRIESTE

XXVIII CICLO DEL DOTTORATO DI RICERCA

IN NANOTECNOLOGIE

THE ROLE OF GOLD ADATOMS IN THE ELECTRONIC AND STRUCTURAL PROPERTIES OF SUPRAMOLECULAR ARCHITECTURES AT Au(111) SURFACES

Settore scientifico-disciplinare: ING-IND/22

Dottorando:

Simone VELARI

Coordinatore:

Prof. Lucia PASQUATO

Supervisore di Tesi:

Prof. Alessandro DE VITA

ANNO ACCADEMICO 2014-2015

UNIVERSITÀ DEGLI STUDI DI TRIESTE

XXVIII CICLO DEL DOTTORATO DI RICERCA

IN NANOTECNOLOGIE

THE ROLE OF GOLD ADATOMS IN THE ELECTRONIC AND STRUCTURAL PROPERTIES OF SUPRAMOLECULAR ARCHITECTURES AT Au(111) SURFACES

Settore scientifico-disciplinare: ING-IND/22

Dottorando:

Simone VELARI

Coordinatore:

Prof. Lucia PASQUATO

Supervisore di Tesi:

Prof. Alessandro DE VITA

ANNO ACCADEMICO 2014-2015

ABSTRACT IN ITALIANO

Questa tesi è focalizzata sulla studio computazionale a scala atomica delle proprietà di strutture supramolecolari all'interfaccia con superfici mediante l'uso di tecniche da principi primi basate sulla teoria del funzionale di densità (DFT). In particolare, l'attenzione viene dedicata ai diversi ruoli che un adatomo nativo di oro, sempre presente su una superficie Au(111) a temperatura ambiente, gioca nell'auto-assemblaggio di diversi sistemi molecolari. Questo lavoro ha come punto di partenza per la sua analisi lo studio dell'adsorbimento di un semplice e comune solvente, il dimetilsolfossido (DMSO); la ragione di questa scelta è che il ruolo del solvente nel processo di deposizione di molecole più complesse (ad esempio, proteine) è spesso, a torto, trascurato. Studi STM hanno infatti evidenziato come il dimetilsolfossido (DMSO), se adsorbito su Au (111), formi una serie di strutture complesse e ben definite. Il mono-strato, trovato a basse temperature, e le strutture riscontrate a temperature più alte sono stati modellizzati e ottimizzati. Le simulazioni DFT hanno mostrato che, mentre un complesso a forma quadrata viene stabilizzato dallo stesso tipo di interazione metile-ossigeno trovata nel mono-strato, le altre strutture risultano sorprendentemente stabili solamente se coordinate da uno o due adatomi di oro caricati positivamente e interagenti con gli atomi di ossigeno delle molecole di DMSO.

Nella parte seguente del lavoro, l'attenzione è stata spostata sulle porfirine, una famiglia di molecole che interagiscono attivamente con i substrati metallici e che spesso sono soggette ad auto-metallazione. In particolare lo studio è partito dalla 5,10,15,20-tetra(4-amminofenil)porfirina (TAPP), cioè una porfirina che espone quattro terminazioni amminiche. Ad alti ricoprimenti le molecole di TAPP si auto-assemblano, come fanno altri tipi di porfirine, in un mono-strato ordinato, mentre a bassi ricoprimenti formano lunghe catene. Le simulazioni

DFT hanno dimostrato che la principale causa della formazione delle catene è il comportamento anfiprotico delle molecole: ogni molecola di TAPP forma quattro legami idrogeno grazie ai gruppi amminici, e ogni molecola si comporta alternativamente o solo da donore o solo da accettore di protoni. Inoltre calcoli DFT hanno dimostrato la presenza sistematica di adatomi di oro intrappolati sotto alle molecole TAPP "accettore"; le molecole "donore" invece restano "vuote" per motivi di stabilità energetica. Infine, è stato dimostrato come la molecola "donore" possa essere manipolata sperimentalmente attraverso impulsi voltaici per rimuovere un protone dall'interno del macro-ciclo, per indurre il protone restante a "saltare" sul pirrolo opposto (tautomerizzazione) o per rimuovere entrambi i protoni. La molecola "accettore", stabilizzata dalla presenza dell'adatomo di oro, non mostra invece alcun segno di deprotonazione o di tautomerizzazione.

Nella parte restante della tesi viene infine esposto lo studio dell'adsorbimento su una superficie di oro (111) della cisteammina (CA). Questa molecola è un piccolo tiolo recentemente usata per funzionalizzare una superficie di oro attraverso il forte legame dell'atomo di zolfo col substrato e l'esposizione del gruppo amminico fuori dal piano. La fase a monostrato, pensata appunto per funzionalizzare la superficie, è stata già ampiamente studiata in letteratura. Ricerche STM a bassi ricoprimenti hanno invece evidenziato l'esistenza di strutture particolari. Simulazioni DFT hanno innanzitutto confermato l'esistenza di due configurazioni di adsorbimento concorrenti: *trans* e *gauche*. Successivamente sono stati identificati, e quindi successivamente modellizzati, tre famiglie di complessi. Due di queste sono formate esclusivamente da molecole di CA, mentre la più interessante è costituita da due molecole *gauche* unite attraverso un "ponte" formato da un singolo adatomo di oro. Questa struttura è simmetrica e chirale. In questo caso la presenza dell'adatomo induce una simmetria nella geometria di adsorbimento non presente nelle altre due famiglie di complessi.

ENGLISH ABSTRACT

This thesis focuse on the computational characterization of the atomic scale properties of supramolecular structures at a gold (111) surface, by means of ab-initio density-functional theory (DFT) techniques. Particular attentions is devoted to the different roles that native gold adatoms, always available on a gold (111) surface at room temperature, play in the self-assembly of different molecular systems.

This work has as a starting point for its analysis the adsorption study of a common and simple solvent, the dimethyl sulfoxide (DMSO); the reason for this choice is that the role of the solvent in the deposition process of more complex molecules (i.e. proteins) is often unfairly neglected. Indeed, STM experiments showed evidence that dimethyl sulfoxide (DMSO) forms complex and well-defined self-assembly structures upon surface adsorption on Au(111). The low-temperature monolayer and the high-temperature different complexes have been modeled and optimized. DFT simulations revealed that, while a square-shaped complex is stabilized by the same methyl-oxygen interactions found in the monolayer, surprisingly, all the other complexes are stable if, and only if, they are coordinated by one or two positively charged gold adatoms that interact with the oxygen atoms of the DMSO molecules.

In the next part of this work the attention has been moved to porphyrins, a family of molecules which actively interact with the metal substrate and often experience self-metalation processes. In particular, the study started from the 5,10,15,20-tetra(4-aminophenyl)porphyrin (TAPP), i.e. a porphyrin that exposes four amino terminations. Like other porphyrins, the TAPP molecules self-assemble in an ordered monolayer at high coverage, while, at low coverage, they form long chains. DFT simulations have demonstrated an amphiprotic

behavior as driving force for the chain formation: every TAPP molecule forms four hydrogen bonds, and alternately behaves as a whole H-donor or H-acceptor. Moreover, theoretical DFT calculations have demonstrated a systematic presence of a gold adatom, trapped beneath the acceptor TAPP molecule, while the donor molecules remain empty for energetic reasons. Finally, it has been shown that donor molecules can be experimentally manipulated through voltage pulses; this results in the subtraction of one proton from inside the macrocycle, in the induction of the remaining proton to jump on the other pyrrole (tautomerisation) or in the removal of both protons. On the contrary, no evidence of deprotonation or tautomerisation was observed on the acceptor molecule, stabilized by a gold adatom.

In the last part of the thesis the characterization of the adsorption of cysteamine (CA) on Au (111) is reported. CA is a small thiol recently used to functionalise the surface by exposing its amino terminations out of the surface plane and strongly binding to the gold substrate via its sulfur atom. While the monolayer phase has been already studied in literature, low coverage STM investigations highlighted the existence of peculiar structures. DFT calculations firstly confirmed the existence of two competitive adsorption configurations, *trans* and *gauche*. Then, three different cluster families have been identified. Two of them are composed only by CA molecules, while the most interesting one is composed by two *gauche* molecules linked through a single gold adatom bridge. These structures are symmetric and chiral. In this case, the presence of gold adatoms forces a symmetric adsorption geometry, which is not observed in the other two kinds of clusters.

CONTENTS

INTRODUCTION

In surface science, the self-assembly is the general principle that rules the most common approach to engine devices at the nanoscale; moreover it creates structural organization on all scales, from molecules to galaxies. This principle is defined as a process in which pre-existing parts or disordered components of a pre-existing system form regular structures or patterns.

In particular, in surface science the self-assembly is a bottom-up technique, in which the molecules spontaneously organise themselves under adequate conditions. The self-organisation is possible, due to the intrinsic self-recognition of the adsorbed molecules, whereas the size and shape of the obtained structure can be controlled by designing properly the molecules with different functionality. Most of the self-assembled structures reported in the literature are based on supramolecular chemistry: in practice, non-covalent interactions such as hydrogen bonding, van der Waals forces, etc… dominate the self-assembly process. The intermolecular interactions can be also mediated by metal atoms, so that coordination bonds between metal centres and organic ligands drive the formation of well-defined systems. These metal atoms, adsorbed on the substrate, are generally called "adatoms" and can be native if they are intrinsically originated from the metal substrate or non-native if they are foreign atoms deposited onto the substrate. Finally, the characteristics of a self-assembled structure also depend on the molecule-surface interactions; hence, by depositing the molecules on different substrates, it is possible to influence the final structure.

The main object of this study is the gold (111) surface, largely used in surface science as inert substrate. Indeed, despite its well-known "herringbone" surface

reconstruction, the gold is considered one of the most stable and less reactive metal substrate available. Nevertheless, in this thesis it will be demonstrated that also the gold substrate can deeply influence the self-assembled structures, in particular through its native gold adatoms. Indeed, the steps edges and the "soliton" of the herringbone reconstructions are, already at 250 K, sources of adatoms that can diffuse over the surface.

The Scanning Tunnelling Microscope is especially suited for the study of self-assembly of molecules deposited on conductive substrates, because it provides direct insight into the assembled complexes. However, STM images are often insufficient for a complete and exhaustive description of the adsorption. Therefore, a DFT computational approach offers a complementary technique that can integrate and better explain the experimental results.

The theoretical investigation of the molecular self-assembly aims at the understanding of the mechanisms that are involved in the complex formation. In particular, atomistic simulations can provide information on the geometry of the structures, the nature and the intensity of the interactions. In this thesis, computational DFT techniques are used to shed light on the role of gold adatoms in the self-assembly of some organic molecules on a gold (111) substrate.

This work started from the adsorption study of a common and simple solvent, the dimethyl sulfoxide (DMSO). STM experiments showed evidence that dimethyl sulfoxide (DMSO) forms complex and well-defined self-assembly structures upon surface adsorption on Au(111). Starting from the experimental STM images, a consistent model for the monolayer structure has been optimized by means of DFT simulations. This structure is actually stable only at low deposition temperatures, whereas at higher temperatures, different molecular complexes have been observed. The calculations revealed that, while a square-shaped complex is stabilized by the same kind of interactions found in the monolayer, surprisingly, all the other complexes are stable if -and only if -

they are coordinated by one or two gold adatoms that interact with the oxygen atoms of the DMSO molecules. This part of the work has been publiched in april 2015 [135].

In the next part of this work the focus has been moved to porphyrins, a family of molecules that actively interacts with the metal substrate and often experiences self-metalation processes. In particular, the study started from the 5,10,15,20-tetra(4-aminophenyl)porphyrin (TAPP), a porphyrin exposing four amino terminations. At high coverage, the TAPP molecules self-assemble in an ordered monolayer, already observed for other porphyrins, while at low coverage, they form long chains. DFT simulations show an amphiprotic behavior which acts as the driving force for the chain formation: every TAPP molecule forms four hydrogen bonds and alternately behaves as a whole H-donor or H-acceptor. Moreover, theoretical DFT calculations demonstrate a systematic presence of a gold adatoms, trapped beneath the acceptor TAPP molecules. Finally, it has been shown that donor molecules can be experimentally deprotonated through voltage pulses. On the contrary, on the acceptor molecule, stabilized by a gold adatom, no evidence of deprotonation has been observed. An article about this part of the work is already in preparation [136].

In the last part of the thesis the characterization of the adsorption of cysteamine (CA) on Au(111) is reported. CA is a small thiol recently used to functionalize the surface by exposing its amino terminations out of the surface plane and strongly binding to the gold substrate via its sulfur atom. STM investigations focused on the low coverage phase, highlighting the existence of peculiar structures. DFT calculations confirmed the existence of two competitive adsorption configurations for the single CA molecule, *trans* and *gauche*. Then, three different complex families have been identified. Two of them are composed only by CA molecules, while the most interesting one is composed by two *gauche* molecules, linked through a single gold adatom bridge. This last

structure is symmetric and chiral due to the presence of the gold adatom. An article about this part of the work is already in preparation [137].

CHAPTER 1

THEORY AND METHODOLOGY

1.1 DFT

Density functional theory (DFT) is one of the most successful and often used methods in computational physics and quantum chemistry to describe a large variety of systems such as bulk materials, interfaces, organic and inorganic molecules and up to the proteins.

The theoretical bases for the DFT are the Born-Oppenheimer (BO) approximation [1], the Hohenberg-Kohn (HK) theorems [2], according to which all properties of a system can be considered as unique functionals of its ground state density, plus the Kohn-Sham (KS) ansatz [3], which puts the HK theorem in practical use. In that way is possible to reduce the 3N degrees of freedom of the N-body system to only three spatial coordinates through its particle density. The result is an advantage for the computational costs if compared to the traditional ways which are based on the complex many-electron wavefunction, such as Hartree-Fock theory [4],[5] and its descendants. The key-element that allows accurate DFT calculations is the approximations for the exchange-correlation (XC) potential, which describes the effects of the Pauli principle and the Coulomb potential beyond a pure electrostatic interaction of the electrons. Since it is impossible to calculate the correct XC potential (by solving the many-body problem exactly), various ways of approximation have been developed. One of the first was the Local Density Approximation (LDA), based on the assumption of a slowly varying electron gas. Nowadays the standard is the so called Generalised Gradient Approximation (GGA) in which not only the

density, but also the gradient of the density enters the XC functional. The GGA functional had a great success in the describing of bulk materials, internal structure of molecules as well as adsorption of atoms and small molecules on surfaces. Nevertheless, one of the main problems of semi-local DFT is the absence of non-local correlation interactions, usually referred to as van der Waals (vdW) forces. These interactions play a crucial role in the adsorption and in the self-assembling of organic molecules on surfaces, even for chemisorbed species.

In last decades several methods that approximate the vdW interactions in DFT calculations have become available [14]-[19]. These methods include both non-local density functionals[14]-[16], which are introduced in subsection 1.2.3, and semi-empirical corrections to DFT [18], [19], which are introduced in subsection 1.2.4. In literature, a very limited number of studies comparing the different methods in an impartial approach are present, thus the choice of the best method to approach this new problem is not obvious. In the CHAPTER 4 and CHAPTER 5, tests performed through both methods are described.

1.1.1 **The Schrödinger Equation**

The time-independent Schrödinger equation describes completely all electronical properties of a system and reads:

$$H_{tot}\Psi(\{R_I\},\{r_i\}) = E\Psi(\{R_I\},\{r_i\}) \tag{1.1}$$

where $\Psi(\{R_I\},\{r_i\})$ is the total wavefunction of the system, H_{tot} is the Hamiltonian and E is the total energy of the system.

The Hamiltonian of a many-body condensed-matter system, consisting of nuclei and electrons can be written as:

$$H_{tot} = -\sum_I \frac{\hbar^2}{2M_I}\nabla^2 R_I - \sum_i \frac{\hbar^2}{2m_e}\nabla^2 r_i + \frac{1}{2}\sum_{\substack{I,J \\ I\neq J}} \frac{Z_I Z_J e^2}{|R_I - R_J|} + \frac{1}{2}\sum_{\substack{i,j \\ i\neq j}} \frac{e^2}{|r_i - r_j|} - \frac{1}{2}\sum_{I,i} \frac{Z_I e^2}{|R_I - r_i|} \tag{1.2}$$

where the indexes I, J run on nuclei, i and j on electrons, R_I and M_I are positions and masses of the nuclei, r_i and m_e of the electrons, Z_I the atomic number of

nucleus I. The first term is the kinetic energy of the nuclei, the second term is the kinetic energy of the electrons, the third term is the potential energy of nucleus-nucleus Coulomb interaction, the fourth term is the potential energy of electron-electron Coulomb interaction and the last term is the potential energy of nucleus-electron Coulomb interaction.

In principle, by solving of Schrödinger equation, everything about the system would be known. However, it is impossible to solve it in practice.

1.1.2 **Born-Oppenheimer (BO) Approximation**

A first attempt to simplify the resolution of the Schrödinger equation is the so-called Born-Oppenheimer (BO) approximation, made by Born and Oppenheimer[2] in 1927. They considered that the nuclei, much heavier than electrons, must necessarily move much slower (about two order of magnitude slower) than the electrons. Therefore they separate the movement of nuclei and electrons. Focusing on the movement of electrons, it is rational to consider the positions of nuclei fixed, thus the total wavefunction can be written as:

$$\Psi(\{R_I\},\{r_i\}) = \Theta(\{R_I\})\phi(\{r_i\};\{R_I\}) \tag{1.3}$$

where $\Theta(\{R_I\})$ describes the nuclei and $\phi(\{r_i\};\{R_I\})$ the electrons (depending parametrically on the positions of the nuclei).

With the BO approximation, Eq. (1.1) can be divided into two separate Schrödinger equations:

$$H_e\phi(\{r_i\};\{R_I\}) = V(\{R_I\})\phi(\{r_i\};\{R_I\}) \tag{1.4}$$

where:

$$H_e = -\sum_i \frac{\hbar^2}{2m_e}\nabla^2 r_i + \frac{1}{2}\sum_{\substack{I,J \\ I\neq J}} \frac{Z_I Z_J e^2}{|R_I - R_J|} + \frac{1}{2}\sum_{\substack{i,j \\ i\neq j}} \frac{e^2}{|r_i - r_j|} - \frac{1}{2}\sum_{I,i} \frac{Z_I e^2}{|R_I - r_i|} \tag{1.5}$$

and

$$\left[-\sum_I \frac{\hbar^2}{2M_I}\nabla^2 R_I + V(\{R_I\})\right]\Theta(\{R_I\}) = E'\Theta(\{R_I\}) \tag{1.6}$$

The Equation (1.4) is for the electronic problem with the nuclei positions fixed. The eigenvalue of the energy $V(\{R_I\})$ depends parametrically on the positions of the nuclei. After solving Eq. (1.4), $V(\{R_I\})$ is known and by applying it to Eq. (1.6), which has no electronic degrees of freedom, the motion of the nuclei is obtained. Eq. (1.6) is sometimes replaced by a Newton equation, according to which the forces are obtained as gradient of the potential, to move the nuclei classically.

The most important outcome of the BO approximation is to separate the movement of electrons and nuclei. This is the starting point of DFT, indeed in that way is possible to consider that electrons are moving in a static external potential $V_{ext}(r)$ formed by the nuclei.

1.1.3 **The Hohenberg-Kohn (HK) Theorems**

The density functional theory (DFT) was conceived by Hohenberg and Kohn[2] in 1964 and it was demonstrated to be an exact theory of many-body systems. It applies not only to condensed-matter systems of electrons with fixed nuclei, but also more generally to any system of interacting particles in an external potential $V_{ext}(r)$. The theory is based upon two theorems.

The HK theorem I:

The ground state particle density n(r) of a system of interacting particles in an external potential $V_{ext}(r)$ uniquely determines the external potential $V_{ext}(r)$, except for a constant.

Thus the ground state particle density determines the full Hamiltonian, except for a constant shift of the energy. In principle, all the states including ground and excited states of the many-body wavefunctions can be calculated. This means that the ground state particle density determines all properties of the system univocally.

The HK theorem II:

A universal functional G[n] of the density exists, and this is independent from the external potential $V_{ext}(r)$, so that the global minimum value of the energy functional $E[n] \equiv \int n(r)V_{ext}(r)dr + G[n]$ *is the exact ground state energy of the system and the exact ground state density $n_0(r)$ minimizes this functional. Thus, the exact ground state energy and density are fully determined by the functional E[n].*

Although HK theorems set particle density *n(r)* as the basic variable, it is still impossible to calculate any property of a system since the universal functional *G[n]* is unknown. This difficulty was overcome by Kohn and Sham [3] in 1965, who proposed the well known Kohn-Sham ansatz.

1.1.4 **The Kohn-Sham (KS) Ansatz**

It is the Kohn-Sham (KS) ansatz [3] that puts Hohenberg-Kohn theorems into practical use and makes DFT calculations possible even with a single personal computer. For this work, Kohn was awarded by the Nobel prize in chemistry in 1998.

The KS ansatz principal idea is to substitute the original many-body system by an auxiliary independent-particle system and to assume that the two systems have exactly the same ground state electron density *n(r)*. Under this hypothesis the functional *G[n]* can be divided into the kinetic energy of a system of non-interacting electrons, $T_S[n]$, and the exchange-correlation (XC) energy of the interacting system, E_{XC}:

$$G[n] \equiv T_S[n] + E_{XC}[n] \tag{1.7}$$

So the ground state energy of an electron gas with density *n(r)* in an external potential $V_{ext}(r)$ is:

$$E[n] = T_S[n] + \int n(r)V_{ext}(r)dr + \frac{1}{2}\iint \frac{n(r)n(r')}{|r-r'|}drdr' + E_{XC}[n] \tag{1.8}$$

where the external potential $V_{ext}(r)$ describes the interaction between electrons and nuclei of the system and the third term is the Hartree (or Coulomb) energy.

All terms can be determined exactly, except the exchange correlation energy $E_{XC}[n]$, which has to be approximated (see subsection 1.2).

The intention is now to minimise Eq. (1.8) with respect to the $n(r)$ under the constraint of a fixed number of electrons. In practise it has to be found an electron density that fulfils the equation

$$\frac{\delta E[n]}{\delta n(r)} = \frac{\delta T_S[n]}{\delta n(r)} + \varphi(r) + \mu_{XC}(r) = \mu \tag{1.9}$$

with

$$\varphi(r) = V_{ext}(r) + \int \frac{n(r')}{|r - r'|} dr' \tag{1.10}$$

that include all external effects and where

$$\mu_{XC}(r) = \frac{\delta E_{XC}[n]}{\delta n(r)}, \tag{1.11}$$

is the exchange correlation contribution to the chemical potential of an electron gas with density $n(r)$. Equation (1.9) is the same equation that can be obtained for a system of non-interacting electrons moving in an external potential $\varphi(r) + \mu_{xc}(n(r))$. Therefore, for given φ and μ_{xc}, it is possible obtain the electron density $n(r)$ which fulfils (1.9) by solving the one-particle time-independent Schrödinger equation

$$\left\{-\frac{1}{2}\nabla^2 + \left[\varphi(r) + \mu_{XC}(n(r))\right]\right\}\psi_i(r) = \varepsilon_i \psi_i(r) \tag{1.12}$$

with the electron density $n(r)$ given by

$$n(r) = \sum_{i=1}^{N} |\psi_i(r)|^2, \tag{1.13}$$

where N is the total number of electrons.

Equations (1.10-1.13) need to be solved self-consistently. The algorithm begins with an assumed electron density $n(r)$, from which $\varphi(r)$ and $\mu_{xc}(n(r))$ are constructed using Eq. (1.10) and (1.11), respectively. A new electron density $n(r)$ is then found from Eq. (1.12) and (1.13). For each iteration the energy is calculated as

$$E = \sum_i^N \varepsilon_i - \int n(r)\mu_{XC}(n(r))dr - \frac{1}{2}\iint \frac{n(r)n(r')}{|r - r'|} drdr' + E_{XC}[n] \tag{1.14}$$

The self-consistent loop is interrupted when the energy is converged, for example when the difference in energy from two (or more) consequent iterations is less than a break condition. The energy given by Eq. (1.14) after the last iteration is the ground state energy for the specific configuration of the nuclei.

1.2 Approximation of Exchange-correlation (XC) functional

As already said, the weak point of the DFT is the Exchange-Correlation energy term $E_{XC}[n]$ that is not determinable exactly. Several approximations have been proposed for this contribution but the two most relevant ones are the Local Density Approximation and the Generalized Gradient Approximation.

1.2.1 Local Density Approximation (LDA)

In the Local Density Approximation (LDA) a slowly varying electron gas has been assumed. The XC-energy is estimated as

$$E_{XC}^{LDA}[n] = \int n(r)\varepsilon_{XC}^{\text{hom}}(n(r))d^3r, \tag{1.15}$$

where $\varepsilon_{xc}^{hom}(n(r))$ is the XC-energy per electron for a homogeneous electron gas with density $n(r)$. This definition of the XC-energy is exact for the special case of a uniform jellium gas in which the electrons move in a uniform positive background chosen to preserve overall charge neutrality.

The homogeneous electron gas is characterised by a single parameter, r_s, and is defined as the radius of a sphere containing on average one electron:

$$r_S = \left(\frac{3}{4\pi n}\right)^{\frac{1}{3}} = \frac{1.919}{k_F} \tag{1.16}$$

where k_F is the Fermi wavevector, which for the uniform electron gas is given by

$$k_F = (3\pi^2 n)^{1/3} \tag{1.17}$$

The total XC-energy can be divided into individual contributions of exchange and correlation as

$$E_{XC}^{LDA} = E_X^{LDA} + E_C^{LDA} \tag{1.18}$$

The LDA exchange energy is given by

$$E_X^{LDA}[n] = \int n(r)\varepsilon_X^{\text{hom}}(n(r))d^3r \tag{1.19}$$

where $\varepsilon_x^{hom}(n(r))$ is the exchange energy per electron in the uniform gas given by

$$\varepsilon_X^{\text{hom}}(n(r)) = A_X n^{1/3} \tag{1.20}$$

with $A_x = -(3/4)(3/\pi)^{1/3} = -0.738$. Finally, the correlation energy is given by

$$E_C^{LDA}[n] = \int n(r)\varepsilon_C^{\text{hom}}(r_S(r))d^3r \tag{1.21}$$

where $\varepsilon_c^{hom}(r_s)$ is the correlation energy per electron of the uniform gas. $\varepsilon_c^{hom}(r_s)$ cannot be determined analytically except for the high- and low-density limits, where $r_s \to 0$ and $r_s \to \infty$, respectively. For intermediate values of r_s, accurate quantum Monte Carlo simulations have been performed on the homogeneous electron gas[6]. These results have been used to derive approximate analytical forms of $\varepsilon_c^{hom}(r_s)$ [7]-[9]. Several variants of LDA exist, among them the Perdew-Zunger (PZ) [8].

1.2.2 **Generalised Gradient Approximation (GGA)**

The other - nowadays largely used- approximation, is the generalised gradient approximation (GGA), in which the exchange term has the form

$$E_X^{GGA}[n] = \int F_X(s(r))\varepsilon_X^{\text{hom}}(n(r))d^3r \tag{1.22}$$

The factor F_x is the exchange enhancement factor, which tells how much exchange is enhanced over its LDA value. The parameter $s(r)$ is defined as

$$s(r) = \frac{|\nabla n(r)|}{2k_F n(r)} \tag{1.23}$$

Hence, as the name suggests, GGA depends not only on the electron density, but also on the gradient of the density. This type of the gradient corrected DFT is often referred to as semi-local DFT.

The full exchange-correlation energy is written as

$$E_X^{GGA}[n] = \int F_{XC}(r_S(r), s(r))\varepsilon_X^{\text{hom}}(n(r))d^3r \tag{1.24}$$

The enhancement factor has the limiting behaviours

$$F_{XC}(r_S, s=0) = F_{XC}^{\text{hom}}(r_S), \qquad F_{XC}(r_S=0, s) = F_X(s) \tag{1.25}$$

F_{XC} is often evaluated on analytical forms, which are designed to satisfy certain criterions, such as the correct uniform electron gas limit (recovering LDA for $s=0$) and the LDA linear response, or by fitting parameters to experimental data. Several variants of GGA exist, among them the Perdew-Burke-Ernzerhofer (PBE) [11]and the BLYP [12],[13] have been used in this thesis.

Generally the GGA functionals, work better than LDA when the subject of the study are organic molecules, because LDA often tends to overestimate the bond strength. Nevertheless, pure GGA functionals are not even capable to describe systems characterized by non-local interactions correctly, because they systematically underestimates bond strengths. For this reason it is often necessary to introduce a correction in DFT methods to take into account the so-called van der Waals (vdW) forces. In this work, two different approaches have been considered: a non-local density functional (vdW-DF) and a semi-empirical correction to DFT (DFT-D).

1.2.3 **The non-local density functional**

Several versions of the van der Waals density-functional (vdW-DF) exist, however in this work it has beeing exclusively used the van der Waals density functional for general geometries introduced by Dion and coworkers [14], know as Langreth-Lundqvist functional. The implementation of this functional in the

code of QuantumEspresso is based on the method proposed by Guillermo Roman-Perez and Jose M. Soler [16].

In the vdW-DF, the correlation energy is divided into two parts

$$E_c[n] = E_c^0[n] + E_c^{nl}[n] \tag{1.26}$$

The first term is treated within LDA. This is according to the authors of Ref. [14] appropriate since the second term is designed to give the non-local correlation energy, which can be expressed as

$$E_c^{nl}[n] = \frac{1}{2}\int n(r)\phi(r,r')d^3rd^3r' \tag{1.27}$$

where the kernel $\phi(r, r')$ depends on $|r - r'|$ and the densities n close to r and r'. The full derivation of the kernel $\phi(r, r')$ can be found in Ref. [14], and is based on a model response function. The detailed form of this response function is still a subject of research [17].

In the vdW-DF the E_c^{nl} term is designed to evaluate all non-local, including semi-local, contributions to the correlation energy. Hence, in the vdW-DF methodology the total *vdW-corrected* energy is given by

$$E_{vdW} = E_{GGA} - E_{c,GGA} + E_{c,LDA} + E_c^{nl} \tag{1.28}$$

where $E_{c,GGA}$ is the correlation part of the GGA XC-energy, $E_{c,LDA}$ is the correlation energy given by LDA, and E_c^{nl} is the non-local correlation energy given by Eq. (1.27). Note that the GGA correlation energy is replaced by LDA correlation plus the non-local correlation energy.

Both non-selfconsistent [14] and self-consistent implementations [15] of the vdW-DF exist. In a non-selfconsistent calculation the non-local correlation energy is calculated as a post-correction to the semi-local DFT calculation using the self-consistent GGA electron density as input.

For a self-consistent calculation the vdW-DF is included in the potential of each iteration in the self-consistent DFT calculation. The main advantage of the self-

consistent approach is that the vdW-correction is not only included in the total energies, but also in the forces.

1.2.4 **Semi-empirical "C_6-correction"**

An empirical approach to include non-local dispersion interactions in semi-local DFT is by adding pair wise interaction between all atoms in the system. The total dispersion energy for a system of N atoms is then given by

$$E_{disp}^{tot} = \sum_{i=1}^{N} \sum_{j>i}^{N} V(R_{ij}) \tag{1.29}$$

where the pair-potential $V(R_{ij})$ between two atoms i and j has the general form

$$V(R_{ij}) = -f_{damp}(R_{ij}) \frac{C_{6ij}}{R_{ij}^6} \tag{1.30}$$

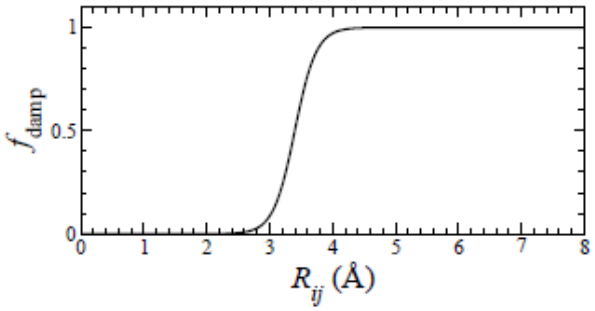

Figure 1.1: The damping function f_{damp} as function of the distance between two carbon atoms used in the Grimme correction [18]. The damping function is equal unity at large separations and zero for small separations and is used avoid divergence due to the C6 correction for small separations.

Here R_{ij} is the distance between the two atoms, C_{6ij} is the C_6 coefficient determining the strength of the interaction between the atoms and $f_{damp}(R_{ij})$ is a damping function which has the value 1 for large separations and 0 for small separations between the two atoms. The damping function is needed to avoid divergence in the energy at small distances. Several methods exists, which are useful for the application of this type of correction to DFT [18], [22] with different definitions of the damping function as well as the C6ij coefficients,

which are discussed in more detail below. Fig. 1.1 shows the damping function used in the Grimme correction [18] as a function of the distance between two carbon atoms.

The forces contributed by the C_6 correction are analytically obtained by taking the gradients of Eq. (1.30), with the force acting on atom *i* due to the interaction with atom j given by

$$F_i = -\nabla_i V(R_{ij}) = C_{6,ij} \frac{R_j - R_i}{R_{ij}^7} \left[\frac{6 f_{damp}(R_{ij})}{R_{ij}} - f'_{damp}(R_{ij}) \right] \quad (1.31)$$

Note that for periodic systems the atoms from periodic images have to be included in Eq. (1.29) for the total energy, and in a similar manner for the forces. In this thesis only the C_6-correction schemes of Grimme [18] will be used, as it is the only one recently implemented in QuantumEspresso [70].

In the Grimme scheme the $C_{6,ij}$ coefficients for dissimilar atoms are obtained from those of similar atoms pairs using combination rules, where parameters other than interaction coefficients are not involved. For homonuclear atoms the interaction coefficients are calculated from the ionisation potential, dipole polarisability and an additional parameter depending on which row in the periodic table the atom is. The chemical environments of the atoms are not taken into account. The Grimme correction has two free parameters for the damping function and one of them is chosen to a seemingly arbitrary number.

1.3 Solve the Kohn-Sham equations in practice

1.3.1 Plane wave basis set and Bloch's theorem

In density functional theory the many-body problem of interacting electrons is simplified to a problem of non-interacting electrons experiencing an effective potential *V(r)*. In other words, it is trying to solve the one-particle time-independent Schrödinger equation:

$$\left\{ -\frac{1}{2}\nabla^2 + V(r) \right\} \psi_i(r) = \varepsilon_i \psi_i(r) \quad (1.32)$$

When a system where the nuclei are arranged in a periodic structure is given, i.e. a crystalline solid, $V(r)$ is also periodic

$$V(r+R)=V(r) \tag{1.33}$$

where R is a lattice vector

$$R=n_1a_1+n_2a_2+n_3a_3 \tag{1.34}$$

Here n_1, n_2 and n_3 are integers, and a_1, a_2 and a_3 are the three unit cell vectors of the system. Our first assumption is that the system is confined into a large volume Ω which consists of N primitive unit cells with volume Ω_C, so that $\Omega = N\Omega_C$.

According to Bloch's theorem, a wave function of such a periodic system can be written as a product of a plane wave function and a periodic function, $u_k(r)$, with the same periodicity as the potential

$$\psi_k(r)=u_k(r)e^{ik\cdot r} \tag{1.35}$$

from which it follows that

$$\psi_k(r+R)=\psi_k(r)e^{ik\cdot R} \tag{1.36}$$

Here, k is a wavevector in the first Brillouin zone and attains N discrete values due to the periodic boundary conditions over the large volume. The physical meaning of the Bloch's theorem is that the wave functions at positions r and $r+R$ are the same except for the phase factor $exp(ik \cdot R)$, and more importantly, the electron density $n(r)$ has the same periodicity as the potential.

The periodic function $u(r)$ can be expanded in terms of plane waves

$$u_k(r)=\sum_G c_k(G)e^{iG\cdot r} \tag{1.37}$$

Due to the periodicity of $u(r)$ only the reciprocal lattice vectors enter the expansion, which are defined as

$$G=\sum_i m_i b_i \tag{1.38}$$

where m_i are integers and b_i are the basis vectors of the reciprocal lattice. Note that the reciprocal lattice vectors are so defined that they fulfil $R \cdot G = 2\pi l$, where l is an integer. The full wave function can then be written as

$$\psi_k(r) = \sum_G c_k(G) e^{i(k+G)\cdot r} \tag{1.39}$$

The periodic potential can also be expanded in plane waves

$$V(r) = \sum_G V(G) e^{iG\cdot r} \tag{1.40}$$

By insertion of Eq. (1.39) and (1.40) into Eq. (1.32) the following eigenvalue problem is obtained

$$\sum_{m'} H_{mm'}(k) c_k(G_{m'}) = \varepsilon(k) c_k(G_m) \tag{1.41}$$

The original problem has been transformed to N independent equations, one for each k-point in the first Brillouin zone. The matrix elements of the Hamiltonian are given by

$$H_{mm'} = \frac{|k+G_m|^2}{2}\delta_{mm'} + V(G_m - G_{m'}), \tag{1.42}$$

By diagonalization of the Hamiltonian a set of discrete eigenvalues $\varepsilon_n(k)$ together with their corresponding eigenvectors $c_{n,k}$ are obtained, one for each k-value. The label n for the different eigenvalues is the band index and the energy eigenvalue for the electrons in the periodic potential defines the band structure $\varepsilon_n(k)$.

Equation 1.41 can be solved numerically when the number of plane waves is truncated. This is done by introducing a kinetic energy cut-off, often referred to as the plane wave cut-off defined as

$$\frac{|k+G_m|^2}{2} < E_{cutoff} \tag{1.43}$$

The convergence of the solution is controlled by varying the value of the plane wave cutoff E_{cutoff}. The convergence is also controlled by the number of k-points included in the calculations. In practice only a few k-points of the first Brillouin zone are included and the actual number required for the convergence of the

total energy depends on both on the size and the type of the system under study. Several methods exist for generating the *k*-points in the first Brillouin zone, the most common one being the Monkhorst-Pack scheme [23].

The plane wave basis set requires periodic boundary conditions in all the three real-space coordinates. The method is however not restricted to the study of periodic structures. The periodic supercell can be designed so that when applying the periodic boundary conditions, the interactions between supercells in certain dimensions are made negligible by adding a vacuum region.

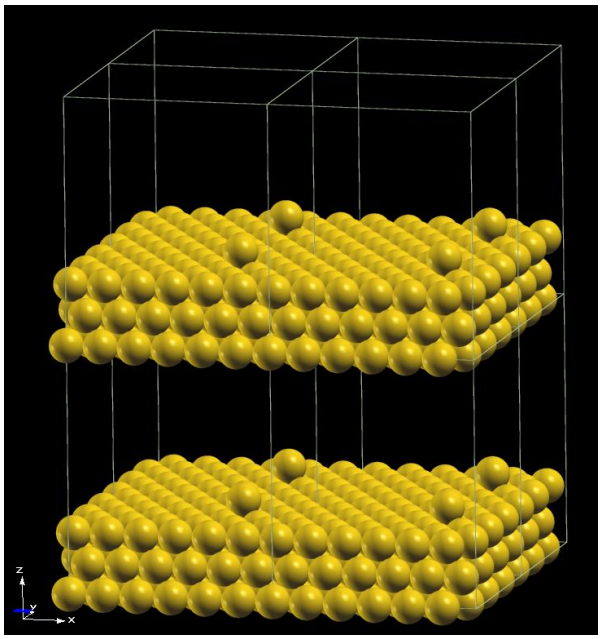

Figure 1.2: Illustration of the supercell approach for gold adatom adsorbed on Au(111) slab. The vacuum region between slabs prevent interactions between periodic images in the direction perpendicular to the surface. Furthermore, the size of the surface unit cell prevents interactions between adatoms of periodic images. The boundaries of the periodic supercell are indicated by white lines.

The principle is illustrated for a single Gold adatom adsorbed on Gold(111) in Figure 1.2. The gold substrate is modelled by a slab of three gold layers. A vacuum region is used to prevent the slab to interact with its periodic images (perpendicular to the surface). Furthermore, the surface unit cell should be chosen to be large enough to prevent interaction of the adatom with its periodic images.

1.3.2 **Pseudopotentials**

All pseudopotential approaches are based on the frozen core approximation. In this approximation the effect of the local chemical environment on core-electrons is assumed to be weak and treated by first order perturbation theory. Therefore, the wave functions of the core-electrons are frozen and equal to those of the isolated atom. Only the valence electron wave functions are updated during the self-consistent iterations. Due to the requirement of orthogonality, valence wave functions have rapid oscillations in the core region of the core wave functions. Outside this core region, the core wave functions are essentially zero, which results in much smoother valence wave functions in this region. To treat the rapid variation of the valence wave functions in the core region a large number of plane waves are needed for convergence. To overcome this problem one strategy is the use of a pseudopotential, in which the interactions of the valence electrons with the nuclei and the core-electrons are described by an effective, much weaker potential. The resulting pseudo-wave functions are smooth inside the core region and are equal the real wave functions outside the core region. The number of plane waves required to describe the pseudo-wave functions is much less than for the real wave functions, allowing a much easier computation of Eq. (1.41).

Several different pseudopotentials exist. In this thesis, due to the significant size of the systems studied, ultra-soft pseudopotentials [69] have been used in order to calculate the plane waves presented which are here reported.

1.4 The calculation code

The calculation code used for this work is *PWscf (Plane-Wave Self Consistent Field)*. It is a set of programs for electronic structure calculations within density functional theory, using plane wave basis sets and pseudopotentials. The software is released under the GNU General Public License. *PWscf* is included in the suite *Quantum ESPRESSO* (QE) [24], which provides several tools for the

study of condensed matter systems. *Quantum ESPRESSO* contains also all the tools necessary for the Post Processing, from the possibility to obtain the Projected Density of States (PDOS) for single atoms to the simulation of STM images.

1.5 The Data Centres

All the calculations required for this thesis, as many of those concerning the quantum simulation of complex systems, require large computational power. That is the reason why the calculation cannot be run on local machines but they have to be submitted to data centres specialised in High Performance Computing (HPC). The machines that have been used for the realisation of this thesis are listed below.

1.5.1 **Cineca – FERMI BG/Q cluster**

FERMI is a highly qualifying system for Computational Sciences; it allows Italian and European research teams to conduct frontier research projects for the solution of fundamental problems in science and engineering that require enormous computing power. It has been used only for the calculation that required a large computing power.

Architecture	10 BGQ Frame
Processor	IBM PowerA2, 1.6 GHz
Number of cores	163840
Total Ram Memory	160 TB
Number of Nodes	10240
Processors for Node	16
Memory for Node	16 GB

Table 1.1: Technical data of Fermi BG/Q Cluster

1.5.2 **Cineca – PLX cluster**

PLX was a "hybrid" (CPU +GPU) supercomputer which was definitively shut down in 2015. It has been used for the calculation that didn't require a large computing power.

Architecture	Linux Infiniband Cluster
Processor	six-cores Intel Westmere 2.40 GHz
Number of processors	548
Total Ram Memory	12.8 TB
Number of Nodes	274
Processors for Node	2
Memory for Node	48 GB
Operative System	Red Hat RHEL 5.6

Table 1.2: Technical data of PLX cluster.

1.5.3 **King's College London –*ADA* cluster**

ADA is a new big cluster, hosted by King's College London, which was inaugurated in 2014. It has been largely used for most of the calculations.

Architecture	Linux Infiniband Cluster
Processor	Intel E5-2650v2, 2.6Ghz, 8 cores
Number of processors	136
Total Ram Memory	4.2 TB
Number of Nodes	68
Processors for Node	2
Memory for Node	64 GB
Operative System	CentOS - enterprise Linux distribution

Table 1.3: Technical data of ADA cluster.

1.5.4 **King's College London –*CAPABLANCA* cluster**

CAPABLANCA was a small and old cluster, hosted by King's College London, which was definitively shut down in 2014. It has been largely used for all the preliminary test phase.

Architecture	x86_64
Processor	Intel Xeon 5150 2.6 GHz
Number of processors	480
Total Ram Memory	960 GB
Number of Nodes	120
Processors for Node	4
Memory for Node	8 GB
Operative System	ClusterVision OS 3 on top of Scientific Linux 4

Table 1.4: Technical data of Capablanca Cluster

1.6 The graphic software

For an easy interpretation of the results, it's used the software XCrysDen[25]. This tool reads input and output files to create a three-dimensional system of atoms, allowing not only a preventive control of the correctness of the input file but also permitting a fast and intuitive interpretation of the results. By mean of XCrysDen, it is possible to measure distances between atoms and angles between bonds. Residual forces on atoms can also be displayed. Finally is possible to analyze and plot the results of the Post-Processing (like charge transfer calculation) and display molecular orbitals. All 2D and 3D models contained in this thesis were obtained by mean of the program XCrysDen.

CHAPTER 2

EXPERIMENTAL TECHNIQUES

The aim of this chapter is to provide a brief introduction to the principles of the different experimental characterisation techniques which are the background of the experimental results presented with our theoretical results in Chapter. It will also be discussed how the quantities measured in the different experiments can be evaluated within density functional theory as well as how the theory is related to the experimental observations.

2.1 Scanning tunnelling microscopy (STM)

The scanning tunneling microscope is a non-optical microscope that scans an electrical probe (or "tip") over a conductive surface to be imaged (Figure 2.1). Since its invention in 1981 by Gerd Binnig and Heinrich Rohrer [26], the scanning tunneling microscope (STM) has had a great impact on surface science for allowing the study of surfaces and molecules on atomic scale.

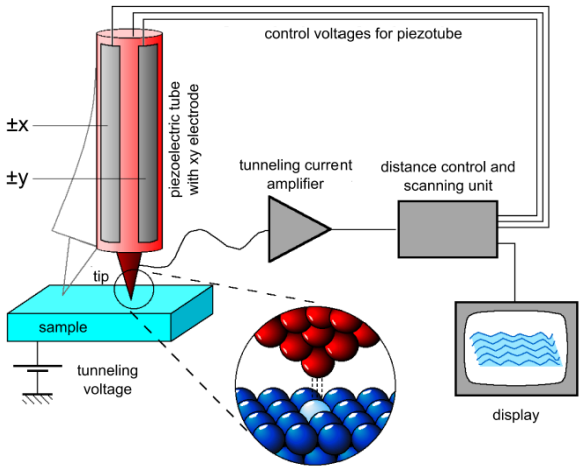

Figure 2.1: Scheme of a Scanning tunnelling microscope (STM)

In an STM the metal tip is approached very closely (~10 °A) to a (semi) conducting surface and a bias voltage is applied between the tip and the surface. Although the bias voltage would not classically allow the electrons to overcome the potential barrier between the tip and surface, quantum mechanics introduces a small probability of tunnelling between tip and sample. The basic principle behind the quantum tunnelling is illustrated in Figure 2.2, where a particle with mass m and energy level E tunnels through a square potential V. The probability to tunnel that has an electron is given approximately by

$$P \propto e^{\left[-d\frac{\sqrt{2m(V-E)}}{\hbar}\right]} \tag{2.1}$$

where d is the width of the barrier, E is the energy of the particle, V is the height of the potential barrier. The tunnelling probability, together with the resulting tunneling current in STM, decays exponentially accordingly to the width of the potential barrier, which is related to the distance between tip and sample in the STM setup. The tunnelling probability decreases by an order of magnitude when increasing the tip-surface distance by 1 °A. Therefore, considering the exponential behaviour of the tunnelling probability it is possible to achieve spatial resolution on the atomic scale, with direction perpendicular to the surface. [30]

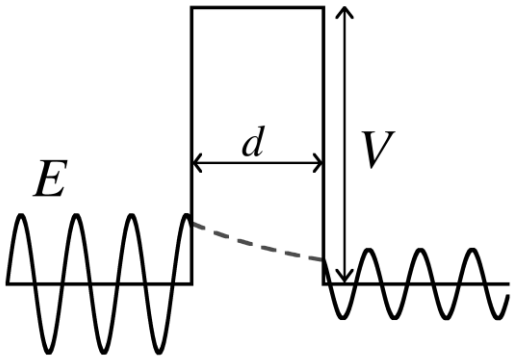

Figure 2.2: Electron with energy E tunnelling through a potential barrier V>E of width d. The probability of the tunnelling is given by Eq. (2.1).

According to first order perturbation theory the tunnelling current from the tip to the sample is given by Fermi's golden rule as

$$I = \left(\frac{2\pi e}{\hbar}\right)\sum_{\mu\nu}\left\{f(\varepsilon_\mu)\left[1-f(\varepsilon_\nu+eV)\right]-f(\varepsilon_\nu)\left[1-f(\varepsilon_\mu+eV)\right]\right\}\times\left|M_{\mu\nu}\right|^2\delta(\varepsilon_\mu-\varepsilon_\nu) \quad (2.2)$$

where $f(\varepsilon)$ is the Fermi function, V is the applied voltage, $M_{\mu\nu}$ is the tunnelling matrix element between states ψ_μ of the probe and ψ_ν of the sample and ε_μ is the energy of state ψ_μ in the absence of tunnelling.

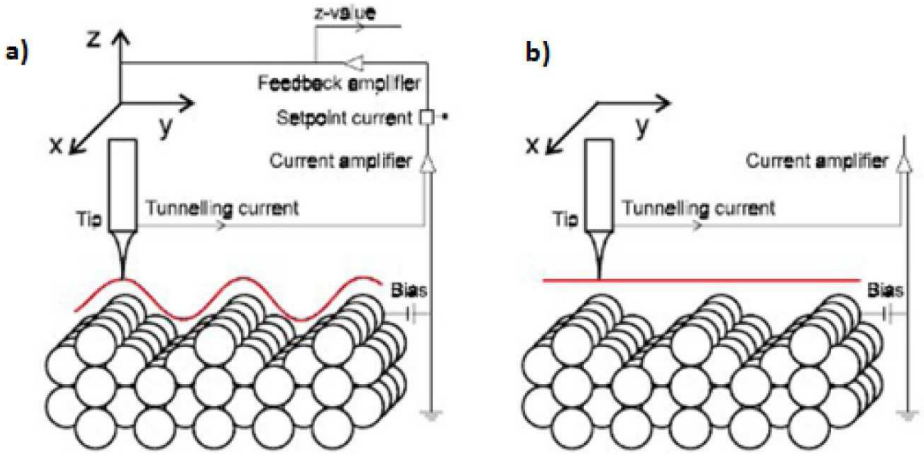

Figure 2.3: (a) Scheme of "constant current" scanning mode and (b) scheme of "constant height" scanning mode [31].

Under the hypothesis that the tip has a constant density of state, the tunnelling current depends on the electronic structure of the sample, as well as on the distance between tip and sample. The tip is scanned on a region of the surface with displacements of the order of Angstroms, thanks to a piezoelectric cylinder. The STM images are formed translating in gradation of colour the height of the tip or the variation of the current, measured at a fixed height. Indeed there are two different modes with which the STM can operate. In the first of these (see Figure 2.3(a)), the "constant current" mode, an electronic feedback system maintains a constant tunneling current by varying the vertical position of the tip during the scan of the surface. Thus images are formed by scaling appropriately, in order to reproduces the "topography" of the sample. In the second mode, the STM operates at constant height, as shown in Figure

2.3(b), in which the vertical position of the tip is maintained constant. Images are rendered giving a gradation color value of the point by point tunneling current. This second operating mode allows faster scans because don't need the electronic feedback system, but the counterpart is that the tip is not protected from impact against the roughness of the surface.

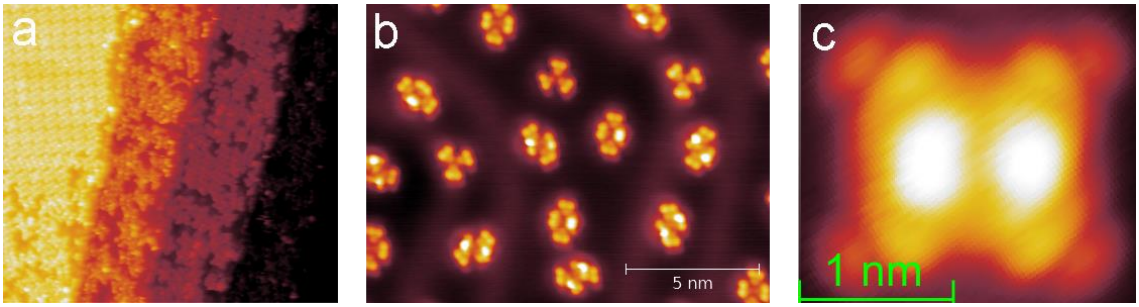

Figure 2.4: STM images of (a) self-assembled TAPP monolayer on Au(111) (40.0x33.8 nm^2), (b) DMSO complexes on (Au)111 and (c) detail of a TAPP adsorbed on Au(111).

Figure 2.4 illustrate both aspects. In Figure 2.4(a) is highlighted the terrace structure of an Au(111) surface covered by a monolayer of TAPP molecules: in this case the main contrast difference is caused by a different height of the substrate. The bright protrusions in Figure 2.4(b) is caused by the presence of ~~are~~ molecules of DMSO which change both topography and electronic structure compared to the metal substrate. Finally, using LT-STM, in which the tip-sample system is cooled down even to the liquid helium temperature (4 K) it is possible to observe the molecular orbitals, which are illustrated in Figure 2.4(c). Therefore attention should be paid in order to directly connect the contrast in images to a topographical feature of the surface, particularly in presence of adsorbed molecules. Indeed the STM is only sensitive to the local density of states (LDOS) of the sample around the Fermi level, not to the total density of charge. This difference can be neglected when measuring a clean metal surface, but not when it is covered with adsorbates, whose electronic states can change drastically the LDOS of the surface. The above mentioned observations also indicate that the main limitation of the STM is its inability to show a purely

chemical contrast. In other words, the identification of species of atomic or molecular adsorbates or the chemical composition of complexes on a surface, through the images is not possible. To obtain this kind of information, it is necessary to perform ab-initio DFT simulations to find a satisfactory theoretical model; thus simulation of the relative STM images should be performed, in order to compare those images with the experimental ones.

2.1.1 The Tersoff-Hamann approximation

From the Bardeen's approximation [27] of the matrix elements $M\mu\nu$ in Eq. (2.2) and by assuming a spherical tip, it can be shown can show that the tunnelling current is proportional to the local density of states (LDOS) of the sample

$$I(V,\vec{r}_0) \propto \int_{\varepsilon_F}^{\varepsilon_F + eV} \rho(\varepsilon,\vec{r}_0)d\varepsilon \tag{2.3}$$

and the first derivative of the tunnelling current is given by

$$\frac{dI}{dV}(V,\vec{r}_0) \propto \rho(\varepsilon_F + eV,\vec{r}_0) = \sum_{\alpha} |\psi_\alpha(\vec{r}_0)|^2 \delta(\varepsilon_F + eV - \varepsilon_\alpha), \tag{2.4}$$

where $\rho(\varepsilon_F + eV,\vec{r}_0)$ is the LDOS at point $\vec{r}_0$ and energy $\varepsilon_F + eV, \psi_\alpha(\vec{r}_0)$ are the wavefunctions of the sample. This is the Tersoff-Hamann approximation [28], [29] which has been used in all STM simulations within this thesis.

In DFT the wave functions in Eq. (2.4) are given by the Kohn-Sham wave functions. In the STM simulations the wave functions have been extrapolated far away from the surface by an exponentially decaying function where the matching distance was determined at a height above the surface where the electrostatic potential becomes constant, corresponding to the vacuum region.

The data obtained with the post-processing tool included in the Quantum Espresso package simulate an STM image taken into "constant height" mode. Thus, to allow a better comparison between simulation and experiments, every simulated STM image present in this thesis has been elaborated with a dedicated script to simulate a better image, taken at "constant current" mode.

2.2 X-ray Photoelectron Spectroscopy (XPS)

X-ray Photoelectron Spectroscopy is a quantitative spectroscopic technique. XPS spectra are obtained by irradiating a material with a beam of x-rays while simultaneously measuring the kinetic energy and number of electrons that escape from the irradiated material. XPS as a surface chemical analysis technique can be used to analyze the chemistry of the surface from a material in its natural state. This technique is also used to measure the elemental composition of the surface or the empirical formula of pure materials. The chemical or electronic structure of each element in the surface is revealed as well; therefore this feature is useful for an accurate study of the electronic state of the adsorbates and for the investigation of bond formation between adsorbates and between adsorbates and substrate. Since the core levels are very sensitive to the local electrostatic potential, XPS can be used to determine the local chemical environments that an atom experiences in a molecule. A XPS spectrum is a plot of the number of detected electrons versus the binding energy of the electron. Each element produces a characteristic set of XPS peaks at a characteristic binding energy. The number of detected electrons in each of the characteristic peaks is directly related to the amount of the element present. The XPS is not sensitive to the presence of hydrogen, thus its presence has to be estimated by means of the electronic state of the other elements.

2.3 Near Edge X-ray Adsorption Fine Structure (NEXAFS)

Near Edge X-ray Adsorption Fine Structure (NEXAFS) is an electron spectroscopy technique with high sensitivity to bond angles, bond lengths and the presence of adsorbates. The great advantage of this technique derives from its elemental specificity. Since the various elements have different core-level energies, NEXAFS permits extraction of the signal from a surface monolayer

and it can also determine the chemical state of the various elements. For this reason it is widely used in surface science. The fundamental phenomenon underlying NEXAFS is the adsorption of an x-ray photon by a core-level of an atom in a solid and the consequent emission of a photoelectron. The resulting core hole is filled either via an Auger process or by the capture of an electron from another shell followed by emission of a fluorescent photon. The difference between NEXAFS and traditional photoemission is that in photoemission the initial photoelectron itself is measured, while here the fluorescent photon or Auger electron or an inelastically scattered photoelectron may be measured.

CHAPTER 3

THE GOLD (111) SURFACE

Metal surfaces are commonly used as substrate for the self-assembly of different kind of molecules and are the favorite support for imaging with STM. The substrate plays often an active role in the assembly process, modifying drastically the characteristics of the complex formed. Some metals like copper are known for their reactivity, other like gold for their inactivity. The gold, in particular with the (111) surface orientation, is considered one of the most stable and inert substrate, despite the "herringbone" reconstruction that involves the first layers of the surface. For this reason gold is the most widely used substrate for the study of self-assembled monolayers [32][33].

In this work we'll demonstrate that the Au (111) surface is not completely inert, but interacts decisively with different molecules, in particular through native gold adatoms, always present on the surface at temperature higher than 250 K.

In this chapter it is described the procedure followed to faithfully reproduce a gold (111) substrate. Initially the crystalline structure of gold (FCC, Face Centred Cubic) has to be reproduced. This has been followed by the optimization of the lattice constant, i.e. finding the value that minimize the energy of the system. After that, a unit cell that reproduces a (111) surface has been replicated in the three dimensions until a slab composed by three atomic layers has been generated. The height of the cell has been expanded along z, to eliminate the periodicity along that axis and to generate in this way a real surface of gold. To simulate the presence of the bulk below the surface, the lower atomic layer coordinates have been fixed. Finally the adsorption site and energy of a gold adatom have been studied.

3.1 The gold surface reconstruction

The Gold is a face-centred cubic (fcc) crystal with lattice constant a = 4.08 Å. The surface of the crystal used is the (111), which has hexagonal structure with a periodicity equal to $a/\sqrt{2}$ = 2.88 Å.

The surface (111) of gold does not exhibits, however, a perfect hexagonal pattern because of its characteristic reconstruction. Gold is a unique case since it's the only *fcc* metal that reconstructs on its (111) surface. As can be observed in the image STM shown in Figure 3.1, the surface (111) it is characterized by the presence of pairs of parallel lines which vary the direction of 120 ° each about 250 Å. This particular structure, observable also on a larger scale, is called "herringbone" and the points where the pairs of parallel lines change their direction, drawing the classic "zigzag" features on the surface, are referred to "elbows".

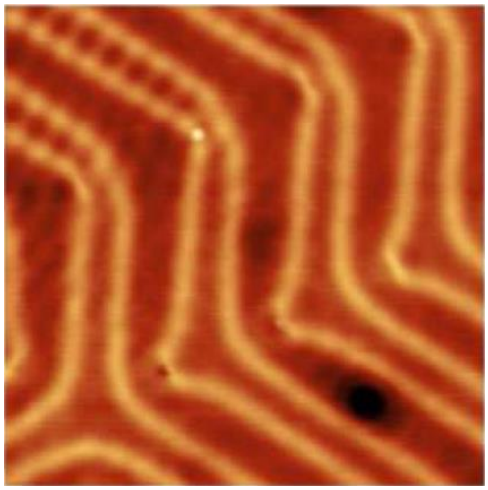

Figure 3.1: STM image of gold (111) surface at 4 K. Scansion area 25x25 nm^2. Scansion parameters: V_{sample}=1V e $I_{tunneling}$=0,2 nA [34].

This structure extends on terraces, separated by monatomic steps of about 2.4 Å. The dimension of the terraces varies from few tens to few hundreds of nanometers different zones of the sample. The reconstruction is characterized by the gradual displacement of atoms along the direction $[1\,\bar{1}\,0]$ from fcc to hcp sites (see Figure 3.2). As a result of this displacement the reconstructed (111)

surface is composed by a rectangular unit cell (22 x √3) with primitive vectors of 63 Å in the $[1\bar{1}0]$ direction and 4,7 Å in the $[1\bar{2}0]$ direction [35], [36].

In addition, as evidenced by the different contrast in the STM image in the Figure 3.2(a), the gold (111) has a vertical corrugation due to the different height of the atoms in different regions. The vertical corrugation has been estimated by Barth et al. in 0.20±0.05 Å [35]. This parameter is measured between the largest region of minimum, which corresponds to the fcc sites, and the brighter region at maximum height, which corresponds to the transition strips (where the atoms are neither in a hcp nor in a fcc site).

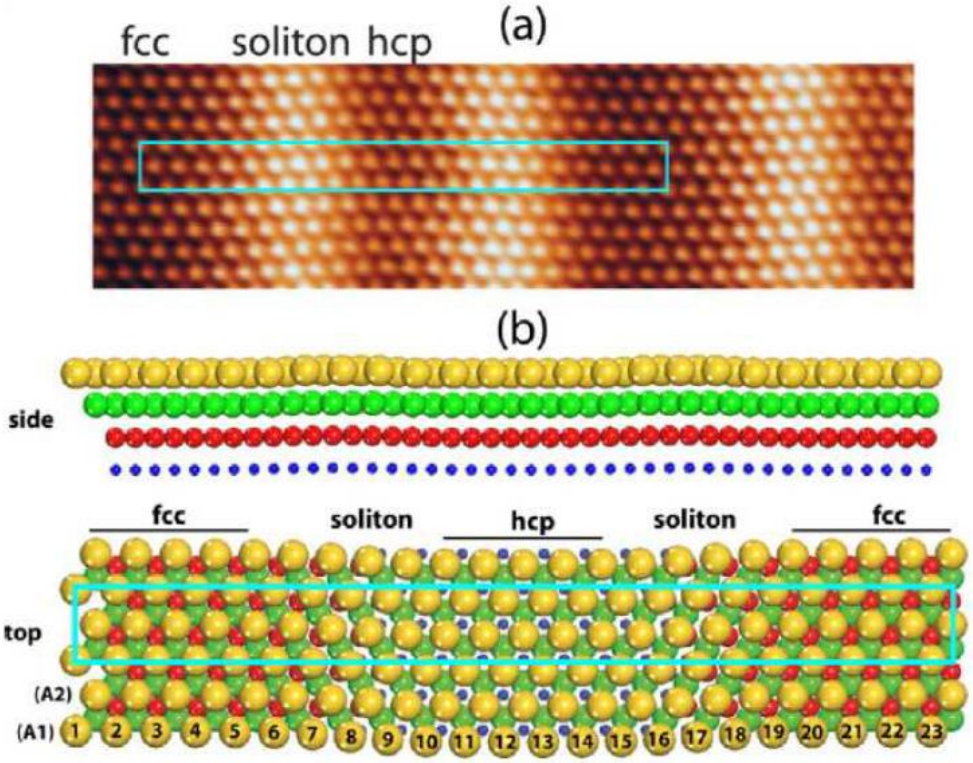

Figure 3.2: Reconstruction (22 x √3) of the surface (111) of gold. (a) STM image with atomic resolution highlighted in blue with the primitive cell rectangular 22 x √3. (b) Model of the structure of the primitive cell. Within the cell a pair of transition strips is present, i.e. solitons, where the atoms are not in a hcp neither in fcc site. The region within the two solitons, which are distant from them about 21 A, has hcp structure. The regions which are external to the solitons have the fcc structure; the wings with these structure, that separate two pairs of consecutive solitons on the surface, have a width of about 34 Å[37].

3.2 Computational modelling

The first step in the accurate modelling of the different adsorption systems studied in this thesis, was to reproduce accurately the gold substrate. As seen in the previous paragraph, the real Au(111) surface is not completely flat due the "herringbone" surface reconstruction. Thus, in principle, in order to obtain a correct surface model, it is necessary to take into account the first layer displacement. However in practice this is not possible, since the dimension of the unit cell in the reconstructed surface is too large for the computational power available. For this reason it is common practice in DFT calculations to use an unreconstructed Au(111) surface as substrate. For this thesis, in particular, this approximation is more than enough, because all the molecules studied adsorb only in the *fcc* regions of the gold reconstructed surface. Before the (111) surface was created, it was however necessary a test phase to verify the physical correctness of the model for all the different pseudopotential used in this work.

3.2.1 **The gold bulk model**

The main objective of this preliminary phase was to obtain an optimized lattice constant "b" for gold. A trigonal elementary cell with one gold atom (see Figure 3.3) has been chosen to reproduce the *fcc* lattice.

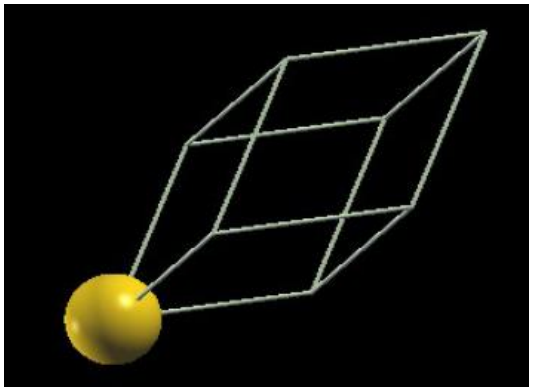

Figure 3.3: trigonal elementary cell containing a single gold atom. This cell, replicated in the three spatial dimensions generates an *fcc* lattice.

Then the lattice constant has been varied until a minimum for the total energy has been reached.

In the table 3.1 displays the results for the lattice constant obtained with different pseudopotentials compared with the experimental one. The relative error is lower then 3% in every case for the PZ, the PBE and the PBE+Grimme.

Pseudopotential	b [Å]	error (%)
Experimental value	2.88	-
PZ	2.82	-2.08
PBE	2.96	+2.78
PBE + vdW-DF	3.09	+7.29
PBE + Grimme	2.84	-1.38
BLYP	3.00	+4.17

Table 3.1: Calculated lattice constant for gold with different pseudopotentials.

Subsequently the Bulk modulus of the model has been calculated, to evaluate the physical properties of the simulated gold crystal. The bulk modulus B is defined as the increase in pressure necessary to have a certain volumetric strain [38]:

$$B = \frac{-dp}{\left(\frac{dV}{V}\right)} \tag{3.1}$$

and it is linked to the second derivative of the energy from the relation

$$B = VE''(V) \tag{3.2}$$

For small deformations, the energy can be expressed as function of the volume with a Taylor expansion near V_0 (non-deformed volume which corresponds to the minimum energy):

$$E(V) = E_0 + \frac{1}{2}\frac{B}{V_0}(V - V_0)^2 \tag{3.3}$$

Once the minimum energy lattice constant is known, it is possible to deform the crystal around that value to obtain a set of values for the energy that can be

plotted as a function of the volume V. The resulting curve can be interpolated with a least-squares parabola

$$E(V) = aV^2 + bV + c \tag{3.4}$$

Combining the equation (3.2), (3.3) and (3.4), the result is

$$B = \left(V \frac{\partial^2 E}{\partial V^2} \right)_{V=V_0} = 2aV_0 \tag{3.5}$$

For each pseudopotential a graph E(V) vs. V has been produced to obtain with the formula (3.5) the different bulk moduli. In table 3.2 the results are summarised. The pseudopotential that shows the smaller error are the PZ and the PBE+Grimme.

Pseudopotential	B [GPa]
Experimental value	220
PZ	197
PBE	154
PBE + vdW-DF	106
PBE + Grimme	190
BLYP	114

Table 3.2: Calculated lattice constant for gold with different pseudopotentials

3.2.2 **Simulation of a Gold (111) surface**

After having defined an optimized lattice constant for every pseudopotential, the trigonal elementary cell has been substituted with one orthorhombic with 6 gold atoms, more suitable to generate a gold (111) surface (see Figure 3.4).

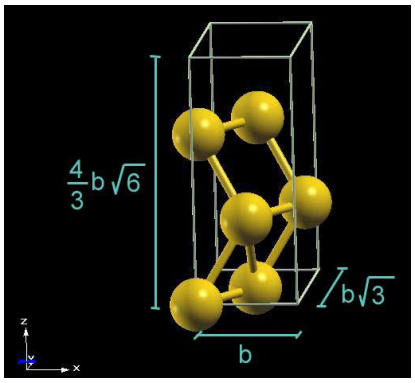

Figure 3.4: Orthorhombic elementary cell containing 6 gold atoms.

Now the elementary cell can be reproduced in three dimensions till the size required by the system in study is reached. After that, it is necessary to introduce enough space over the gold slab to avoid the interactions between the repetitive images. For the same reason the gold surface has to be large enough to avoid lateral interactions between the adsorbed system and its periodic images (see Figure 3.5).

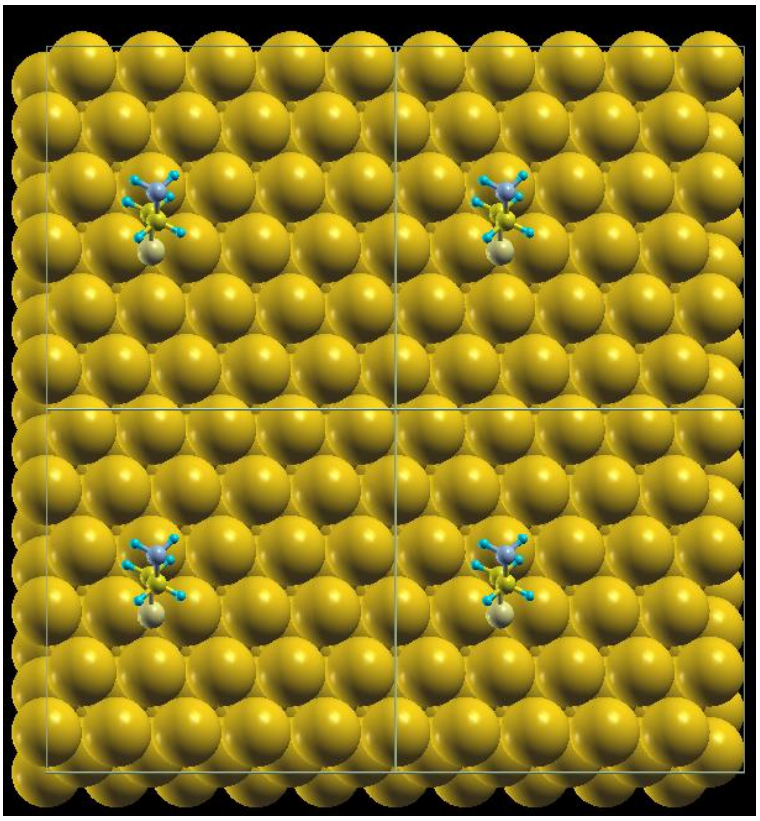

Figure 3.5: Illustration of the supercell approach for CA molecule adsorbed on Au(111) slab. The size of the surface unit cell prevents interactions between the molecules of periodic images. The boundaries of the periodic supercell are indicated by white lines.

One last step is necessary to prepare the surface for the "deposition" of the required molecules: in order to simulate the presence of the bulk under the three gold layers, the lower layer is fixed. Afterwards, the gold substrate has to be relaxed to avoid the presence of residue tensions.

3.3 Native gold adatoms

On the Au(111) surface, low-coordinated atoms are natively available, since the higher density of gold atoms in the first atomic layer induces a periodic displacement of the atoms out of the surface plane along the soliton walls of the herringbone reconstruction. On this surface, extraction and stabilization of native gold adatoms can be induced by interaction of organic molecules with the Au(111) surface, as observed for instance with molecules containing cyano (CN) groups [106]-[108], porphyrin or phthalocyanine derivatives[73],[105], and molecules containing very electronegative substituents such as sulfur [110],[111]. For this reason, a preliminary study about the adsorption site of a native adatom has been carried out on a clean Au (111) surface. The DFT calculations confirmed the "hollow" position as the most stable for an adatom. Moreover, the two possible *hollow* positions (*fcc* and *hcp*), differing for only 7 meV, can be considered isoenergetic.

CHAPTER 4

SELF-ASSEMBLY OF DMSO ON GOLD (111)

4.1 Summary

In this chapter the study about the formation of dimethyl sulfoxide (DMSO) molecular complexes on Au(111) is reported; this complex is enabled by native gold adatoms, unusually linking the molecules *via* a bonding of ionic nature. This interaction yield a mutual stabilization between molecules and adatom(s). DMSO is a widely used polar, aprotic solvent whose interaction with metal surfaces is not fully understood. Starting from X-ray photoelectron spectroscopy and low temperature scanning tunnelling microscopy data, density functional theory (DFT) calculations have been used to show that DMSO molecules form complexes made by up to four molecules, arranged with adjacent oxygen terminations. In particular, after a brief introduction on DMSO molecule, the STM, XPS and NEXAFS results are exposed. Afterwards, the presentation of the technical aspects of the calculations and finally the results of the computational study will be illustrated. DFT calculations reveal that most of the observed structures are accurately reproduced if, and only if, the negatively charged oxygen terminations are linked by one or two positively charged Au adatoms. A similar behaviour was previously observed only in nonstoichiometric organic salt layers, fabricated using linkage alkali atoms and strongly electronegative molecules. These findings provide nanoscale insight into the interaction of DMSO with gold and also suggest a motif for anchoring organic adlayers of polar molecules on metal substrates.

4.2 The DMSO molecule

The dimethyl sulfoxide is an organosulfur compound with formula $(CH_3)_2SO$ (fig. 4.1). At room temperature it is a colourless liquid with a highly polar domain and two apolar methyl groups, making it soluble in a wide range of both aqueous and organic media. For this reason it is one of the most used solvent in chemistry. The main properties of DMSO are listed in table 4.1.

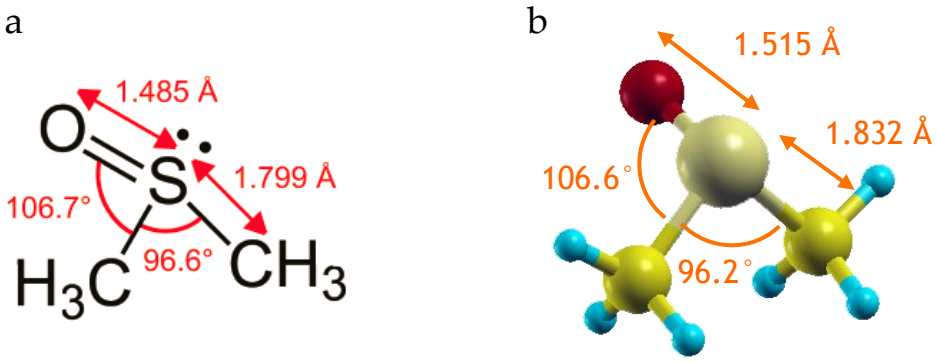

Figure 4.1: (a) A 2D model of DMSO with experimental values for bond lengths and angles and (b) a 3D model of DMSO, optimized with DFT calculations in gas phase with the theoretical values for bond lengths and angles .

Molecular formula	$(CH_3)_2SO$
Molar mass	78.13 g mol^{-1}
Density	1.1 g cm^{-3}
Melting point	18.5°C
Boiling point	189°C
Refractive index	1.48
Dielectric constant	48
Specific heat	0.45 cal/(g °C)
Dipole moment	4.3 D

Table 4.1: The main properties of DMSO at 25°C and 1 atm. [39]

DMSO was first prepared by the oxidation of dimethyl sulfide by the Russian scientist Alexander Saytzeff in 1867, but it had remained just a chemical curiosity until the 1940s when the plastic industry noted its unique solvent properties. Further research and development introduced DMSO as a solvent into other industrial processes such as insecticides, fungicides, and herbicides, and in other fields such as pharmacology, biology and microelectronics [40]-[46].

The most interesting uses of DMSO are however in surface science, as solvent.

4.2.1 **DMSO role in surface science**

Surface functionalization by deposition of organic molecules is an active area of research and it has several industrial applications due to the low cost and the wide range of potential applications [32]. In particular, self-assembled monolayers (SAMs) and polymer brushes have recently attracted considerable attention for the creation of such surfaces due to their intriguing physical-chemical surface properties and ease of processing [47]. In surface science, solvents are commonly used in order to obtain the formation of self-assembled monolayers by immersion of a suitable substrate in the solution containing the molecules of interest. Furthermore, in order to characterize the properties of large organic molecules at surfaces, it is often necessary to adopt deposition techniques based on solutions like drop-casting [48] or electrospray [49], in particular where conventional thermal evaporation is not practicable since heating would likely lead to molecular decomposition well before sublimation.

Usually the molecules of interest are deposited on a surface together with the solvent. The behavior of the solvent varies from case to case: it can desorb leaving on the surface only the molecules of interest or can adsorb on the surface and forming peculiar adsorption structures together with the molecules [49]. The delicate balance between the different kind of interactions can give rise to the co-adsorption or competitive deposition of solvent with adsorbate [50].

The drastic differences in the 2D ordering of self-assembled monolayers can be an excellent example of the key role played by the nature of the solvent [51]. But, before studies about complex systems are performed, it is crucial to comprehend how the solvents themselves interact with the surface of interest. There has been a longstanding interest in understanding the way in which water adsorbs on metals and surfaces in general[52][53], but relatively little effort has been focused on other solvents.

DMSO is an important solvent in electro-chemistry and its properties have been studied for a long time, because of its self-associative properties in neat solution, mixed with water and mixed with other solvents. An intense effort has been done to characterize also vibrational and other spectroscopic features of neat DMSO. Surprisingly, only few spectroscopic studies have been performed regarding DMSO on metal surfaces [54]-[56].

Furthermore, only two studies in literature have focused on the adsorption of DMSO on surfaces, by means of the scanning tunnelling microscope (STM), which is the ideal technique for this kind of investigations. In these two studies by A. Gewirth *et al.*[57][58], the authors observed by STM the adsorption of DMSO on Au(100) and Au(111) from gaseous and liquid phase at low and room temperatures. They reported some structures formed by DMSO on these surfaces and hypothesised some model for them. However the resolution of the STM images (fig. 1.2) of those studies is not sufficient to demonstrate the atomic-scale structural properties of DMSO adsorption and to define reliable structural models. Indeed, the above mentioned studies do not allow a complete comprehension of DMSO adsorption on metal surfaces.

A spectroscopic study can give information about the adsorption site and coordination of the adsorbates on surfaces but it cannot provide a satisfactory understanding of the geometry disposition and the long range order of the adsorbates. For this reason XPS and NEXAFS together with LT-STM has been

chosen as experimental techniques to characterize the adsorption of DMSO on Au (111) surface.

4.3 Experimental evidences

So far, only very few experimental works were able to characterized the adsorption of DMSO on metal surfaces, in ultrahigh vacuum (UHV) [54],[58]-[60] or in solution [58],[61],[62] environments. In particular, on Au(100) and Au(111), the structural properties of the DMSO-gold interface have been investigated by means of STM, but only attempt models were suggested, given the poorly resolved features in the STM images [57][58].

By means of X-ray photoelectron and near-edge absorption spectroscopy (XPS and NEXAFS), and by extensive Low Temperature Scanning Tunnelling Microscopy measurements (LT-STM) of DMSO on Au(111) from multilayer to sub-monolayer molecular coverages, the experimental results show how the adsorption of this molecule is characterized by the formation of characteristic molecular complexes composed of three or four DMSO molecules.

4.3.1 **XPS and NEXAFS results**

To characterize the adsorption of DMSO, our experimental group has first monitored the *O 1s* and *S 2p* photoemission spectral features of films obtained by depositing the molecules at different temperatures T_S of the Au(111) sample in the 153 K < T_S < 300 K range. Curve fitting reveals the presence of multilayer components for T_S < 193 K (top spectra in Figure 4.2), whereas a decreasing coverage starting from the full monolayer is observed in the 193 K < T_S < 300 K range. In Figure 4.2, the deconvolution profiles obtained by the fitting procedure highlight a binding energy shift between the monolayer (blue) and multilayer (black) components, arising from the screening effect of the metallic substrate.

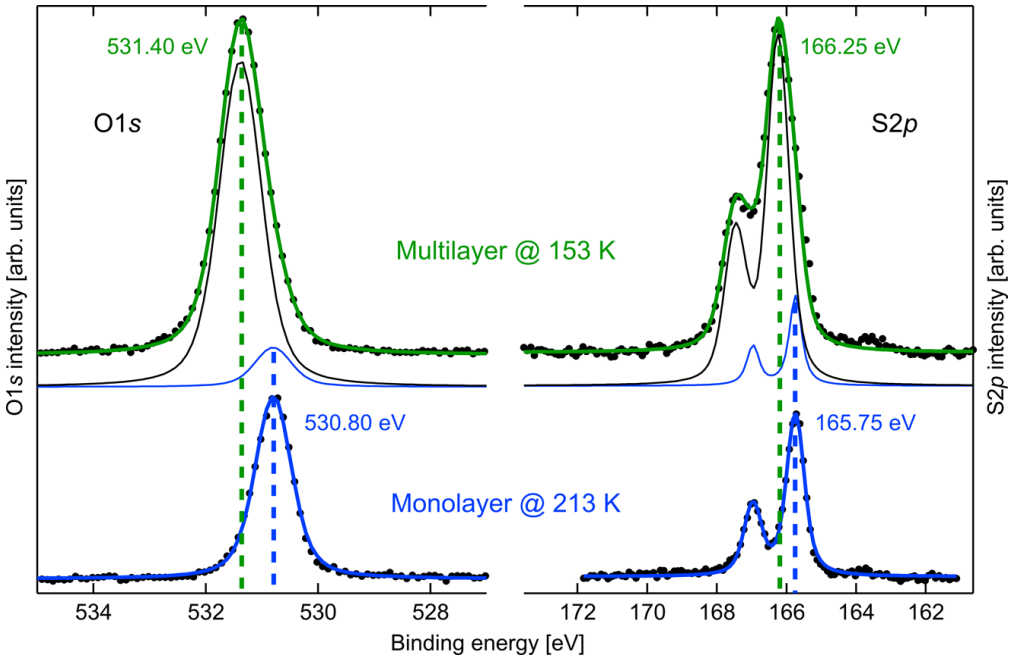

Figure 4.2: O 1s and S 2p spectra (hν = 650 eV) acquired on the multilayer (153 K, top spectra, green) and on the monolayer (213 K, bottom spectra, blue) phase. The uncertainty on the absolute binding energy values is ±0.05 eV. Individual components, obtained from the fit, are superimposed on the spectra.

Both the S and the O atoms of the DMSO molecule have an electron lone pair and can therefore act as electron-donors in binding to the substrate or to an adjacent molecule. In the latter case, as compared to a non-interacting molecule, an increase in the binding energy of the donating atom is expected. On these bases, in an early paper, Su and Faller [63] measured the difference between the O 1s and S 2p binding energies, ΔE_b, for several metal/DMSO complexes. They attempted to determine from this quantity whether the metal/molecule bonding occurred through the oxygen atom, the sulfur atom, or both. The same method was adopted to rationalise the XPS data for the adsorption of DMSO on Au(100) and Pt(111) [54],[62], where bi- and mono-dentate configurations have been found, respectively. By adopting this approach, the change in ΔE_b we found (≈ 0.1 eV, not significant within our errors) suggests that, as it occurs on the Au(100) surface, also in the Au(111) case DMSO adsorbs by interacting with both its donor terminations to the metal. However, an important aspect, which

was not discussed in the cited works, has also to be considered. Indeed, the supramolecular assembly at both monolayer and multilayer stages can be driven by the formation of intermolecular hydrogen bonds, which affects the binding energy of the termination involved in the interaction. Moreover, the O···CH_3 affinity could also drive the assembly of the monolayer phase. These observations indicated that it is not possible to unambiguously infer a bidentate DMSO/metal bonding from the observed small ΔE_b, and therefore called for further investigations to characterize the nature of the molecule/metal and molecule/molecule interactions.

To tackle this question, the DMSO adsorption geometry at the monolayer stage was also investigated by means of NEXAFS measurements. Figure 4.3 reports the O 1s light polarization-dependent NEXAFS spectra, measured on a DMSO monolayer grown at 213 K. The fit of the curves reveals the presence of distinct components, showing a clear dichroic effect, thus suggesting that the molecules adsorb on the surface with preferential orientation. These spectra resemble the ones taken in both the gas[65] and liquid phase [66]. In a nutshell, comparison with gas phase spectra [66],[67] identifies peak 3 (532.7 eV) as due to a transition from the O 1s to the LUMO, which has a π^* character; thus, it is expected to have maximum intensity when the photon polarization is perpendicular to the S=O bond. Conversely, peak 4 (533.5 eV) shows opposite polar dependence and can be assigned to the σ^* transition of the same bond. By comparing the intensities of this peak at the two polarization angles, it can be determined that the S=O bond is tilted by 25 ± 10° with respect to the surface plane.[68]

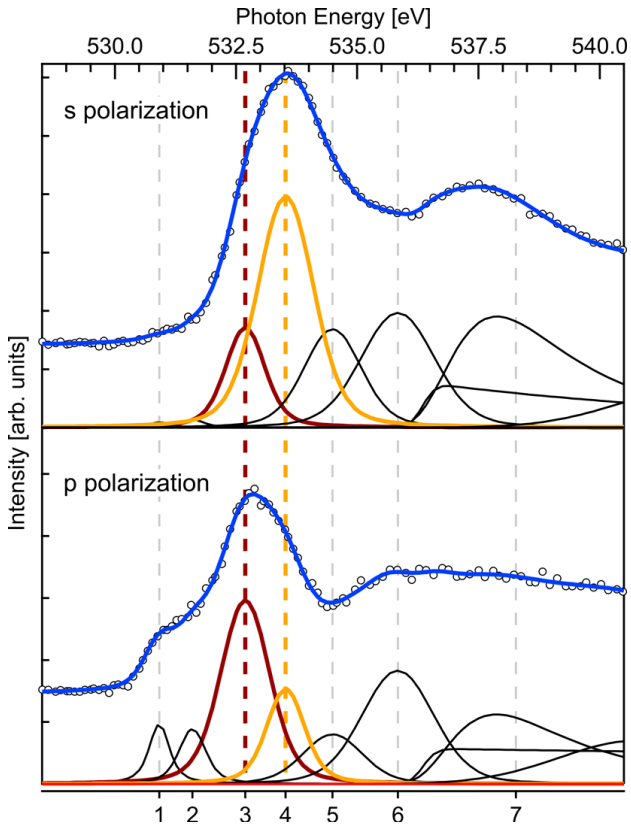

Figure 4.3: Linear dichroism NEXAFS spectra at the O 1s edge for two different synchrotron light polarizations (s polarization, parallel to the surface; p polarization, perpendicular to the surface) of DMSO/Au(111) after annealing at 213 K. The main peaks, 3 and 4, are located at 532.7 and 533.5 eV, respectively. Peaks 1 and 2 are assigned to impurities or beam induced damage, whereas peaks 5-7 are related to oxygen Rydberg states[58].

Summarizing the information obtained from XPS and NEXAFS, on one side, XPS indicates that DMSO could possibly interact with the metal both via the S and O atoms, whereas the role of hydrogen bonding remains to be assessed. On the other, at the same time, NEXAFS reveals that the S=O bond appears to be significantly raised from the surface plane. These two apparently conflicting findings called for a deeper investigation of the adsorption of DMSO, and in order to shed light on this point, high-resolution LT-STM imaging of molecular layers has been performed.

4.3.2 **LT-STM results**

Upon annealing of the multilayer phase at 193 K for 2 min, a high coverage, compact phase is obtained. This exhibits regions where complexes composed by four DMSO molecules (hereafter referred to as *square*) begin to form, where the compact phase starts to break apart, as it is shown in Figure 4.4. In the compact phase, the orientation of molecular rows is found to be approximately ±15° with respect to the directions of the herringbone reconstruction (the $\langle 11\bar{2} \rangle$ directions). By measuring the distance between the molecules, it is possible to define the unit cell of the molecular structure, which is described by the $\vec{b}_1$ and $\vec{b}_2$ vectors in the following matrix notation:

$$\begin{pmatrix} \vec{b}_1 \\ \vec{b}_2 \end{pmatrix} = \begin{pmatrix} 3 & 1 \\ -1 & 6 \end{pmatrix} \begin{pmatrix} \vec{l}_1 \\ \vec{l}_2 \end{pmatrix} \tag{4.1}$$

with the Au(111) unit cell vectors being defined as $\vec{l}_1 = a_0(1;0)$ and $\vec{l}_2 = a_0(\frac{1}{2};\frac{\sqrt{3}}{2})$ the nearest neighbour distance in the Au lattice (0.288 nm).

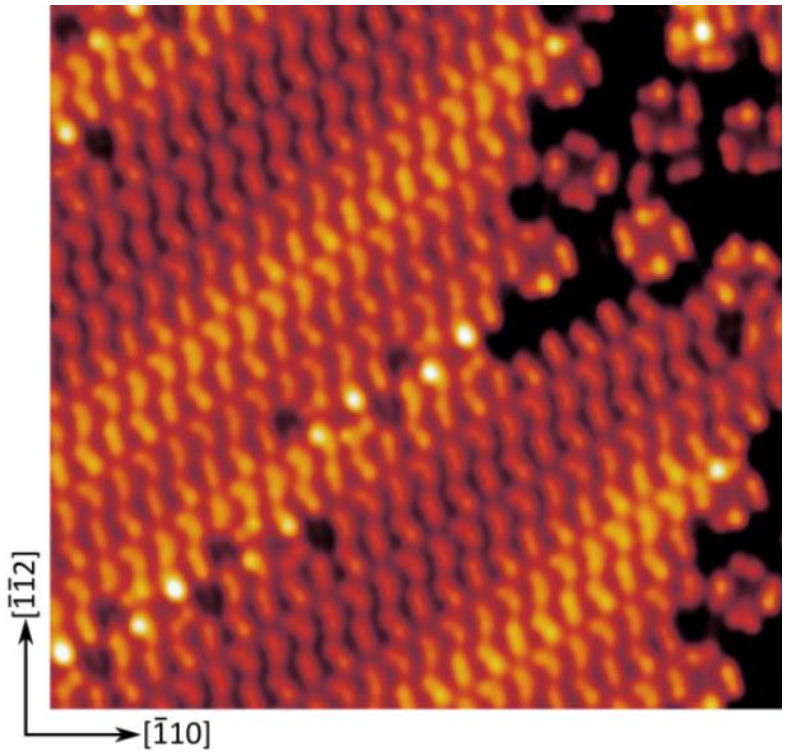

Figure 4.4: Experimental STM image (12.75 × 12.75 nm²) showing the high coverage phase (left part of the image), coexisting with patches of square complexes (on the right). Image parameters: *Vs*= 100 mV, *It*= 100 pA.

Then the focus has been moved to the sub-monolayer phase. Interestingly, after annealing the monolayer phase to 233 K, thereby desorbing a large part of the DMSO molecules, the surface appears as shown in the STM image in Figure 4.5. From the high resolution insets (Figure 3b,c), the features corresponding to the molecular structure of DMSO can be straightforwardly identified: the two brighter protrusions correspond to the methyl groups, whereas the less intense one can be assigned to the oxygen atom. The appearance also suggests that the molecule is sitting in an "inverted umbrella" geometry, i.e., with the S atom directly interacting with the Au surface. From these considerations, the dominant structural motif of this layer appears to be the *square* complex, together with a smaller number of isolated, single DMSO molecules.

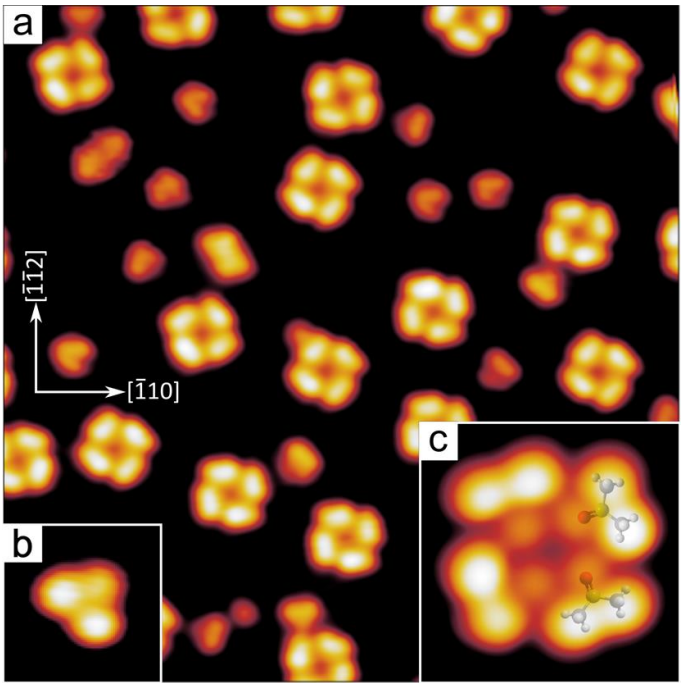

Figure 4.5: (a) STM image (12.82x12.82 nm^2) showing the square complexes formed by annealing the DMSO/Au(111) multilayer phase to 233 K. Panels (b) (1.00x1.00 nm^2) and (c) (1.60x1.60 nm^2) are high-resolution details of a single isolated DMSO molecule and a square complex, respectively. Transparent ball and stick models are superimposed to guide the eye in the identification of the single molecules. Image parameters: (a) Vs = 100 mV, It = 100 pA; (b) Vs = 50 mV, It = 100 pA; (c) Vs = 100 mV, It = 50 pA.

Within the *square* complex, it appears that DMSO favours a geometry where the oxygen atoms are located close to each other, a configuration that should intuitively be relatively unstable, due to mutual repulsion of the oxygen atoms. Subsequent annealing of the surface up to 273 K leads to a further decrease in the molecular coverage and to the formation of a variety of complexes, which are summarized in Figure 4.6

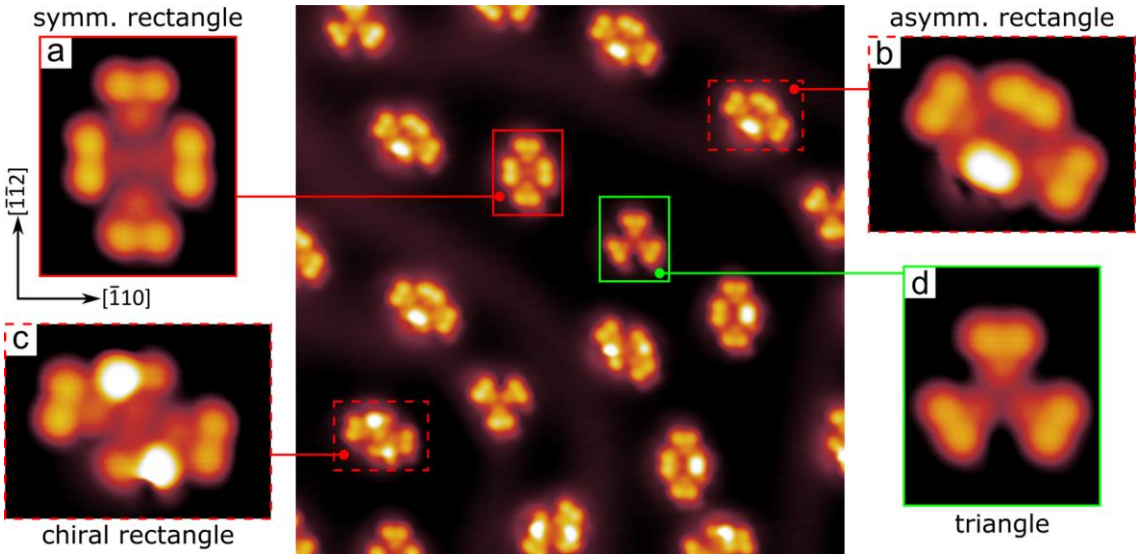

Figure 4.6: STM image (centre, 12.94 x 12.94 nm²) showing the various complexes that form on the surface after annealing to 273 K. (a-d) Insets show high resolution details of complexes: (a) the *symmetric rectangle* complex (1.63x1.99 nm²), (b) the *asymmetric rectangle* complex (2.21 x 1.62 nm²), (c) the *chiral rectangle* complex (2.21 x1.62 nm²) and (d) the *triangle* complex (1.63 x 1.99 nm²). All images: 30 mV < Vs < 50 mV, 100 pA < It < 200 pA.

In the same figure, high resolution details of the four most common complexes are shown. While the arrangement of the DMSO molecules within the complexes in Figure 4a,d can be readily identified, since the shape of the single DMSO molecules is evident, the complexes in Figure 4b,c are less trivial to understand. More precisely, in the STM image in Figure 4b, three DMSO molecules can be readily identified, whereas the nature of the brighter protrusion is not straightforward. Similarly, in Figure 4c, two DMSO molecules can be recognized, whereas the assignment of the two brighter features needs

further investigation. From now on the complexes will be referred in Figure 4a-d as the *symmetric rectangle*, *asymmetric rectangle*, *chiral rectangle*, and *triangle*, respectively. Surprisingly a common feature of all the described complexes is evident, i.e. the oxygen atoms appear to be preferentially located close to each other, a configuration that should be extremely unfavourable due to the negative charge on the oxygens.

To understand this behaviour, Density Functional Theory (DFT) calculations of the structural, electronic, and energetic properties of the observed DMSO complexes as well as simulations of the STM images have been carried out.

4.4 Computational modelling

4.4.1 **Technical aspects**

DFT calculations were performed with the plane-wave pseudopotential package QUANTUM ESPRESSO [24] using ultrasoft pseudopotentials[69] and a GGA-PBE[11] exchange-correlation functional. The wave function (charge) energy cut-off has been fixed at 408 eV. Brillouin-zone sampling refers to a Monkhorst-Pack sampling and included two k-points in x and y directions, and only one in z direction, perpendicular to the surface. An higher number of k-points would have caused an exponentially increase in the calculation time, without real benefits for the precision.

After a first test phase, since van der Waals interactions play a non-negligible role in self-assembled organic structures, the calculations have been performed including the semi-empirical dispersion-corrected DFT (DFT-D) method proposed by Grimme[18], recently implemented in the QE package[70] and successfully used by Casarin et al. [71] to determine the adsorption energetics of iron phthalocyanine on Ag(110). Also the self-consistent vdW-DF method, proposed by Dion et al.[14], the LDA-PZ[8] and BLYP[10][11] pseudopotentials have been tested in the early phase of the study, without success.

The Au(111) surface was modelled with three layers for the simulations of the DMSO complexes and four layers for the monolayer simulation, allowing a vacuum (adlayer-surface) distance of ≈1.4 nm. The bottom layer of the surface was kept fixed at the bulk Au calculated values to mimic the behaviour of the metal substrate. In the presence of the surface, only forces acting on the top Au layer and the molecular adlayer atoms were relaxed up to 0.26 eV/Å. STM images were simulated within the Tersoff-Hamann approximation according to which the tunnelling current is proportional to the energy-Integrated electronic Local Density Of States (ILDOS) [28]. To mimic the constant-current experimental STM images, an ILDOS iso-surface lying within a certain height range over the surface has been taken. All the images in this paragraph were simulated at a bias of 100 mV, at an ILDOS value for the iso-surface of 4×10^{-3} nm^{-3}, lying at an average distance of approximately 0.5 nm from the first atomic layer. Ball models are rendered with the XCrySDen software packages [25].

4.4.2 **Single DMSO molecule adsorption**

The study started obviously from a complete analysis of the adsorption of DMSO molecule on Au (111) surface. Starting from a gas-phase optimized molecule (see Figure 4.1b), several adsorption geometries, as well as several adsorption sites have been used as starting point for the simulations. As result, only two stable configurations have been found: the "umbrella", with the sulfur atom pointing out of surface (Figure 4.7) and the "inverted umbrella", i.e., with the S atom directly interacting with a *on top* site of the Au surface (Figure 4.8). To determine the most stable configuration, the adsorption energy of the molecule has to be estimated:

$$E_{ads} = -\left[E(DMSO/sub) - E(DMSO) - E(sub)\right] \tag{4.2}$$

where *sub* indicates the substrate, i.e., the clean Au(111) surface; *E(DMSO/sub)*, *E(DMSO)* and *E(sub)* indicate the energies of the total system (adsorbed

molecule and substrate), of a gas-phase, isolated DMSO molecule, and of the substrate, respectively. Comparing the adsorption energies, the "inverted umbrella" results to be, accordingly with the literature [57][58], the most stable (see Table 4.2). Finally it has been simulated the STM image of the "inverted umbrella" configuration (see Figure 4.9) to confirm the model.

Since the experimental and simulated STM images were in good agreement, the "inverted umbrella" has been used as starting point for the further calculations.

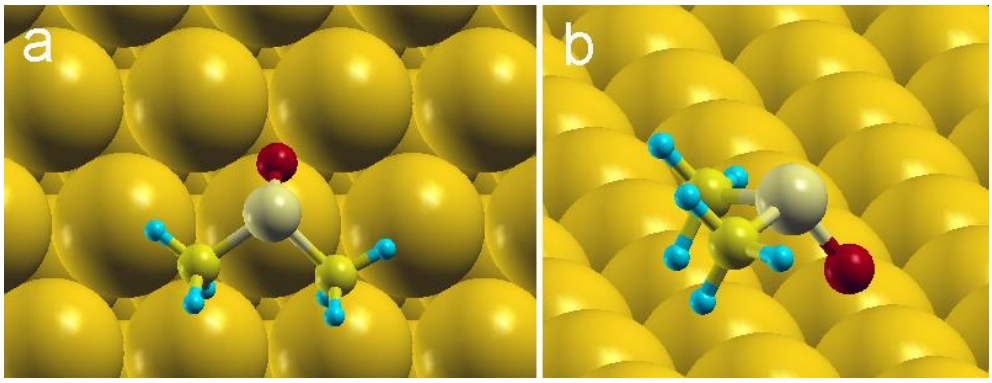

Figure 4.7: (a) lateral and (b) top view of stick and ball model for the "umbrella" adsorption geometry of the DMSO molecule on Au(111) substrate obtained by DFT calculation.

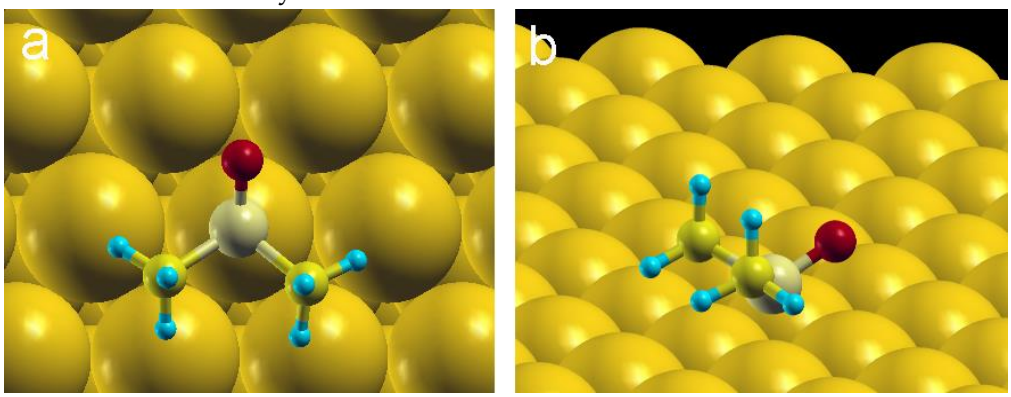

Figure 4.8: (a) lateral and (b) top view stick and ball model for the "inverted umbrella" adsorption geometry of the DMSO molecule on Au(111) substrate obtained by DFT calculation.

Adsorption configuration	E_{ads} [eV]
"umbrella"	1,70
" inverted umbrella"	1,78

Table 4.2: Calculated Adsorption Energies (E_{ads}) of a single DMSO Molecule adsorbed *on-top* on Au(111) substrate in various configurations.

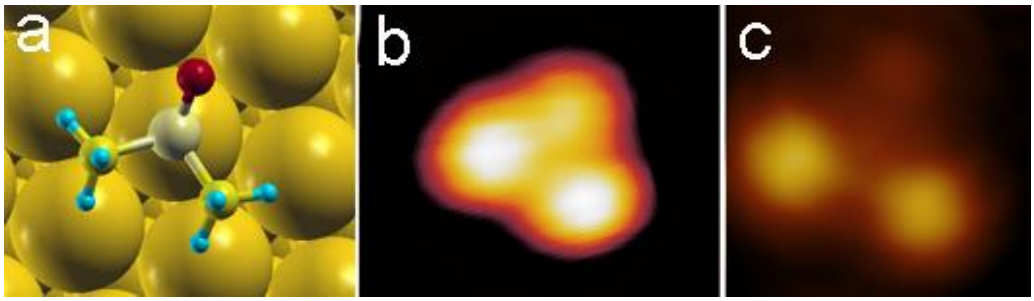

Figure 4.9: (a) stick and ball model for the "inverted umbrella" adsorption geometry and its relative (b) experimental (1.00x1.00 nm^2) and (c) simulated STM images.

4.4.3 The *impossible* "triangle" complex

For sake of simplicity and computational cost, the study started from the simplest complex, i.e., the *triangle*. From the experimental STM images, it can be easily inferred that the complex is formed by three DMSO molecules with an experimentally measured distance of approximately 5.8 Å (twice respect the Au lattice constant) between the S atoms. As already reported in the previous section, DFT calculations indicate that the most favourable adsorption configuration for a single adsorbed DMSO is the on-top site, with the S atom bound to the metal surface. Both these information have been used to elaborate the model shown in figure 4.10a.

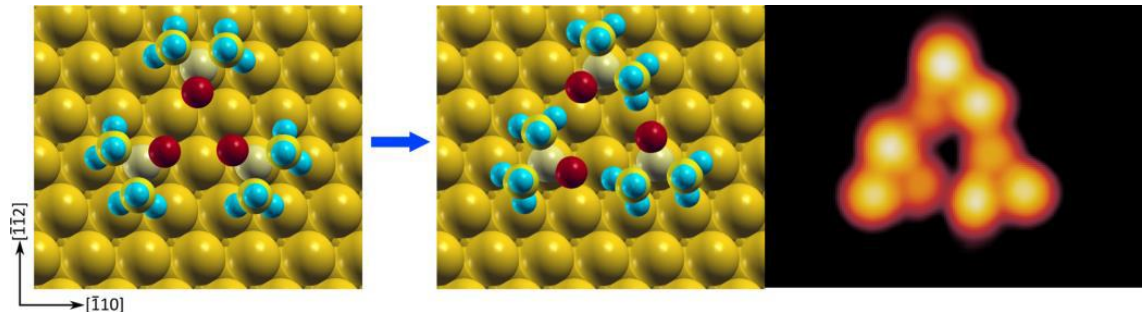

Figure 4.10 : stick and ball model for the *triangle* complex (a) before and (b) after the DFT optimisation; (c) simulated STM image of the optimised *triangle* complex.

As expected from the chemical considerations of the paragraph 4.3.2, the *triangle* with all three DSMO adsorbed on top is predicted by DFT to be less

stable (losing 0.13 eV/molecule) with respect to a single adsorbed DMSO taken as the reference configuration (1.78 eV/molecule, see Table 4.3). The adsorption energy per molecule have been calculated as

$$E_{ads}(n) = -\frac{1}{n}\left[E(nDMSO/sub) - n \times E(DMSO) - E(sub)\right] \qquad (4.3)$$

where *sub* indicates the substrate, i.e., the clean Au(111) surface, for the single DMSO, or the surface with one adatom, for the triangle; *nDMSO* indicates a DMSO complex with n molecules; *E(nDMSO/sub)*, *E(DMSO)* and *E(sub)* indicate the energies of the total system (adsorbed complex and substrate), of a gas-phase, isolated DMSO molecule, and of the substrate, respectively.

In this *triangle*, upon relaxation, each DMSO, due the O-O repulsion, rotates around the axis normal to the surface and containing the S atom by slightly more than 30°, in order to maximize the CH3···O interaction, by analogy with the behaviour reported for the pure crystalline form [64]. However, the simulated STM image obtained from the relaxed configuration (Figure 4.10c) is clearly not compatible with any of the structures observed in the experimental STM images. It is thus confirmed that the triangle structure would be completely unstable without a coordination element in the middle.

Adsorption configuration	E_{ads} [eV]
single DMSO	1.78
triangle without adatom	1.65
triangle with adatom	2.03
asymmetric triangle	1.79

Table 4.3: Calculated Average Adsorption (E_{ads}) per DMSO Molecule of the Various Molecular Complexes.

4.4.4 **The gold adatom role in "triangle"**

To explain the stability of the structure, the presence of an Au adatom, sitting on a "hollow" site and trapped within the complex has been therefore hypothesized (Figure 4.11a). This adatom could indeed act as an acceptor for the electrons of the oxygen atoms. As a consequence of this assumption, the triangle, once optimised, becomes stable, gaining 0.25 eV/molecule with respect to single DMSO adsorption energy (see Table 4.3). In agreement with the experimental STM data, the simulated images clearly show no protrusion related to the adatom at the centre of the complex, as it can be seen in Figure 4.11c.

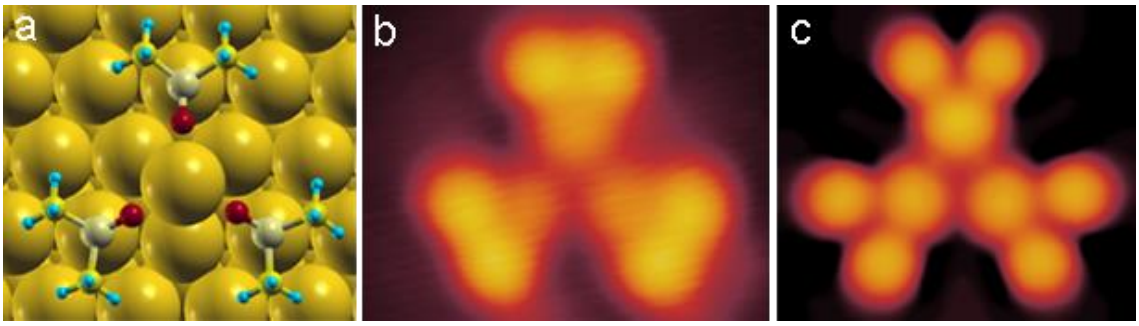

Figure 4.11: (a) stick and ball model for DFT-optimised *triangle* including a gold adatom in the middle and its relative (b) experimental and (c) simulated STM images.

It should be noted that in the experimental STM images the triangles can be found pointing towards both the$[11\bar{2}]$ and the$[\bar{1}\,\bar{1}2]$ directions (see Figure 4.12). These two possible adsorption configurations of the triangle are consistent with the preferred adsorption site of DMSO (on-top), and with the two possible "hollow" Au sites for the adatom (hcp and fcc). The difference in energy between the two structures is negligible because it's of the same order of the DFT accuracy (meV). The manipulation of the complex with the STM, if a voltage pulse is applied to the centre of a *triangle*, can induce a rotation as shown in figure 4.13: the adatom moves to the nearest possible site (from *fcc* hollow to *hcp* hollow or

vice versa), while the DMSO molecules consequently move to the nearest on-top adsorption sites, resulting in a *triangle* pointing in opposite $[\bar{1}\,\bar{1}\,2]$ directions (see Figure 4.13a and 4.13b). Measuring on the STM images the minimum displacement of a *triangle* upon a tip-induced rotation a value of ~1.8 Å, which is in good agreement with the displacement expected from the model in Figure 4.13c (~1.7 Å).

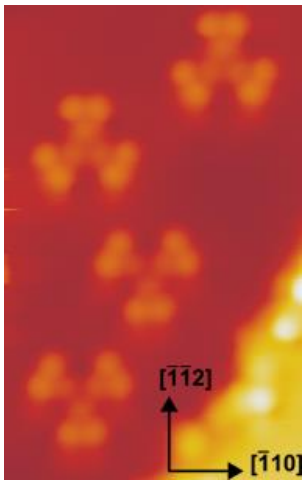

Figure 4.12: experimental STM image of some *triangles* pointing in both the $[11\bar{2}]$ and the $[\bar{1}\,\bar{1}\,2]$ directions.

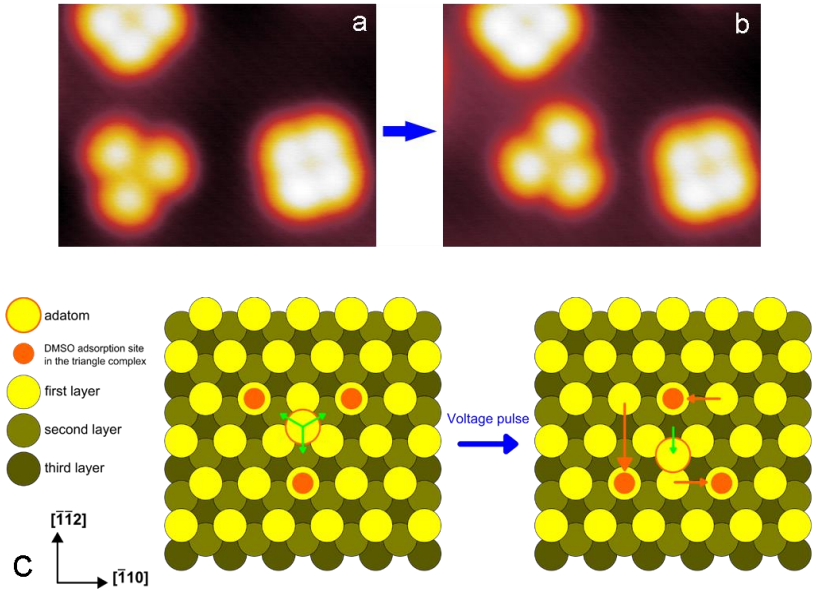

Figure 4.13: STM image showing the *triangle* (a) before and (b) after a voltage pulse. (c)Model explaining the direction change process of the *triangles*. In figure on the left the green arrows indicate the possible positions to which the adatom (in *fcc* hollow site in this example) can move (in *hcp* hollow sites in this example). If the adatom moves, the molecules follow it by changing their adsorption site to the near on-top sites as shown in figure on right.

The voltage pulse, if applied then on top of a molecule at sufficiently high voltages, ~~it~~ can "switch on" a bright protrusion (Figure 4.14a), which is related to a vertically "flipped" DMSO adsorption configuration (*i.e.* the "umbrella" with the sulfur atom pointing out of surface). This structure (hereafter referred to as *asymmetric triangle*) has been also found spontaneously formed at higher temperatures. In the figure 4.14c and 4.14d is possible to see the optimized DFT model for this structure, while in Figure 4.14b is represented the simulated STM image. As expected, the asymmetric triangle lose 0.24 eV/molecule with respect to normal *triangle*.

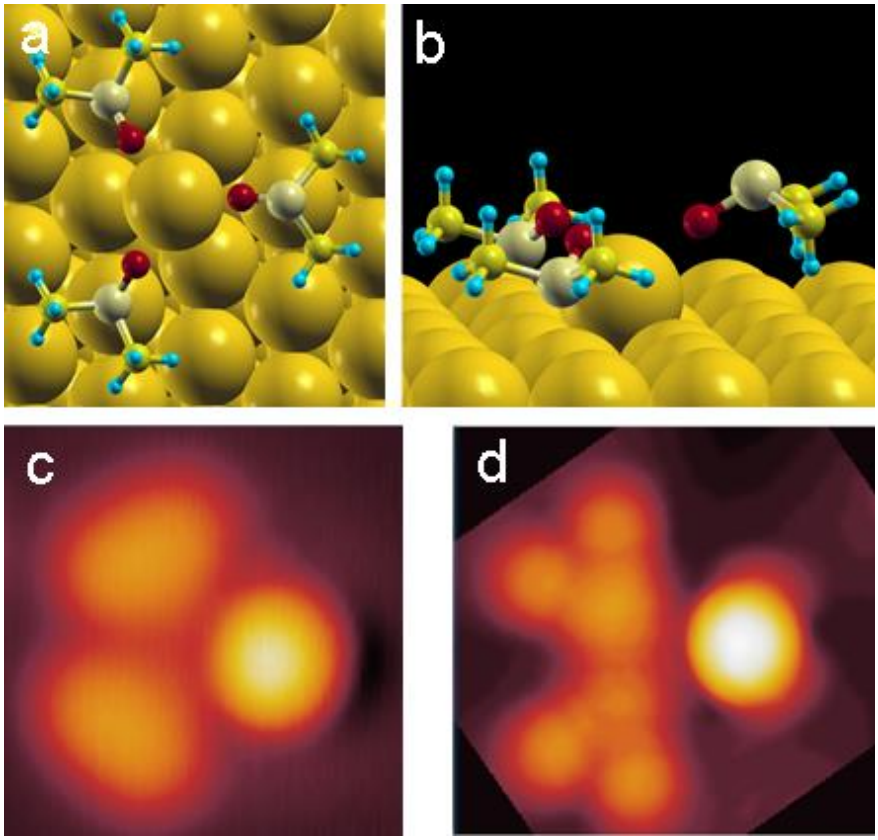

Figure 4.14: (a) top and (b) lateral view of stick and ball model for a DFT-optimised *asymmetric triangle*; its relative (c) experimental and (d) simulated STM images.

For a deeper comprehension about the nature of the interaction between gold adatom and DMSO complex, some post processing analysis has been performed. In particular DFT calculations reveal that a peculiar redistribution

of the electron density occurs around the Au adatom, as shown for the *triangle* by the charge density transfer plots in Figure 4.15. The latter has been calculated as

$$\rho_{tot}(r) = \rho_{sub}(r) - \sum \rho_{mol}(r) \tag{4.4}$$

where $\rho_{tot}(r)$ is the charge density of the total system, $\rho_{sub}(r)$ the density of the gold substrate including an isolated adatom, and $\Sigma\rho_{mol}(r)$ the density of three non-interacting DMSO molecules in gas phase.

Namely, the density depletion (blue lobe) occurring at the gold adatom suggests that this atom displays a significant degree of cationic behaviour. This is confirmed by the calculation of the atomic Löwdin charges [72]: even in the absence of DMSO co-adsorption, a single Au adatom in the hollow position is always slightly positively charged (≈ -0.21e^-) with respect to an atom of the surface layer, as it donates electronic charge to the nearest neighbour surface Au atoms. In the presence of a DMSO complex, the adatom recovers only part of its electronic charge (≈ +0.08e^- relative to the single adatom) and rearranges the occupation of its *s*, *p*, and *d* orbitals. Moreover, at the same time, an increase in the electronic charge occurs on its second nearest neighbour surface Au atoms, which are directly interacting with the sulfur of DMSO. The oxygen atoms surrounding the adatom are polarized in a characteristic double peak-trough pattern: this charge rearrangement pattern favours the coordination of the oxygen terminations of DMSO with the gold adatom, which effectively acts as ionic linker between the otherwise mutually repelling molecular terminations. The observed charge depletion and the proximity of deep *p*-orbitals associated with the oxygen atom ligands imply the lack of electron states available for tunnelling in the STM observations at the Au site.

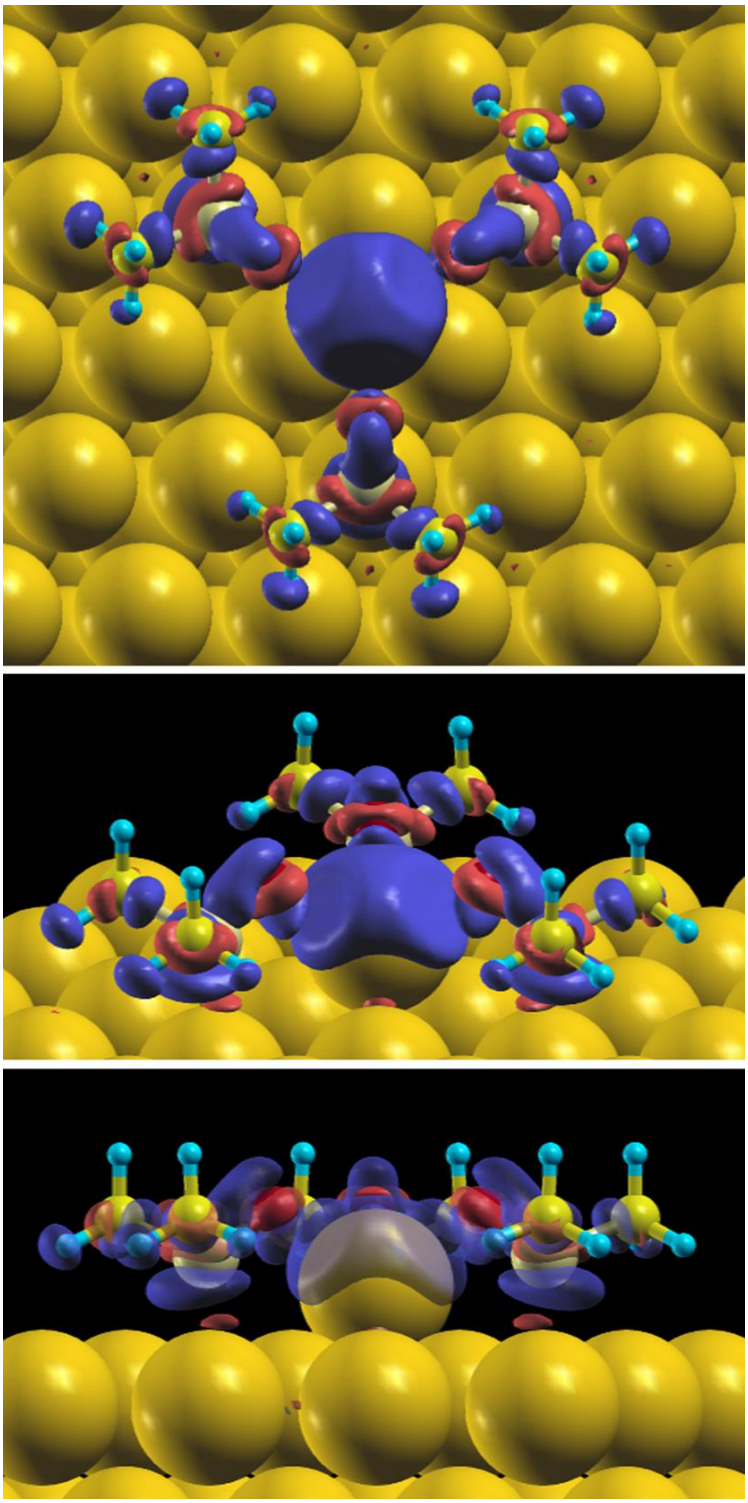

Figure 4.15: Top (top panel) and side (bottom panel) views of the changes in charge density around a gold adatom coordinated by three DMSO molecules (*triangle* complex) on the Au(111) surface with a pre-existing adatom on it. A perspective view (middle panel) is also shown. The accumulation of negative charge is depicted in red, the depletion in blue. The blue lobe surrounding the adatom highlights its cationic behaviour.

This is consistent with the STM images where the adatom is indeed not visible. It is to be noted that linker adatoms which cannot be resolved in STM images were also reported in other works, and this effect was accompanied by a reduction of the occupation of the adatom states upon surface complexation [73][74]. The finding of a significant charge redistribution around the entrapped adatoms is analogous to what it was observed by Pawin et al. for 9,10-anthracenedicarbonitrile on Cu(111), where a similar effect occurs [75].

Finally, we observe that the ionic character of the DMSO-adatom interaction is consistent with the average Au(adatom)-O distance, which is approximately 2.6 Å, and 30% larger than the same distance in related oxo-gold compounds (~2.0 Å), where the Au-O bond is mainly covalent [76].

4.4.5 **The "rectangle" complexes**

On the basis of the same chemical considerations used for the triangle, the stability of the *symmetric rectangle* can only be explained by introducing two Au adatoms, as shown in Figure 4.16a, gaining 0.40 eV/molecule with respect to a single adsorbed DMSO. Also in this case, the adatoms are not visible in the experimental STM images(Figure 4.16b), and the absence of protrusions related to their presence is confirmed by the calculated image. The two adatoms are located in fcc and hcp hollow sites, and consistently with the C_3 symmetry of the substrate, they are observed with the long side oriented in all the three equivalent $\langle \bar{1}\,\bar{1}\,2 \rangle$directions.

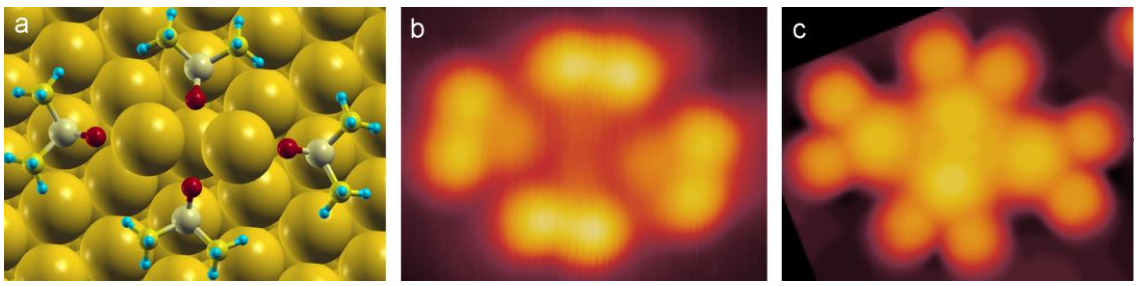

Figure 4.16: (a) stick and ball model for DFT-optimised *symmetric rectangle* including two gold adatoms in the middle and its relative (b) experimental and (c) simulated STM images.

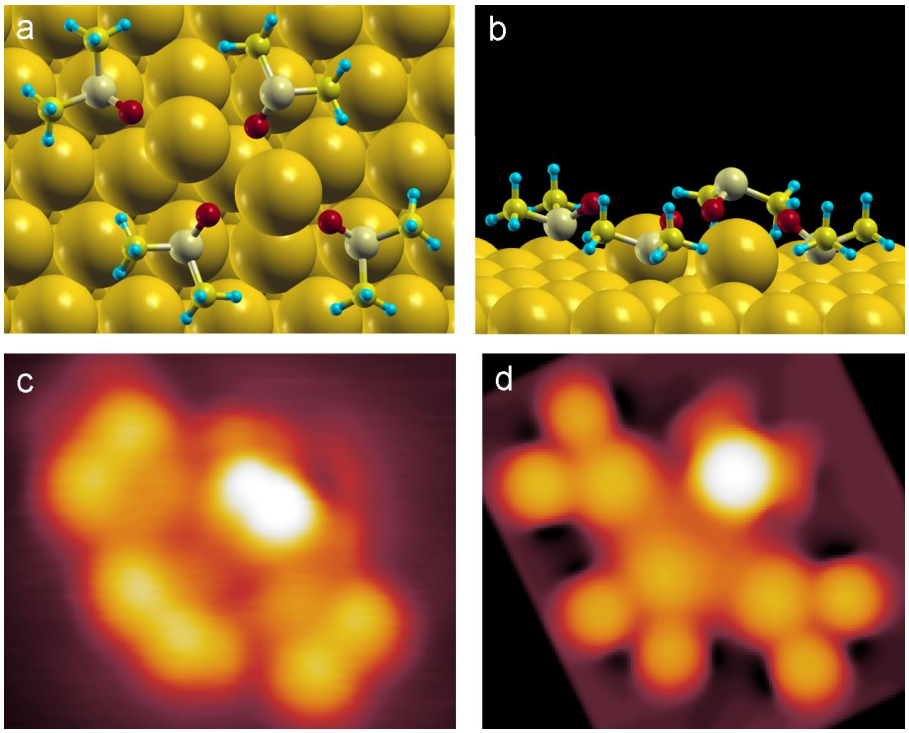

Figure 4.17: (a) top and (b) lateral view of stick and ball model for a DFT-optimised *asymmetric rectangle*; its relative (c) experimental and (d) simulated STM images.

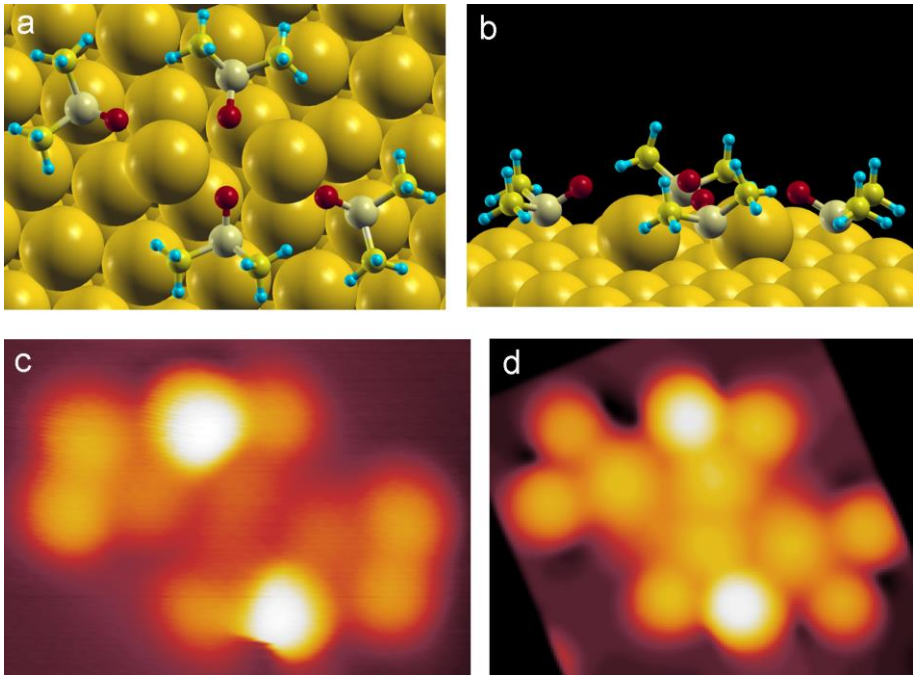

Figure 4.18: (a) top and (b) lateral view of stick and ball model for a DFT-optimised *chiral rectangle*; its relative (c) experimental and (d) simulated STM images.

With concern to the *asymmetric rectangle* and the *chiral rectangle*, various models have been tested, and the ones that show the best agreement with the experiment in terms of energetics and appearance of the STM images are shown in Figure 4.17 e 4.18. The energetic gain, referred to a single adsorbed DMSO, is 0.35 and 0.32 eV/molecule, respectively (see Table 4.4) .

In the *asymmetric rectangle* (Figure 4.17), the brighter protrusion is originated by a DMSO molecule in an "umbrella" adsorption geometry, i.e., with the S atom pointing out of the surface plane and the O atom interacting with the Au adatoms. As in the case of the *symmetric rectangle*, the two adatoms are located in fcc and hcp hollow sites(Figure 4.17a and 4.17b), and the complexes can be found on the surface with the same orientations. The *chiral rectangle* (Figure 4.18) is again characterized by the presence of two adatoms in fcc and hcp hollow sites. However, in this case, the two sites are almost aligned along the $[\bar{1}10]$direction, with the adatoms located slightly off-site, giving rise to a characteristic angle of ±14° of the long side of the complex with respect to the equivalent $\langle\bar{1}10\rangle$direction (Figure 4.18a and 4.18b).

The simulated STM images in Figure 4.16c, 4.17d and 4.18d are in good agreement with the corresponding experimental images, since the morphology of the main features can be immediately identified, in particular concerning the lack of features related to the presence of the adatoms. However, it is also clear that the methyl groups in the simulated images always appear lower than the experimental ones. The main reason could be the slight overestimation of the strength of the sulfur-gold bond, whose calculated distance is 2.62 Å, by the chosen pseudopotential. In the case of complexes in which at least one Au adatom is present (e.g. the *triangle*), the result is a tilting of the molecule that lowers the methyl groups with respect to the surface (figure 4.19d). To validate this mechanism, and exclude other possible explanations, we optimized a model for the *triangle* with another pseudopotential (BLYP)[12],[13], that does not alter the gold–oxygen bond, but underestimates the strength of the gold–

sulfur interaction, yielding Au-S distance of 3.7 Å. The calculations reveal in this case a higher position of the methyl groups (figure 4.19e) and the corresponding STM image better reproduces the observed contrast (figure 4.19c). However, such an underestimation of the gold–sulfur bond, makes this pseudopotential not suitable to reproduce the other complexes (e.g. the *rectangles*). Indeed, without a correct description of the interaction with the substrate, the peculiar bi-dentate interaction between DMSO and Au would be completely lost.

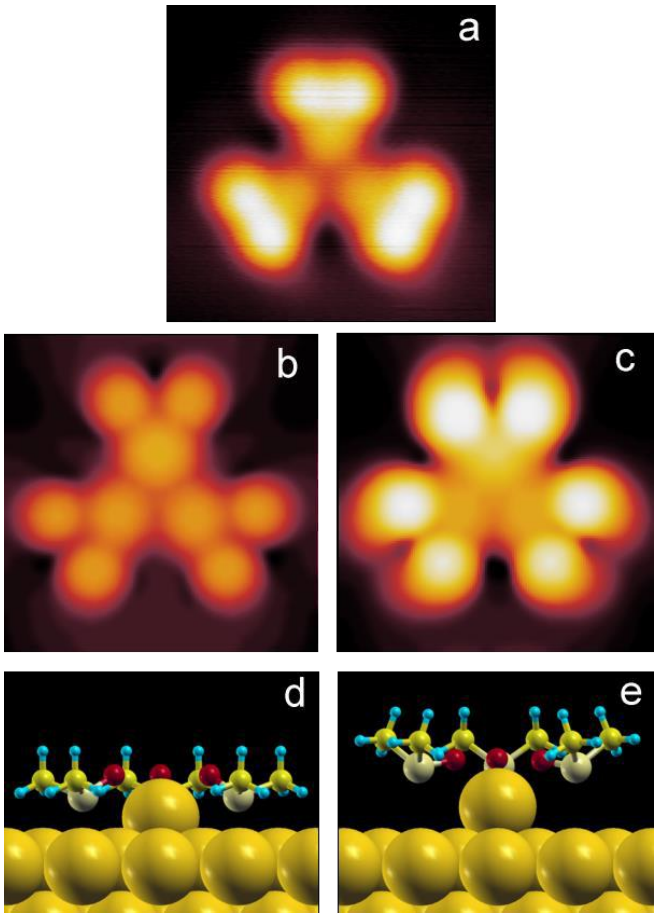

Figure 4.19: (a) experimental STM image of the triangle; (b) calculated STM image based on a DFT-optimized structure with ultrasoft pseudopotentials, with the corresponding ball and stick model shown in (d); (c) calculated STM image of the same structure optimized with the BLYP pseudopotential, with the corresponding ball and stick model in (e).

4.4.6 **The "square" complex**

The case of the *square* complex deserves a separate discussion. Similarly to the other complexes, the oxygen atoms are quite close to each other, possibly giving rise to a repulsive interaction that could in principle destabilize the complex. However, in this case the molecular arrangement also favours the interaction between the oxygen and the methyl groups of each couple of adjacent molecules. In the model shown in the Figure 4.21a, the calculated CH-O angle in the closest H-O couple (2.5 Å) is approximately 140°, and this geometry does in fact favour the formation of a hydrogen bond [77]-[79]. Additionally, the *square* exhibits a remarkable stability upon manipulation with the STM tip. Therefore, the question arises whether an adatom is trapped inside the complex or not, and the contrast of the STM images cannot address this point since it has been verified that the trapped adatoms, even when present, are not visible both in the experimental and simulated STM images. To clarify this point, on one side the distribution of the characteristic orientations of the complexes has been analysed with respect to the Au(111) crystallographic directions in the experimental STM images, and on the other, we carefully evaluated the energetics of the different complexes as obtained by DFT.

As a starting point, the orientation of more than 1500 square complexes has been measured on the experimental STM images, using as a reference the directions shown as blue lines on the top inset of Figure 4.21. By taking into account both the symmetry of the substrate and the symmetry of the square complexes themselves, the resulting angular distribution of the complexes falls within 0° and 60°, and is represented by the blue histogram in Figure 4.20 (left axis). It is clear that squares are aligned around four distinct angles, namely, 7°, 23°, 36°, and 53° with an error of about ±4°.

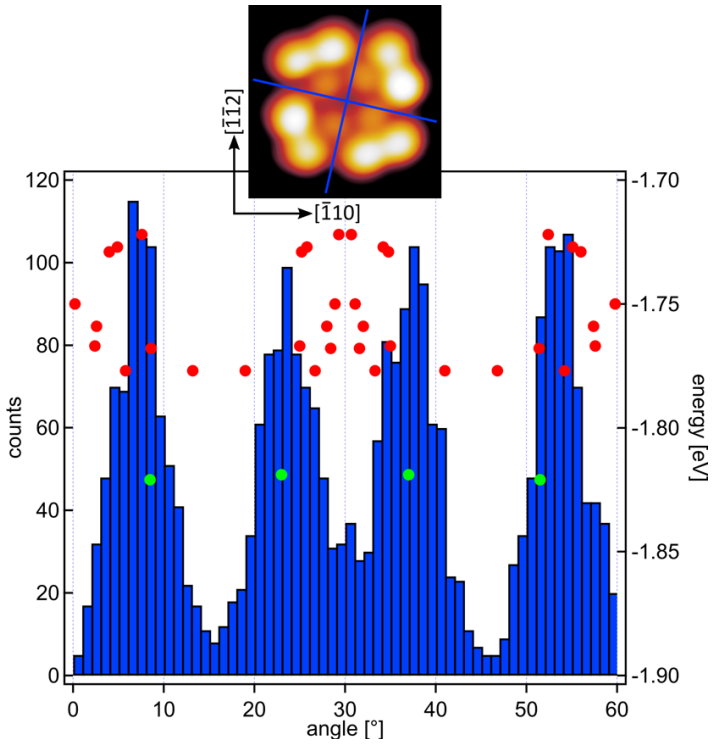

Figure 4.20: Experimental angular distribution of the square complexes (blue histogram, left axis) and the adsorption energy per molecule (markers, right axis) of the possible candidate models for the square complex with (red) and without (green) the central adatom. The thumbnail above the graph shows the directions taken as a reference to determine the orientation of the square complexes.

In the same graph, the green and red markers show the calculated energies of various structures composed by four DMSO molecules (right axis), hypothesised as reasonable candidates for the *square* complex, as a function of their characteristic angle with respect to the surface. In particular, the red markers correspond to the models including the Au adatom, the green ones the model without the gold adatom. It is to be noted that relaxation of the models corresponding to the red markers after removal of the adatom consistently yielded one of the structures corresponding to the green marker.

Both analyses indicate that, at variance with the other observed complexes, the *squares* do not include a central gold adatom: first, from the energetic point of view, it is clear that the complexes with no adatom are always more stable

(green markers) by more than 50 meV. Second, a clearly different angular distribution should be found if the squares included the adatoms(red markers).

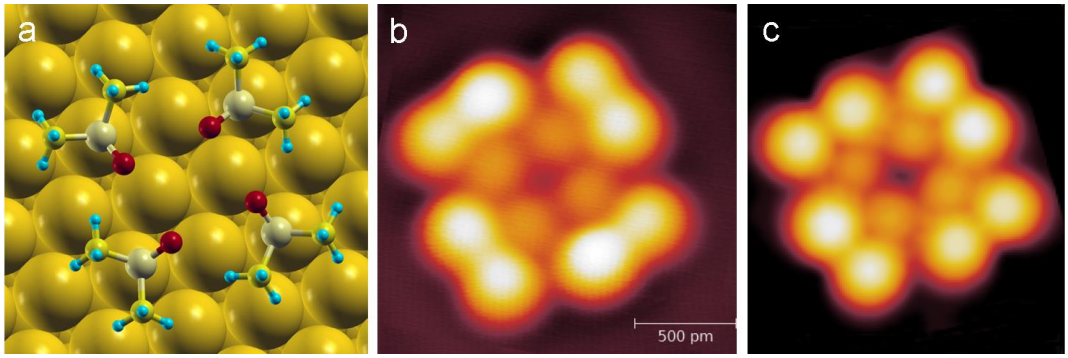

Figure 4.21: (a) stick and ball model for DFT-optimised square without the gold adatom in the middle and its relative (b) experimental (1.60x1.60 nm2) and (c) simulated STM images.

The energetics of the various complexes can help to rationalize the experimental observations. The least stable species is the single DMSO molecule (1.78 eV/molecule), that was in fact observed in rare cases. The square complex (1.83 eV/molecule) is more stable than the single adsorbed molecule, and is by far the dominant structure, together with the monolayer phase, at temperatures below 233 K (see Figure 4.5a). This is apparently in contrast with the fact that all the other complexes are significantly more stable than the square itself, and should therefore dominate the surface. However, as shown above, strong energetic and structural evidence indicate that this particular complex is the only one which is not entrapping one or more Au adatoms. It is reasonable to assume that at temperatures below 233 K a decreased availability of gold adatoms prevents the formation of triangles and rectangles, and therefore favours the formation of the squares. This consideration further strengthens the conclusion that no adatoms are trapped inside the squares.

The cohesion energy per molecule, reported in Table 4.4 for all the complexes, is defined as

$$E_{coh}(n) = E_{ads}(n) - E_{ads}(1) \qquad (4.5)$$

and indicate energy gain per DMSO molecule in the most stable adsorption configurations of a complex with respect to the adsorption of the individual molecule(s) on the bare Au(111) surface. Analysis of the cohesion energies shows evidence that the presence of the adatoms in *triangles* and *rectangles* plays a relevant role in the stability of the complexes: molecule-molecule and molecule-adatom interactions (E_{coh}) account for 15-18% of their adsorption energies E_{ads}. This stabilization effect of the adatoms is also reflected by the fact that desorption of DMSO becomes more costly at increasing temperatures. Conversely, in the *squares*, E_{coh}/E_{ads} is only 3%, consistently with the weaker molecule-molecule hydrogen bonding.

Adsorption configuration	E_{ads} [eV]	E_{coh} [eV]
single DMSO	1.78	-
square	1.83	0.05
triangle	2.03	0.25
symm. rectangle	2.17	0.40
asymm. rectangle	2.11	0.35
chiral rectangle	2.09	0.32

Table 4.4: Calculated Average Adsorption (E_{ads}) and Cohesion Energies (E_{coh}) per DMSO Molecule of the Various Molecular Complexes.

4.4.7 **The monolayer**

The arrangement of the DMSO molecules in the high coverage phase (monolayer) has been also characterized from the theoretical point of view, by means of Density Functional Theory (DFT) calculations, that confirm the hypothesised structure. With concern to the stability of the structure, the adsorption energy (E_{ads}) amounts to 2.06 eV/molecule, whereas the contribution from lateral interactions (E_{coh}) to 0.29 eV/molecule. In figure 4.22a a ball model of the optimized adsorption geometry is shown, while figure 4.22c shows the DFT-based simulation of the STM image, which is in good agreement with the

experimental high-resolution image in panel 4.22b of the same figure. Judging from its structure, the stabilizing interaction within this phase is clearly the intermolecular attractive $CH_3 \cdots O$ interaction, the same already found in the square complex. Therefore it is not surprisingly to find both structures in the same temperature interval (see Figure 4.4).

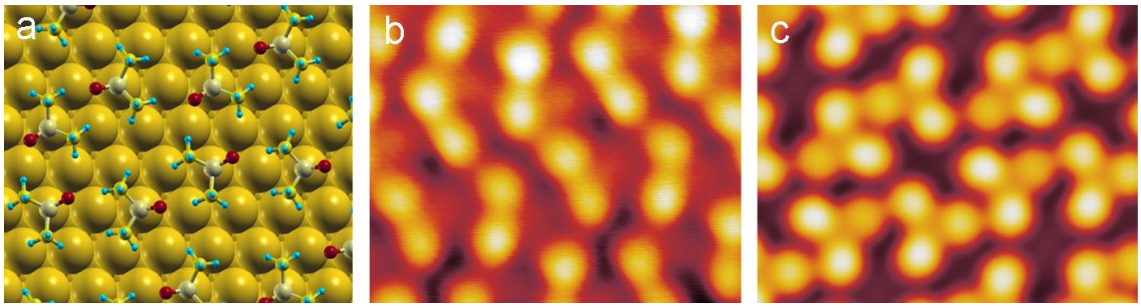

Figure 4.22: (a) stick and ball model for DFT-optimised monolayer and its relative (b) experimental and (c) simulated STM images.

4.4.8 **Conclusions**

In the present chapter, it has been shown that there is a mutual stabilization between a common, polar molecule, DMSO, and native, positively charged adatoms on the Au(111) surface. The existence of these adatoms, whose related features were so far not directly visible in the experimental data, is demonstrated by the agreement between the measured and simulated STM images, as well as by the observed stability of the complexes, that would have otherwise remained unexplained. These adatoms act as ionic linkers between the molecules, thus displaying a behaviour reported up to now only for alkali metal linkers. The broader interest of such mechanism stems from the evidence that, even at low coverage, fabricating discrete structures with high size selectivity can be achieved by exploiting more than just attractive short-range intermolecular interactions (i.e., van der Waals, or H-bonding). In particular, it is gradually becoming clear that monodisperse cluster populations can be obtained if interactions of electrostatic nature are also present, as well as, for

instance, repulsive interactions between parallel dipoles which act on a longer range [80]. The observed mutual stabilization of DMSO and Au is indeed likely related to the strong dipole moment of the molecule and the strong electronegativity of its constituents.

CHAPTER 5

SELF-ASSEMBLY OF TAPP ON GOLD (111)

5.1 Summary

In this chapter, the behaviour of an amino-functionalised porphyrin on a gold (111) surface at various concentrations and temperatures is reported. The chapter follows the same scheme already seen in the previous one. After a brief introduction about the molecule object of the study, the experimental results are exposed; finally, the results of the DFT calculation are shown and rationalized.
The combination of STM experiments and Density Functional Theory (DFT) calculations reveals that, at low density, these porphyrins form chains via their amino-terminations by a donor-acceptor mechanism. Moreover, it has been demonstrated that such porphyrins, when in the acceptor configuration, tend to trap at their centre charged gold adatoms, intrinsically available on the gold substrate. At higher concentration, a compact monolayer phase becomes available instead. Finally, heating the sample up to 700 K, the TAPP molecules show a conformational change already observed in literature on different and more reactive substrates (silver, copper,…), but never on gold. Moreover, observing the STM images, this modified TAPP exhibits a slight protrusion in the middle, which is supposed to be a gold atom. A theoretical model for this structure has been proposed.

5.2 The TAPP molecule

5,10,15,20-tetra(4-aminophenyl)porphyrin (TAPP) (Figure 5.1b and 5.1c) belongs to porphyrins family. The porphyrins belong to a large class of fluorescent pigments of crystalline synthetic or natural origin, characterized by an intense red or purple coloring. They have in common an aromatic macrocyclic system containing 22 π electrons. 18 of them are delocalized on the ring in accordance with the Huckel rule [4n + 2] for the aromaticity (n = 4).

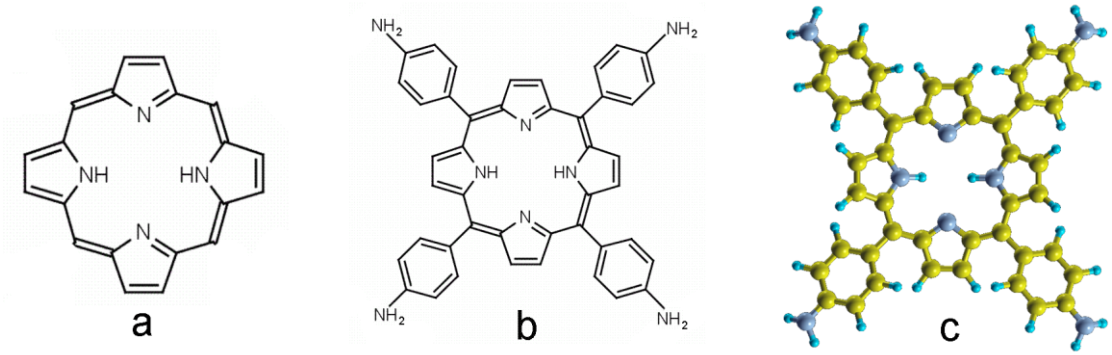

Figure 5.1: Molecular formula of (a) a porphyrin and (b) a TAPP; (c) 3D DFT-optimised model of a TAPP.

The basic structure is called porphyrin and is formed by four pyrrole rings, linked by four methinic carbons on the bridge (Figure 5.1a). The nitrogen atoms of the porphyrin can experience single or double protonation or deprotonation in relatively mild conditions. When deprotonated, porphyrins become perfect sites to host metal ions and non-metallic elements, typical of the XIII-XV group (aluminium, silicon, phosphorus, etc...). The aromaticity is probably the most important reason which makes porphyrins presence so common in natural processes; the ability to delocalise electrons in such a large system offers a good thermal stability and the possibility to be oxidized or reduced easily. It has been demonstrated by NMR analysis, crystallographic and theoretical studies that the two protons inside the macrocycle jump normally between the two opposite couple of pyrrole, forming two degenerates tautomers[81].

5.2.1 **Porphyrins in surface science**

The integration of organic molecules into electronic devices is at the basis of new-concept devices (such as OLEDs, biosensors) and could help to circumvent the limit of the traditional technologies based on semiconductors. Among all the classes of organic molecules, porphyrins have attracted particular attention among the researchers because of their key roles in biological systems, their stability and electronic structure. Porphyrins can be functionalized with a wide range of functional groups and they can incorporate at their centre a metal atom, which is used to modify both the electronic and structural properties of porphyrins. These features make porphyrins suitable for a wide range of potential applications in the fields of catalysis, solar cells, sensors, and electrochemistry [82][83].

Single molecules and self-assembled monolayers of porphyrins on metal surfaces have been widely studied with Scanning Tunneling Microscopy (STM) in literature from both structural and electronic point of view. However, to realise molecular electronic devices, non-periodic assemblies of molecules may be required [84]. For this reason, in the last decade researchers made an effort to understand how to control the assemblies of molecules into the desired organic architecture [82][84][85]. In particular, one-dimensional molecule chains have attracted interest as they are promising candidates to be employed, *e.g.*, as organic wires into organic circuits. The possibility to functionalise the porphyrins opens the perspective for using them as building blocks in several sorts of assembly, especially in organic chains.

5.3 Experimental evidences

Several studies have reported many properly functionalized porphyrins forming chains through hydrogen bond [86]-[88], covalent bond [89],[90], or metal-organic bond [87],[91]-[94]. The functional groups equipping porphyrins

and the interaction of porphyrins with the metal substrate determine the geometric and the electronic structure of such organic chains.

Hydrogen bond based organic chains are of fundamental importance because they are precursor of stronger covalently or metal-organic bonded chains. In particular, primary amines (-NH_2) can establish hydrogen bonds with each other and can interact with a metal substrate via weak bonds involving the electron lone pair of their amino functional group. In particular, the N-Au bond has been employed to form molecule-gold junction for single molecule conductance studies [95]-[97]; at the same time charge transfer between amines and gold substrates have been proved to be promising, showing a very fast N-Au charge delocalization [98].

5.3.1 **LT-STM results**

Experiments have been performed in UHV conditions at a base pressure of 1×10-8 Pa. TAPP has been evaporated from a Knudsen cell at 520 – 570 K on a clean monocrystalline Au(111) sample at room temperature. STM imaging has been performed with a Low Temperature STM, working at a temperature of approximately 4.3 K. Images were acquired at constant current mode.

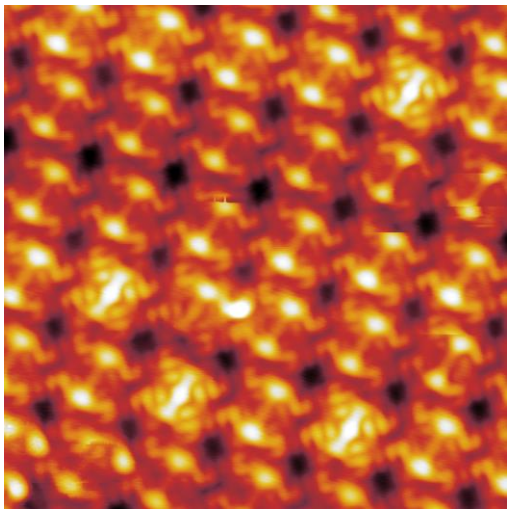

Figure 5.2: Experimental STM image (9.0×9.0 nm^2) showing the high coverage phase of TAPP. Some molecules differs from the other for a bright dot in the middle. Vs= - 1.0 V, It= 200 pA.

At high coverage, the TAPP molecules form a compact monolayer for steric effects like the simple tetraphenylporphyrins (Figure 5.2). In this structure two types of TAPP have been found and one of them shows a bright protrusion in the middle. This is exactly what Mielke et al. [105] observed for tetraphenylporphyrins on Au(111), where brighter molecules were demonstrated to have gold adatoms underneath.

Instead, TAPP forms chains at low coverage, along the herringbone reconstruction of the substrate (Figure 5.3a). Interestingly the TAPP molecules alternate systematically their orientation along the chain(Figure 5.3b).

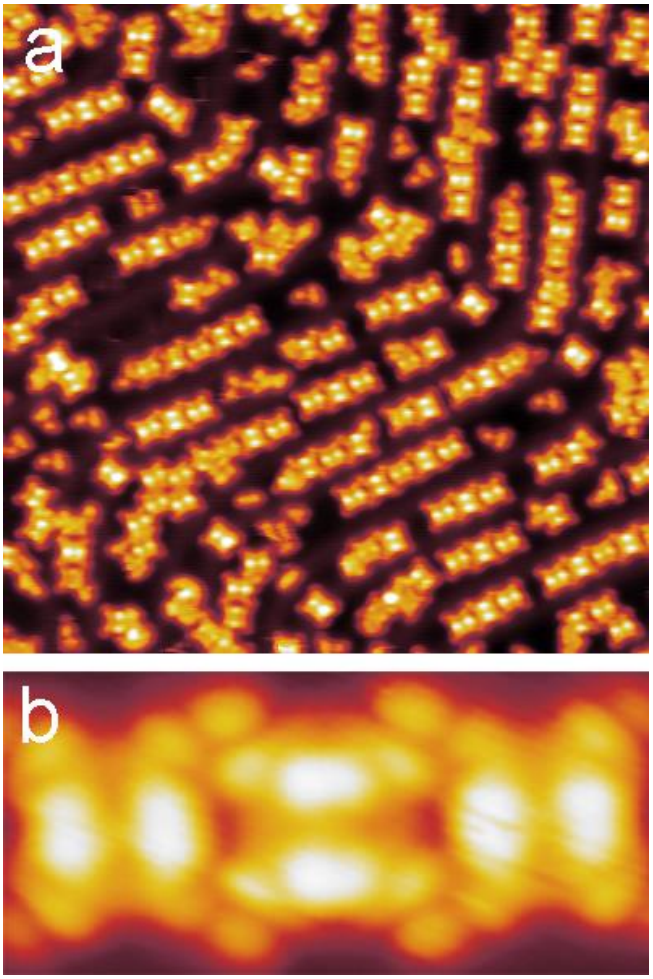

Figure 5.3: Experimental STM images (a) showing the chains of TAPP formed at low coverage phase (40x40 nm^2,) and (b) a particular of a chain (5.0x2.2 nm^2, *Vs*= - 2.0 V, *It*= 300 pA) highlighting the alternation of the orientation of TAPP molecules.

The length of these chains is limited by the herringbone reconstruction of the substrate (see Figure 5.3a) suggesting some weak interactions between the molecules. Moreover, it is easy to remove each TAPP from a chain by STM manipulation: this fact further supports the hypothesis of a weak hydrogen bond between TAPPs. Each azote of an amine has an electron lone pair which can interact with one hydrogen atom of a neighbour amine, or with the gold substrate [97],[99]. For geometrical reasons, the aminophenyl terminations should twist with respect to the others to establish such interactions, as it is known that phenyls of tetraphenylporphyrins have different angles with respect to the porphyrin plane both in gas phase and on metal surfaces [100]-[103]. More interestingly, often the TAPP molecules in the chain appear alternately different suggesting the existence of two different "states" of molecules, as already observed for the monolayer (compare Figure 5.4 with Figure 5.2).

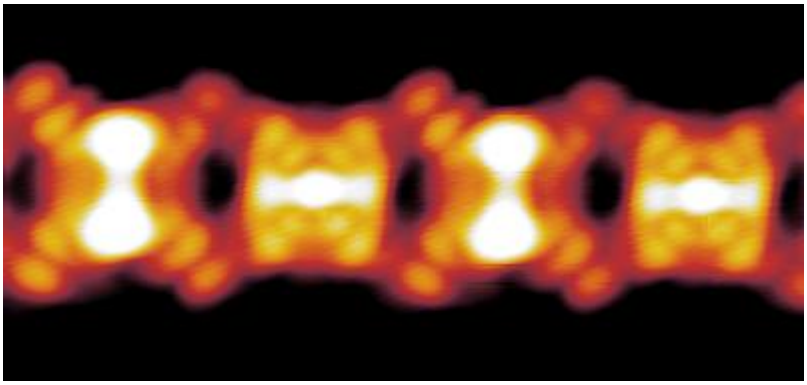

Figure 5.4: Experimental STM image showing a detail of the chain (6.4x3.0 nm^2, Vs= - 1.0 V, It= 300 pA) highlighting the systematic alternation of two different types of TAPP molecules.

To understand the self-assembly mechanism of the chains and the origin of the bright protrusion in some TAPP molecules, Density Functional Theory (DFT) calculations of the structural, electronic, and energetic properties of the observed TAPP adsorption structures as well as simulations of the STM images have been carried out.

5.4 Computational modelling

5.4.1 **Technical aspects**

Also for this chapter, DFT calculations were performed with the plane-wave pseudopotential package QUANTUM ESPRESSO using a GGA-PBE ultrasoft pseudopotentials. The wave function energy cut-off has been fixed at 408 eV. Considering the large size of the cell, the Brillouin-zone sampling included only the gamma point. As already done in CHAPTER 4, after a first test phase, since van der Waals interactions play a non-negligible role in self-assembled organic structures, the calculations have been performed including the semi-empirical dispersion-corrected DFT (DFT-D) method proposed by Grimme.

The Au(111) surface was modelled with three layers for the simulations of the single TAPP molecule and only two layers for the chain, allowing in both cases a vacuum (adlayer-surface) distance of ≈1.4 nm. For the single TAPP adsorption, the bottom layer of the surface has been kept fixed at the bulk Au calculated values to mimic the behaviour of the metal substrate. For the chain model, the two gold layers have been kept fixed, except for the gold atom underneath the middle of the two porphyrins. The forces were relaxed up to 0.26 eV/Å. STM images were simulated within the Tersoff-Hamann approximation and elaborated to be comparable with experimental "constant current" STM image, as already explained in paragraph 4.4.1 . The images in this paragraph were simulated at various biases, at an ILDOS value for the iso-surface of 4×10^{-3} nm^{-3}, lying at an average distance of approximately 0.5 nm from the first atomic layer. Ball models are rendered with the XCrySDen software packages.

5.4.2 **Singole TAPP molecule adsorption**

The study started from the model of the adsorption of a single TAPP molecule on gold (111) surface. Using as prototype a gas-phase optimized molecule, we

tested several adsorption geometries and sites. In Table 5.1 a comparison between the energy of the main different simulated systems is reported. Comparing the energies, the most stable structure is the so called α-TAPP that has a saddle-shaped macrocycle, where pairs of opposite pyrrole rings are tilted upwards or downwards, with the two internal hydrogen located on the two upwards tilted pyrroles, which we thus name H-pyrroles (Figure 5.5). The aminophenyl terminations, on the contrary, are slightly twisted with respect to the surface plane.

.

Adsorption configuration	ΔE [eV]
α-TAPP	-
β-TAPP	0.21
α-TAPP – tilted by 14°	0.41
β-TAPP – tilted by 14°	0.33

Table 5.1: Calculated differences in energy between various adsorption systems of TAPP on gold (111).

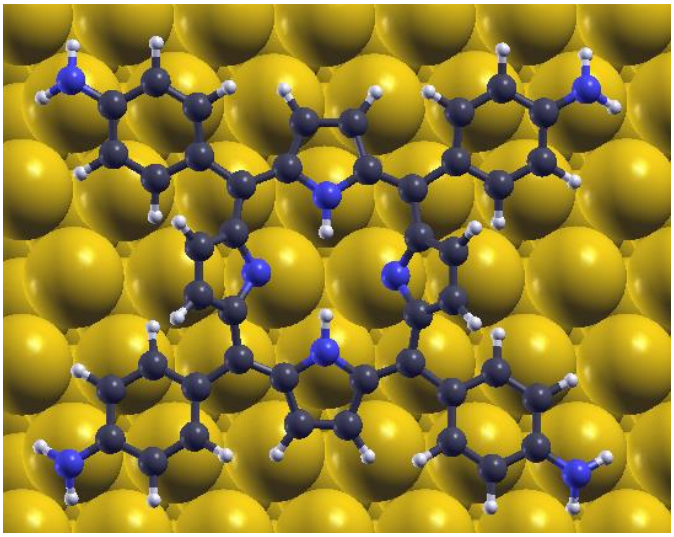

Figure 5.5: top view of stick and ball model for the α-TAPP molecule on Au(111) substrate obtained by DFT calculation.

This result is in perfect agreement with the literature, since the saddle-shaped macrocycle and the tilted phenyls are typical characteristics of phenyl-porphyrins adsorbed on metal surfaces[101],[104]. Also the orientation of the

axis of the most stable computational model for TAPP is in perfect agreement with the experimental observation. Indeed the TAPP molecules results to be always aligned with direction equivalent to $[1\bar{1}0]$ and $[11\bar{2}]$, independently of whether they are alone, in chains or in a compact monolayer (Figure 5.6).

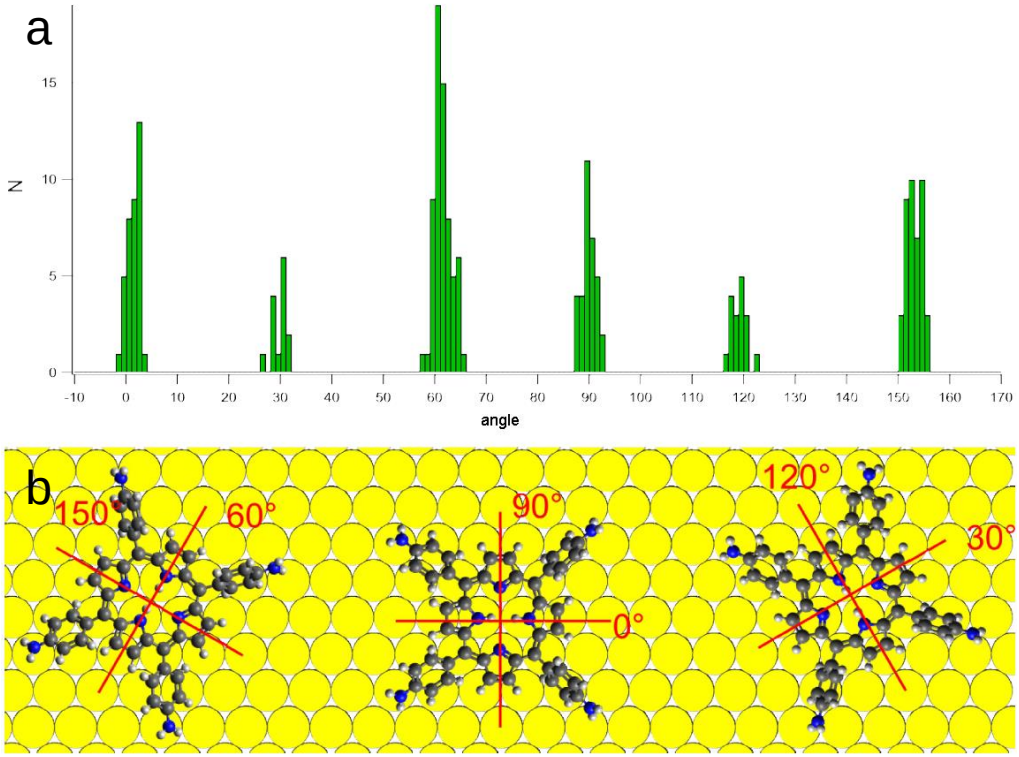

Figure 5.6: (a) histogram with statistic distribution of the orientations of the molecules respect to the surface: the TAPP are always oriented along the symmetry directions of the substrate equivalent to $[1\bar{1}0]$and $[11\bar{2}]$; (b) representation of the orientation of molecules respect to the surface.

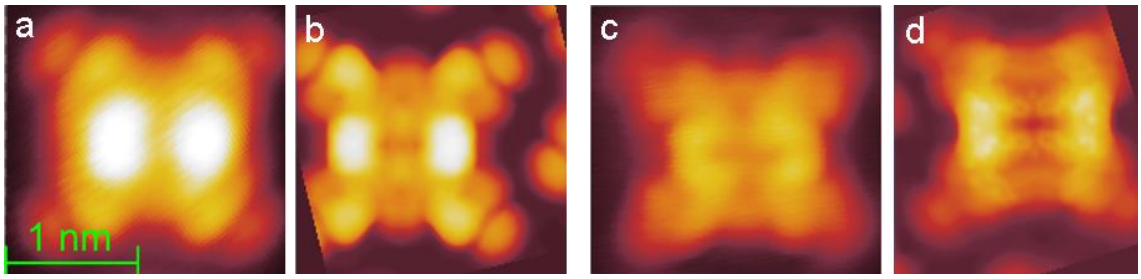

Figure 5.7: Experimental (a,c) and simulated (b,d) STM images of a single TAPP adsorbed on gold (111) at various biases. (a) *Vs*= - 1.0 V, *It*= 300 pA, (c) *Vs*= + 1.0 V, *It*= 300 pA

Finally the experimental and simulated STM images have been successfully compared (Figure 5.7), so the α-TAPP has been used as starting point for the further calculations. It should be noted that the compatibility of the simulated and experimental STM images is in this case a necessary but not sufficient criterion. Indeed the different adsorption configurations of TAPP, summarised in Table 5.1, are not distinguishable from the bare STM simulated images.

5.4.3 **TAPP monolayer**

Firstly the high coverage phase (monolayer) of TAPP has been characterized from the theoretical point of view, by means of DFT simulations. The calculations confirm the hypothesised structure. The TAPP molecules, if analysed individually, shows an alignment with the directions $[1\bar{1}0]$and $[11\bar{2}]$. At long range however, the monolayer is clearly characterised by two perpendicular directions, inclined by 21° with respect to the above mentioned directions, as shown in Figure 5.8.

The unitary cell, highlighted in green in Figure 5.8 and 5.9 is determined by two vectors defined as:

$$\begin{pmatrix} \vec{b}_1 \\ \vec{b}_2 \end{pmatrix} = \begin{pmatrix} 4 & 2 \\ -1 & 8 \end{pmatrix} \begin{pmatrix} \vec{l}_1 \\ \vec{l}_2 \end{pmatrix} \tag{5.1}$$

with the Au(111) unit cell vectors being defined as $\vec{l}_1 = a_0(1;0)$and $\vec{l}_2 = a_0(\frac{1}{2};\frac{\sqrt{3}}{2})$

In figure 5.9 a ball model of the optimized adsorption geometry is shown; figures 5.10b and 5.10d show the DFT-based simulation of the STM images, which are in good agreement with the experimental high-resolution images in panel 5.10a and 5.10c of the same figure. The TAPP molecules have weak lateral interaction with the other molecules of the monolayer. The driving force for the monolayer formations, as already hypothesised for other tetraphenyl-porphyrins, seems to be a purely steric effect.

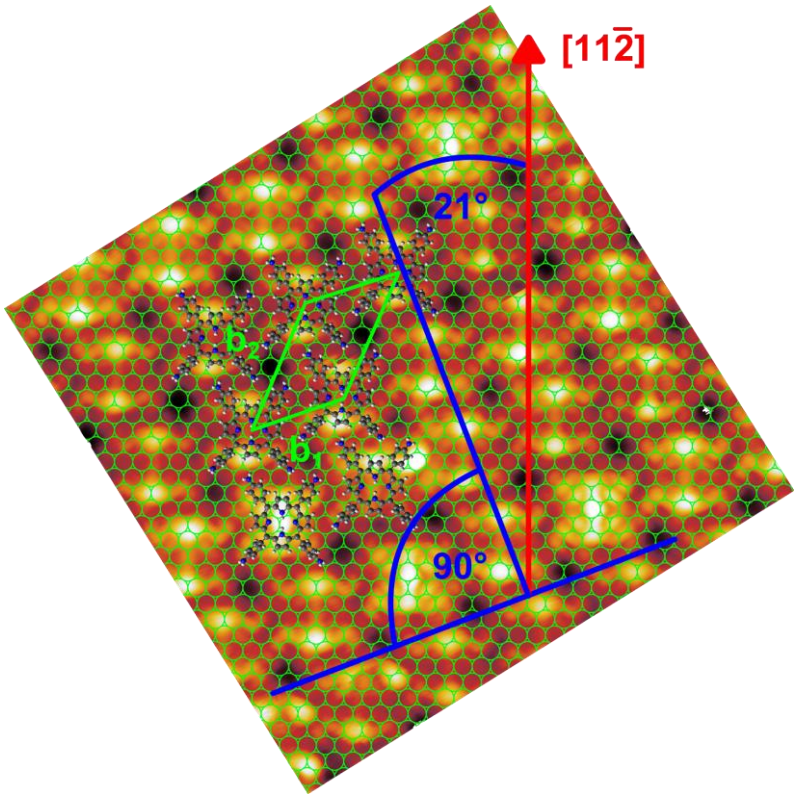

Figure 5.8: model of the monolayer of TAPP overlaying an STM experimental image. The blue lines emphasize both directions that characterize the monolayer: these are perpendicular to each other and are about inclined 20/21° respect to the directions$[1\bar{1}0]$and$[11\bar{2}]$ of the Au (111). The unit cell of the proposed model is in green with the basis vectors b_1 and b_2.

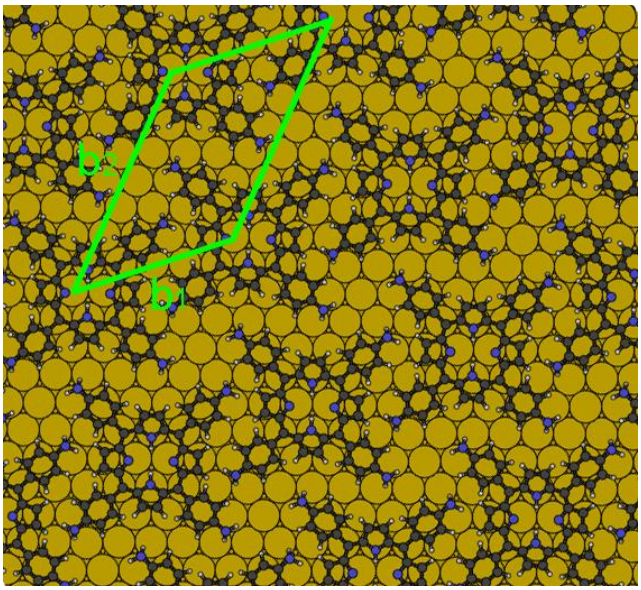

Figure 5.9: stick and ball model for DFT-optimised monolayer. The unit cell of the model is highlighted in green.

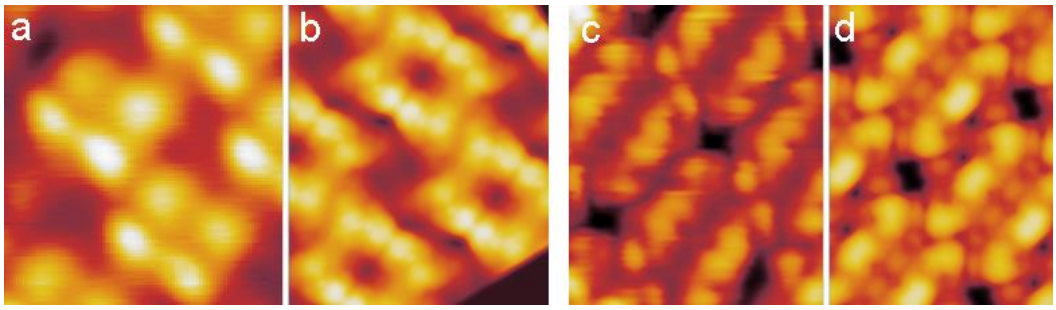

Figure 5.10: Experimental (a,c) and simulated (b,d) STM images (2.8x3.2 nm^2) of monolayer phase of TAPP adsorbed on gold (111) at various biases. (a) Vs= + 1.0 V, It= 200 pA, (c) Vs= - 2.0 V, It= 200 pA.

5.4.4 **The amphiprotic behaviour of TAPP**

Subsequently, the focus has moved to the chain structure. To reproduce the system the unit cell has been optimized to contain two TAPP molecules. These molecules are in one direction close to the other, at a distance compatible with the experimental one, whereas in the other direction, they are divided by ~7 Å from the periodic images. In this way the model represents an ideal endless TAPP chain. After having analysed many possible configurations (Table 5.2), the conclusion is that the most stable one, shown in Figure 5.11, is obtained by placing two α-TAPP molecules, one perpendicular to the other. In that way, the two opposite H-pyrroles directions inside the two α-TAPP result to be perpendicular. Indeed, in this configuration, the aminophenyl terminations tilt into geometry that favourites the interaction of amino terminations of the two neighbour molecules.

Adsorption configuration	ΔE [eV]
α-TAPP + α-TAPP	-
α-TAPP + β-TAPP	0.01
β-TAPP + α-TAPP	0.07
β-TAPP + β-TAPP	0.17

Table 5.2: Calculated differences in energy between various adsorption systems of TAPP chain on gold (111).

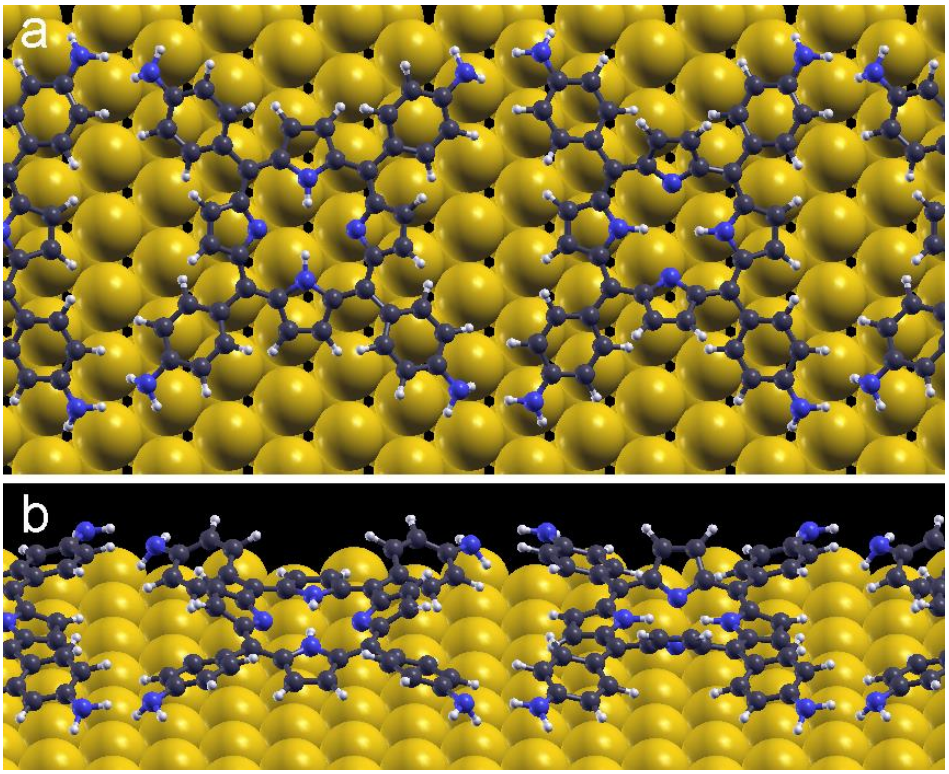

Figure 5.11: (a) top and (b) perspective view of stick and ball model for the chain formed by two α-TAPP molecules on Au(111) optimised by DFT calculations.

The DFT simulations confirm thus our initial hypothesis, showing the lone pair of a N atom of the TAPP on the left (Figure 5.11) interacting with a proton of the amino group of the TAPP on the right, establishing an amino-amino hydrogen bond. Moreover it is clear that in a TAPP chain, each molecule behaves alternately as acceptor (Figure 5.11, left TAPP) or donor (Figure 5.11, right TAPP) as a whole, i.e., TAPP has an amphiprotic behaviour in such chains.

As already done for the *triangle* structure of the DMSO in paragraph 4.4.4, some post processing analysis have been performed. First, an ideal gas phase chain has been analysed, with the aim to focus on the molecule-molecule interaction. DFT calculations confirm the formation of hydrogen bonds between the amino-groups, as shown by the charge density transfer plots in Figure 5.12a and 5.12b: the red arrow highlights the electron lone pair of the amines which are exposed. Moreover, by integrating the charge transfer in sections, perpendicularly to the chain, (Figure 5.12c) it has been demonstrated that the acceptor molecule results

to be globally positively charged, whereas the other one shows an opposite behaviour.

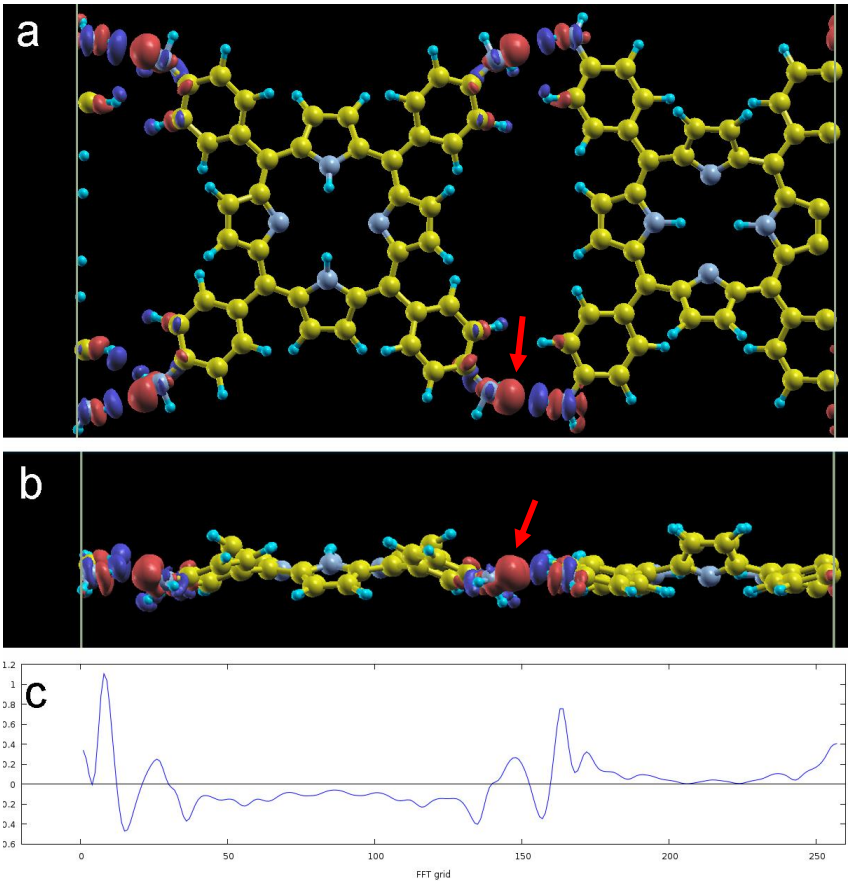

Figure 5.12: The formation of four hydrogen bond evidenced in the top (a) and side (b) views of the changes in charge density in an ideal gas-phase chain of TAPP molecules. The accumulation of negative charge is depicted in red, the depletion in blue. The red arrow highlights the electron lone pair of the amine exposed. (c) Integral of perpendicular sections of the charge transfer.

5.4.5 **The role of adatoms in chain formation**

After having identified the driving force for the chains formation, the attention has been moved to the TAPP that has a different appearance, a "brighter" lobe in the middle. These kind of molecules have been sometimes found in the monolayer (some of them are visible in figure 5.2), and systematically as acceptor molecule of the chain. Figure 5.13 shows an experimental STM image where two acceptors have different appearances: the first one, named from now

on acceptor-1, appears similar to its neighbour donor TAPP, while the second one, named acceptor-2, have a bright protrusion at its centre.

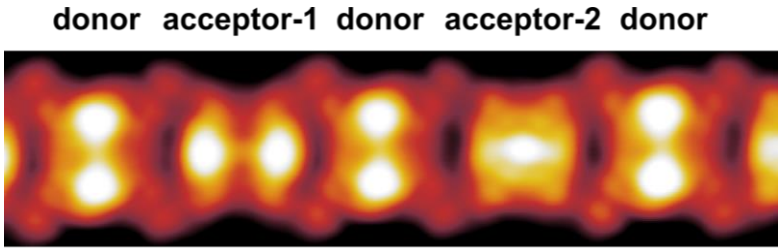

Figure 5.13: Experimental STM image (9.0.0x2.3 nm², *Vs*= - 1.0 V, *It*= 200 pA) of a TAPP chain showing an acceptor-1 and an acceptor-2.

Firstly, all possible conformational explanations have been excluded. Indeed, the only donor-acceptor states or the adsorption geometry (α- or β-TAPP) cannot explain this remarkable difference in the appearances of the acceptors and donors. Then, by searching in the literature, a more intriguing hypothesis has been taken into account. In a recent work, Mielke *et al.*[105] demonstrated that gold adatoms can be trapped underneath porphyrins on Au(111). In their STM images, they find two types of porphyins: "bright" and "dark", and they show that the "bright" porphyrins have a gold adatom underneath. This is similar to what it has been observed in our experimental STM images: most TAPP acceptors are "brighter" than the few others because they (likely) trap one gold atom underneath. Indeed, at temperature higher than 250 K, native gold adatoms are normally diffusing on Au(111) surface. As already seen in chapter 4, such adatoms are charged due to their undercoordination, and can detach from the surface steps, diffuse along them and across the surface terraces, where they can interact, *e.g.*, with molecules with cyano (CN) groups [94],[106]-[109]or sulfur [110],[111]. In this case, as shown in the model of Figure 5.14a, a TAPP can bind one gold adatom at its centre, with N atoms of two pyrroles coordinating to the adatom.

The simulated STM image (Figure 5.14c) is in good agreement with the experimental one.

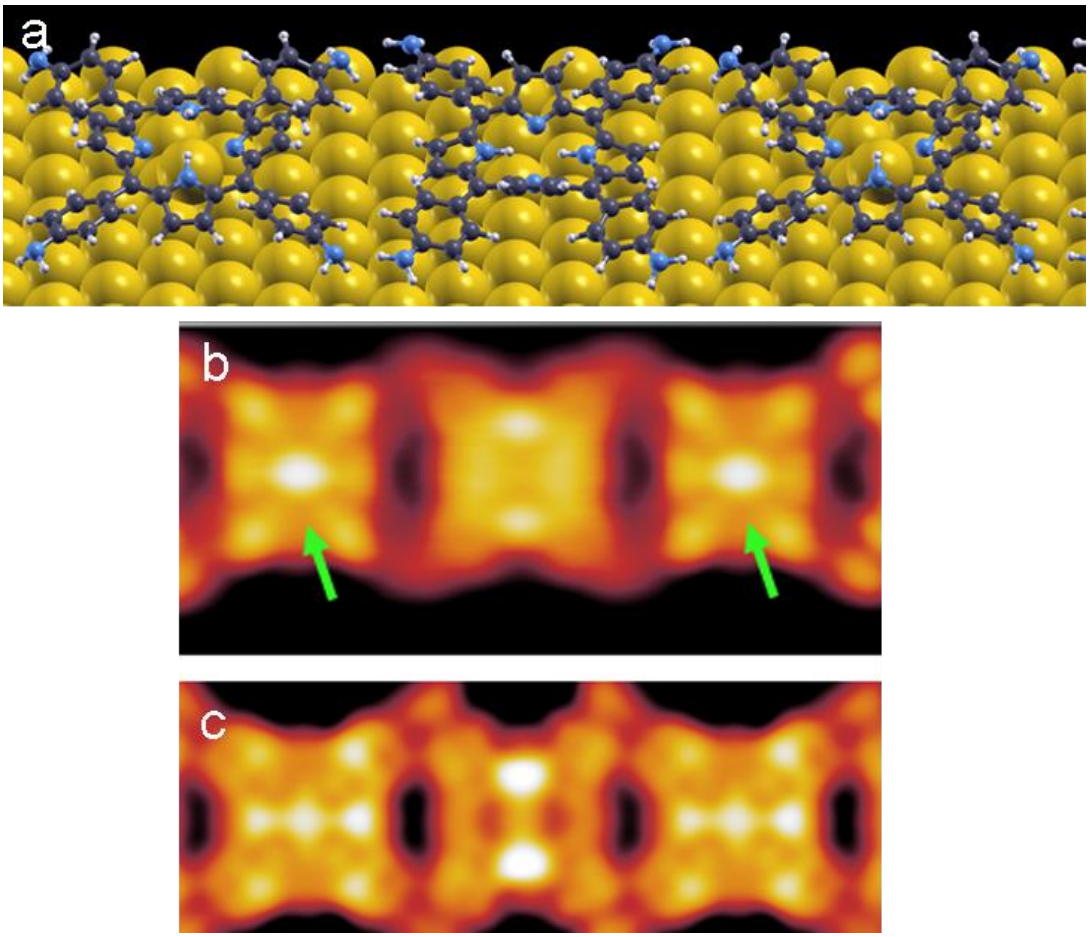

Figure 5.14: (a) stick and ball model for DFT-optimised chain of TAPP with gold adatoms trapped beneath the acceptor-2 molecules (b) experimental 5.2x2.5 nm^2, *Vs*= - 0.1 V, *It*= 300 pA) and (c) simulated STM images. With green arrows are highlighted the bright dots caused by the presence of gold adatoms.

To verify the stability of the structure proposed, its adsorption energy E_{ads} (calculated with the formula (4.3)) has been compared with the one of the chain without adatom. The energetic gain of 1.30 eV confirms that a gold adatom, if already present on the surface, is more stable when trapped under a TAPP molecule than alone on the surface. Moreover, the adatom results more stable (0.23 eV) under the acceptor TAPP than under the donor one, explaining in that way why they have never been experimentally found under a donor TAPP molecule. This energetics analysis allows a clear interpretation of the experimental picture: the driving force of the chains formation is the interaction

between the amino groups and it is independent from the presence of gold adatoms. But if native gold adatoms are already available on the surface, they are much more stable if trapped under the acceptor molecules of the chain.

5.4.6 **Deprotonation of donor molecules**

Another peculiarity of the chain structure has been evidenced by a manipulation experiment on the donor molecule: through a voltage pulse it's possible to remove one proton from inside the macrocycle, to induce the remaining proton to jump to the opposite pyrrole (tautomerisation) or to remove both protons (Figure 5.15). On the contrary on the acceptor molecule, no evidence of deprotonation or tautomerisation was observed.

All deprotonation state of the donor molecule has been modelised and optimised by means of DFT calculations (Figure 5.16).

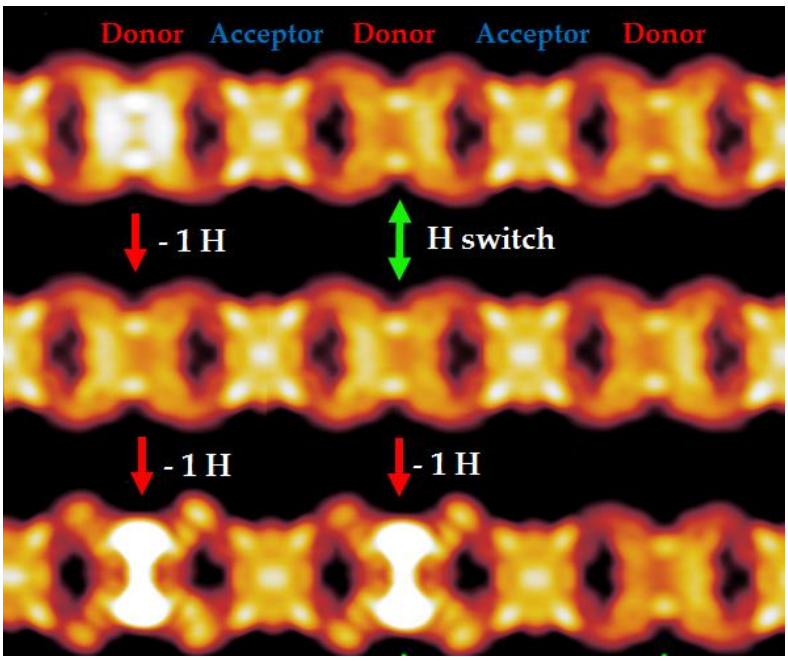

Figure 5.15: Experimental STM images highlighting the effect of voltage pulses on a TAPP chain. The donor molecule can be deprotonated once, the proton can be switched between the two opposite pyrroles or can be deprotonated twice. On contrary, the acceptor-2 molecule never change.

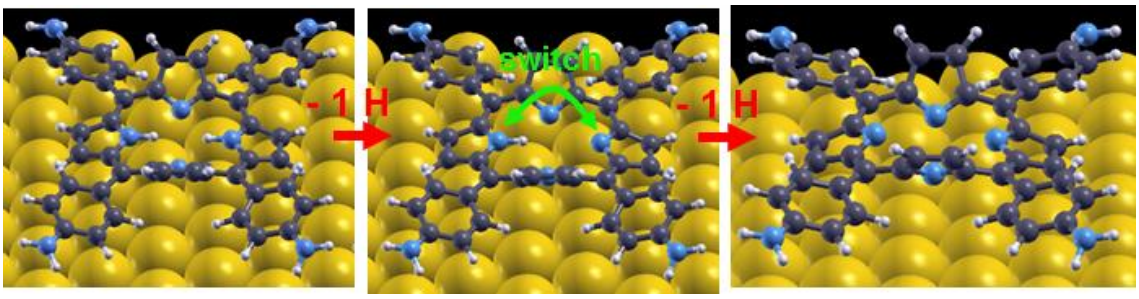

Figure 5.16: stick and ball models for DFT-optimised donor molecule evidencing the possible deprotonation states of the TAPP.

To explain the discrepancy of the behaviour of donor and acceptor molecules, a spontaneous metalation process of the acceptor TAPP has been considered.

Indeed, metalation process of porphyrins have been widely studied in literature, especially their self-metalation on metal surfaces, such as Cu, Fe or Ni [113]-[117] and their direct metalation by evaporation of metal atoms on the surface [118]-[120]. However, in this case TAPP acceptors-2 do not metalate, but rather trap one gold atom underneath, via a coordination bond with. Indeed, the simulated STM image of the model in which the acceptor is metalated does not match the experimental ones. This conclusion is supported by the literature, where no study of direct metalation with gold atoms of porphyrins on surfaces has been reported till now.

Therefore, in order to explain the impressive stability of the acceptors-2, the charge transfer calculation already done (see paragraph 5.4.4) for a gas phase chain, has been replicated for the adsorbed structure (Figure 5.17). From the top view in panel 5.17a, the electron charge accumulation (red lobes highlighted by green arrow) on the gold adatom is clearly visible, suggesting a strong interaction between gold and the porphyrinic cycle. Such kind of interaction could justify the great stability of the acceptors-2 molecule. Moreover, observing the electron charge accumulation (the red arrow in Figure 5.17) on the gold surface, it is clear that the amine terminations not only form hydrogen bonds between TAPP molecules, but also strongly interact with the substrate, conferring to the chain a good stability.

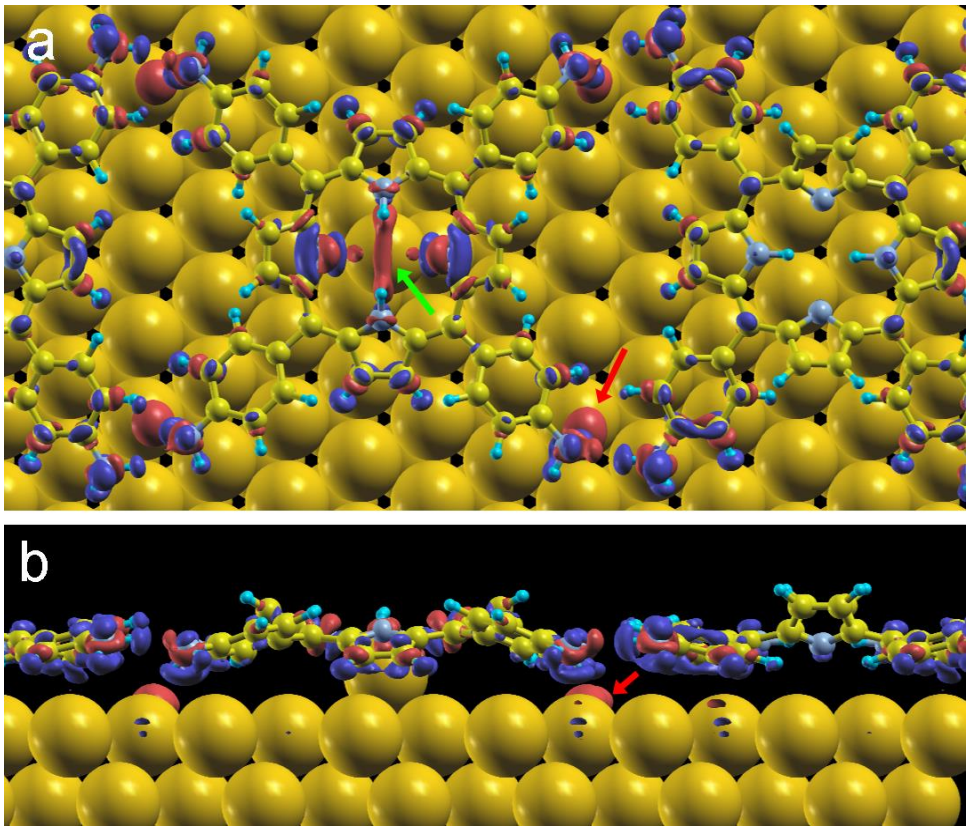

Figure 5.17: The adsorption mechanism of a chain in the top (a) and side (b) views of the changes in charge density. The accumulation of negative charge is depicted in red, the depletion in blue. The green arrow evidences the interactions between adatom and pirroles of the acceptor-2 TAPP. The red arrows highlight the electron the interactions between amine and gold substrate.

5.4.7 **TAPP behaviour at high temperature**

In the last part of the study the behaviour of the TAPP molecules at high temperature has been analysed.

When heating the monolayer at 580 K, some molecules started to detach from the compact phase and to change their morphology completely (green arrow in Figure 5.18).

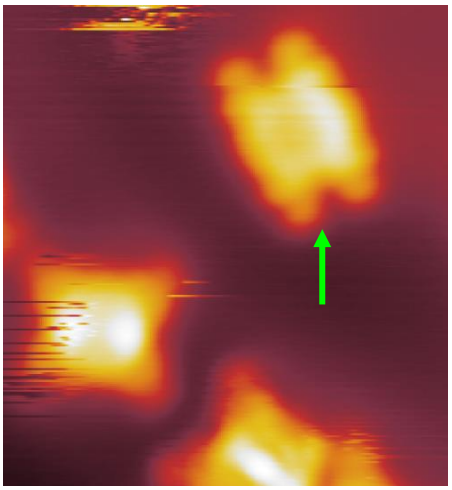

Figure 5.18: Experimental STM image taken at 580 K showing (green arrow) a deformed TAPP molecule, compared to other normal (7.0x7.2 nm^2, Vs= - 1.0 V, It= 300 pA) .

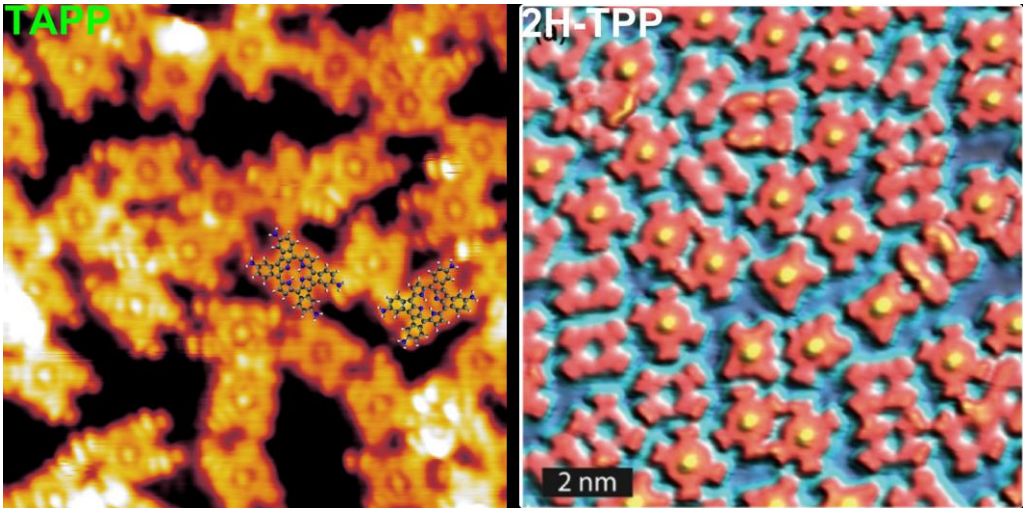

Figure 5.19: Experimental STM images of (left panel) deformed TAPP molecules on Au(111) after an annealing at 680 K and of (right panel) 2H-TPP on Ag(111) after an annealing at 550 K: some 2H-TPP are "empty", while others have a Ru atom in the middle [119].

This process increases with the temperature, up to an annealing temperature of 670 K, when there are no more compact zones but only deformed TAPP, arranged randomly on the surface (Figure 5.19 left panel). Di Santo et al. [120], by studying the 2H-Tetraphenylporphyrin (2H-TPP) on Ag (111), have found a similar situation. In their work they explained the deformation with a deprotonation and a subsequent binding of some phenyls and pyrroles, as

shown in Figure 5.20. Moreover, the deformed TAPP molecules have another peculiarity: most of them seem to have a bright dot in the centre. Papageorgiou et al.[119] studied the 2H-TPP on Ag (111) and then deposed an atom of ruthenium in the centre of these porphyrins. As shown in the right panel of the Figure 5.19, the 2H-TPP molecules without Ru atoms in the centre appear empty in the middle, while those with a Ru atom show a bright protrusion in the centre, just like the deformed TAPP, experimentally observed on gold. This could be an indication that a gold adatoms has been adsorbed in the inner porphyrinic cycle (self-metalation).

In literature several cases of self-metalation of porphyrins are reported on more reactive surfaces like copper, nickel, iron [113]-[117]; however self-metalated porphyrins on gold have been never reported, possibly because of the molecules evaporation before the deprotonation and the subsequently deformation. In this case, the strong interaction between amine groups and gold surface probably stabilise the TAPP molecules at a temperature which is high enough to allow the deformation and the metalation.

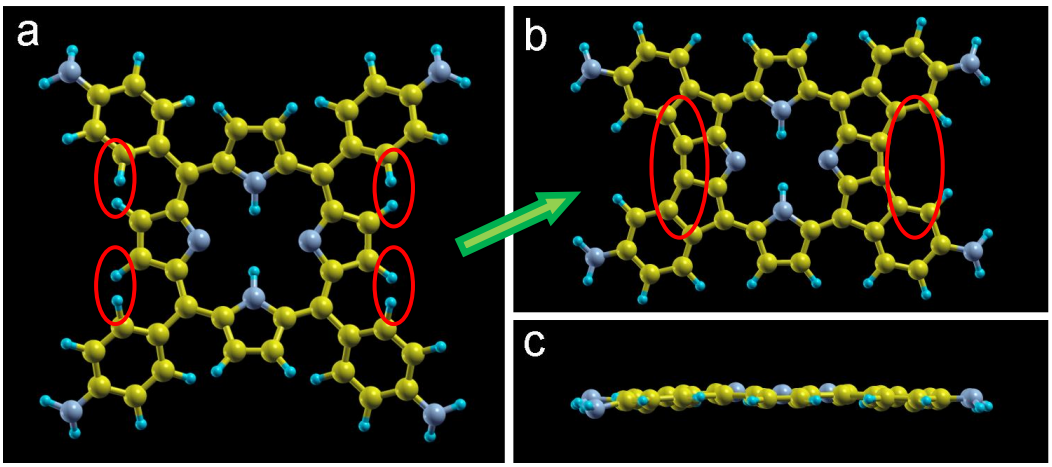

Figure 5.20: Stick and ball DFT-optimized models of that explains the formation of a deformed TAPP molecule ((b) top and (c) side view) starting from a normal one (a). The deformation is caused by the deprotonation of some phenyls and pyrroles (circled in red) and their subsequently bonding, as hypothesised by Di Santo et al. [120].

Therefore, as reported in Figure 5.21a, a DFT theoretical model has been proposed and optimised. The deformed TAPP molecule results completely flat (Figure 5.20c). As clearly shown in the charge transfer calculation of Figure 5.22, the gold adatom forms an organometallic bond with the four equivalent N atoms of the pyrroles. The simulated STM image (Figure 5.21c) is in good agreement with the experimental one, suggesting the correctness of the model (Figure 5.21b).

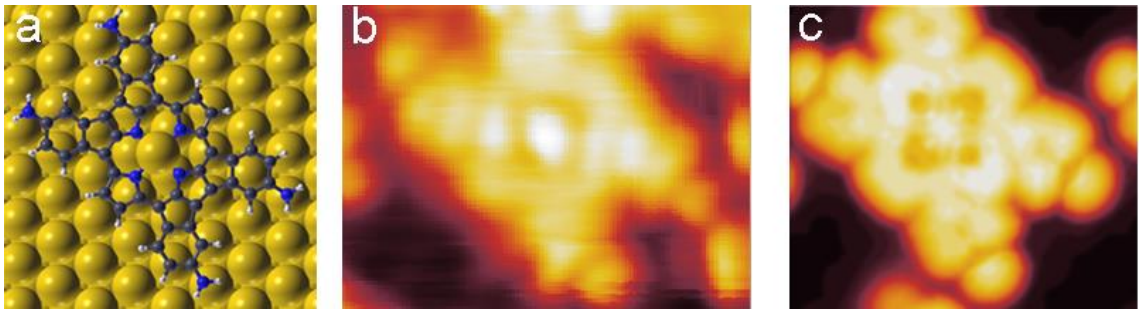

Figure 5.21: (a) stick and ball model for DFT-optimised deformed TAPP, metalated by a gold adatom; its relative (b) experimental and (c) simulated STM images. In both STM images is clearly visible the bright dot caused by the presence of gold adatom.

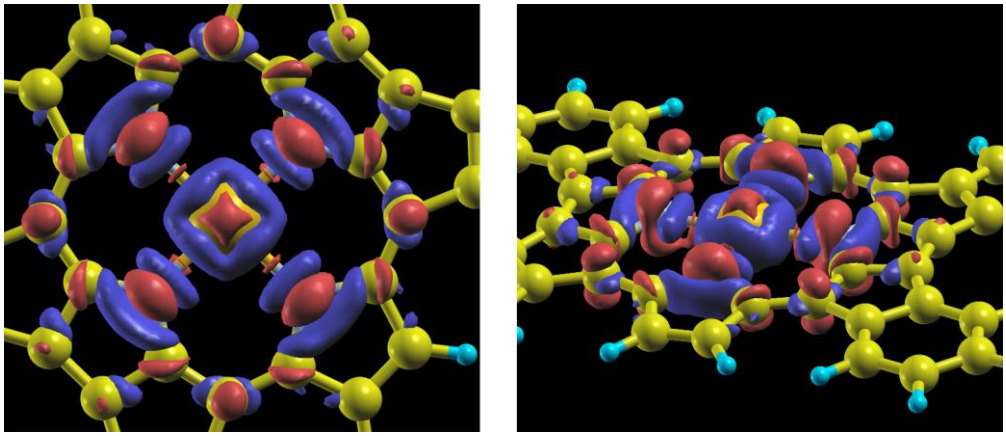

Figure 5.22: (a) Top and (b) perspective view of the changes in charge density for a modified TAPP, metalated by a gold adatom. The accumulation of negative charge is depicted in red, the depletion in blue.

In order to obtain a definitively confirm of the self-metalation of the deformed TAPP molecules on gold (111), some photo-emission experiment (i.e. XPS, etc…) are planned in the near future. Indeed, without a metal atom at the

centre, the four N atoms of the pyrroles would be two by two inequivalent and would have two emission peaks at different energies. If the gold atom were at the centre instead, all 4 nitrogens, bonded to the adatom, would be energetically equivalent.

5.4.8 **Conclusions**

In the present chapter, the study of an amino-functionalized porphyrin (TAPP) on Au is reported (111). At high coverage, the classic monolayer, already observed for other porphyrins, has been found. On the other, at low coverage, the surface is dominated by chain structures, stabilised by the interplay between the amino-amino and amino-gold interaction. Combined experimental STM images and DFT calculations demonstrate that TAPP forms such chains via hydrogen bond between their amino terminations. Inside a chain, each TAPP alternately behaves as acceptor or donor as a whole. Moreover, in STM images, most acceptors show at their centre a bright protrusion, which has been demonstrated to be induced by a gold adatom, trapped beneath the molecule. This adatom coordinates the TAPP via two pyrroles and stabilises the H-pyrroles preventing their deprotonation via voltage pulse.

Finally, studies at high annealing temperature of the monolayer reveal probably for the first time a self-metalation of a porphyrin on a gold substrate. This last hypothesis needs however more experimental data to be confirmed.

CHAPTER 6

LOW COVERAGE SELF-ASSEMBLY OF CA ON GOLD (111)

6.1 Summary

In this final chapter, the study of the adsorption at low coverage of the cysteamine (CA, a small thiol with an amino termination) on a gold (111) surface is reported. Hereby, after a brief introduction about the molecule, the experimental results are exposed, followed by the result of the DFT calculation. Whereas the monolayer has been already analysed in literature, this study reveals peculiar structures composed by two or three CA molecules. By means of experimental techniques (STM and XPS) and DFT calculations, it has been demonstrated that the presence of gold adatoms on the surface induces a drastic modification in the adsorption geometry of the CA.

6.2 The CA molecule

Cysteamine (2-aminoethanthiol) is an organic compound having the molecular formula $HSCH_2CH_2NH_2$; it is a small thiol functionalized with $–NH_2$ termination (Figure 6.1). The Ca molecule, once deposited, allows to obtain a self-assembled monolayer (SAM) that can be exploited as a linker between metal surfaces and simple or complex molecules [121]. Some experiments were carried out for this purpose and complex molecules such as proteins, nano-

clusters and biomolecules have been successfully linked to surfaces of noble metals (e.g. gold or silver) by means of a cysteamine SAM [122]. Indeed, the thiol group reacts chemically already at 300 K, due to its high affinity with the noble metals, whereas the substrate gives rise to a strong metal-sulfur covalent bond.

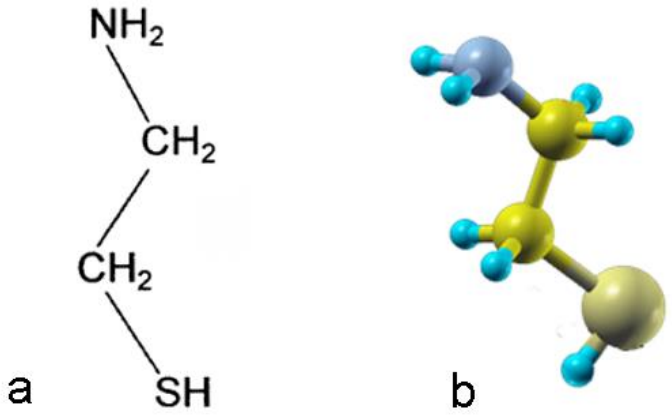

Figure 6.1: (a) Molecular formula of cysteamine (CA); (c) 3D DFT-optimised model of gas phase CA.

The amine on the other side, once the molecule is adsorbed and if it does not form bonds with other molecules or with the substrate, can be used to anchor to the surface other functional molecules with one or more carboxyl groups. In that way the amino-carboxylic interaction can be exploited to form a hetero-molecular structure [123] or to anchor proteins to surfaces in biosensors and biocompatible devices [124], [125].

The substrate and the cysteamine SAM preparation technique determine the density of the molecules that expose the amine termination [126], and thus the degree of functionalization of the surface.

6.3 Experimental evidences

The commonly used technique for forming a SAM consists in the immersion of a metal substrate in a solution in which there are one or more solvents in addition to the molecule that has to be deposited (cysteamine in this case) [127]. Measures through Surface Enhanced Raman Spectroscopy (SERS) have led to hypothesise the existence of two conformations of the molecule of cysteamine in SAM grown in solution called *trans* and *gauche*[126],[127]. A schematic representation of the two conformations is showed in figure 6.2. The main differences between the *trans* and *gauche* conformations is that in the first one the molecule is in an upright position on the surface with amine termination pointing upwards and does not interact with the substrate, while in the second the molecule is lying on the surface and the amine termination interacts with the substrate. In order to get better knowledge of the structural properties of the SAM, a characterization by STM was carried out. The images show a single layer of molecules with highly ranked domains. But the most interesting information is that the presence of the two cysteamine conformations on the surface was confirmed. The presence of molecules in the *gauche* conformation and the proliferation of defects, due to co-adsorption of molecules of the solvent [128] are unwanted characteristics of the SAM obtained. Indeed it greatly reduces the number of amino groups available for anchoring a second layer of molecules via the interaction amino- carboxylic.

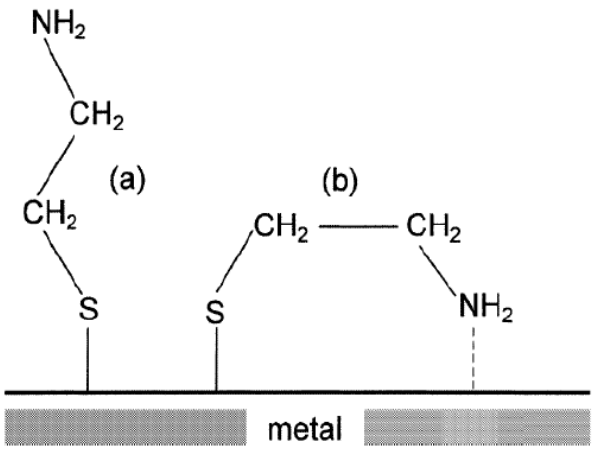

Figure 6.2: Schematic representation of cysteamine molecule adsorbed in (a) *trans* and (b) *gauche* conformation [126].

To overcome these problems, Cossaro et al. [129] in 2010 deposited at room temperature a monolayer of cysteamine on gold (111) in UHV. Working under these conditions indeed allows an extremely precise characterization of this system, compared to the studies carried out in solution. If we change the monolayer preparation method, it is possible that this assumes some of the different characteristics described in the previous work.

Cossaro et al. have characterized the monolayer obtained by in-situ measurements of high-resolution XPS and NEXAFS. In this study, they they were able to prepare a high density monolayer of cysteamine, homogeneous and compact, in which most of the amine termination are in a neutral state, turned up with respect to the surface. These features make the monolayer of cysteamine, prepared by evaporation in UHV, an excellent candidate, useful to anchor a second layer of molecules.

6.3.1 **STM results**

Also in this work the deposition has been carried out in UHV condition at room temperature. At 300 K indeed the system has enough energy to break the S-H bond of the CA and subsequently to chemisorbs the molecule.

At very low coverages the molecules are located only in the *fcc* areas of the sample (Figure 6.3a) and they are clearly combined in complexes composed by

two or three CA molecules (Figure 6.4). With increasing coverage, these complexes invade the other areas of the surface, destroying in fact the "herringbone" reconstruction (Figure 6.3b and 6.3c). Indeed thiols are known to induce deep restructuring of the gold surface by covalently binding to this substrate.[130]-[132].

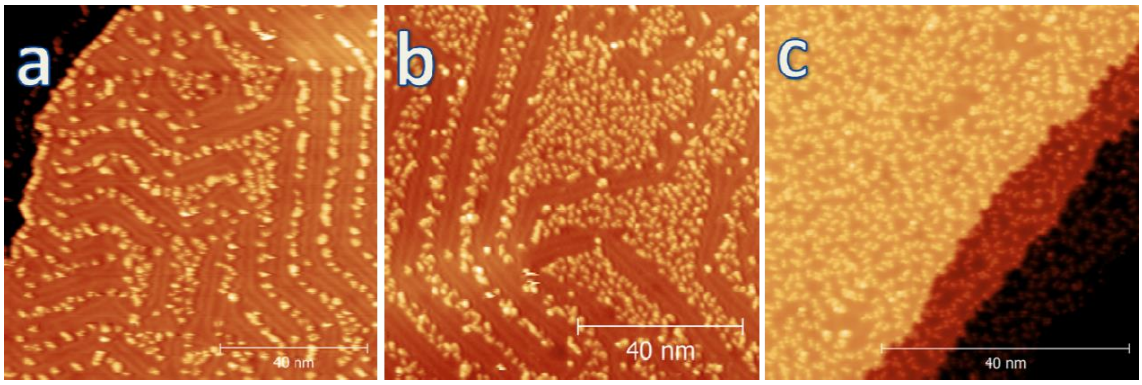

Figure 6.3: Experimental STM images of CA adsorbed on Au (111) in UHV conditions at increasing coverages. In panel (a) the herringbone reconstruction is still present, in panel (b) start to disappear in some areas, whereas is completely destroyed in panel (c).

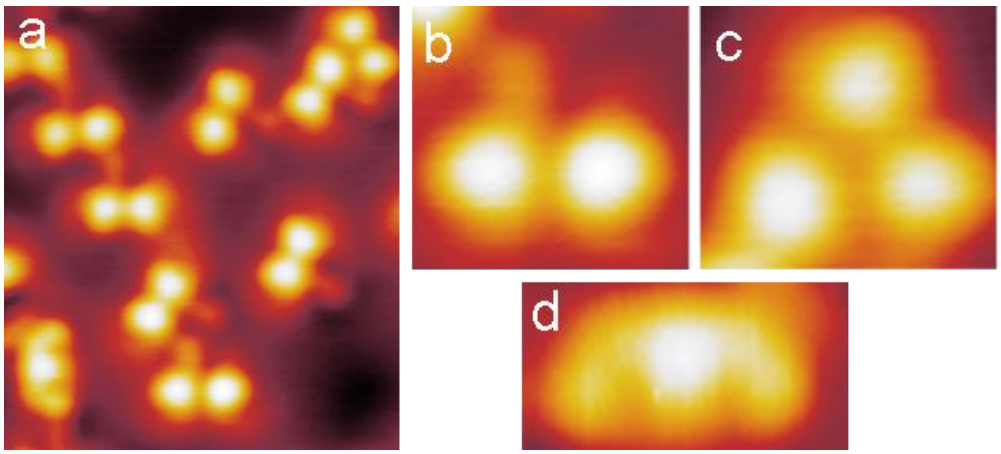

Figure 6.4: (a) Experimental STM images (5.0x5.0 nm^2) of CA complexes adsorbed on Au (111) in UHV conditions at low coverage. Detail of (a) *A-complex* (1.42x1.33 nm^2), (b) *B-complex* (1.44x1.33 nm^2) and (c) *chiral complex* (1.66x0.82 nm^2). *Vs*= 0.2 V, *It*= 700 pA

Three different family of structures have been identified: *A-complex*, composed by two bright lobe and a darker one, the *B-complex*, composed by three bright lobe forming a triangle and the *chiral complex*, also composed by three in-line bright lobe. The first two kind of complexes, especially the *A-complexes*, could be found in a great variety of shapes, i.e. two different *A-complex* which often differs by the relative orientation of the bright lobes (Figure 6.4). The *chiral complex* instead, has a central symmetry and could be found in three distinct shapes: the *E*, the *S* and the *Z* configuration.

To understand how are composed the observed structures at low coverages, and whether a gold adatoms plays any role, the system has been studied by means of DFT calculations.

6.4 Computational modelling

6.4.1 **Technical aspects**

Also for this chapter, DFT calculations were performed with the plane-wave pseudopotential package QUANTUM ESPRESSO using a GGA-PBE ultrasoft pseudopotentials. This time no van der Waals corrections has been applied. The wave function energy cut-off has been fixed at 408 eV and the forces were relaxed up to 0.26 eV/Å. Brillouin-zone sampling refers to a Monkhorst-Pack sampling and included two k-points in x and y directions, and only one in z direction, perpendicular to the surface.

The Au(111) surface was modelled with three layers allowing a vacuum (adlayer-surface) distance of ≈1.4 nm. The bottom layer of the surface has been kept fixed at the bulk Au calculated values to mimic the behaviour of the metal substrate. STM images were simulated within the Tersoff-Hamann approximation and elaborated to be comparable with experimental "constant current" STM image, as already explained in paragraph 4.4.1 . The images in

this paragraph were simulated at 0,2 V of bias, at an ILDOS value for the iso-surface of 4 x 10^{-3} nm^{-3}, lying at an average distance of approximately 0.5 nm from the first atomic layer. Ball models are rendered with the XCrySDen software packages.

6.4.2 **Singole CA molecule adsorption**

Also in this study the calculations started from a complete analysis of the adsorption of CA molecule on Au (111) surface. First, a gas-phase molecule (see Figure 6.1) has been optimised. Thereafter, the thiol group of the CA molecule has been deprotonated: it is indeed well known that thiols adsorb on gold in their deprotonated form.

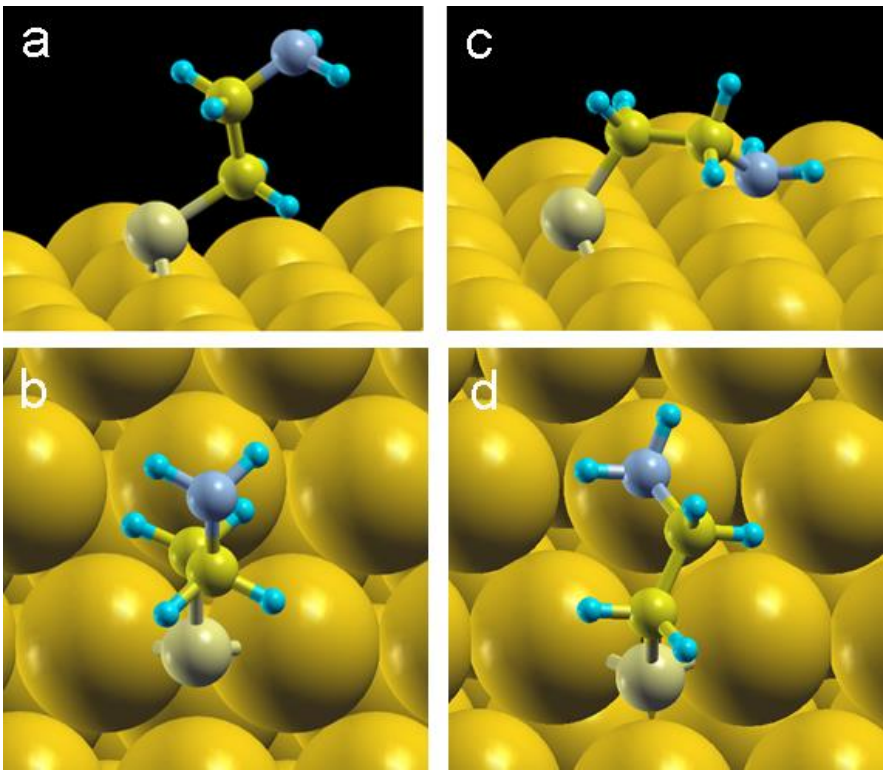

Figure 6.6: Stick and ball models for the two different adsorption geometry of the CA molecule on Au(111) substrate obtained by DFT calculation: (a) lateral and (b) top view of the *trans* configuration; (c) lateral and (d) top view of the *gauche* configuration.

Several adsorption geometries, as well as several adsorption sites have been tested. As result, the sulfur atom adsorbs in a "bridge" site; moreover, in perfect

agreement with the literature, two stable configurations have been found: the *trans*, with the pointing out of surface (Figure 6.6a and 6.6b) and the *gauche*, with the amine group interacting with a *on top* site of the Au surface (Figure 6.6c and 6.6d). Analysing the adsorption energies, the two conformers differ by a quantity of energy comparable with the thermal excitation at room temperature ($K_bT \cong 0.025$ eV), confirming their possible coexistence.

6.4.3 **The "A" and "B" complexes**

With concern to the *A-* and *B-complex*, various models have been tested, and those that show the best agreement with the experiment in terms of energetics and appearance of the STM images are shown in Figure 6.7 e 6.8.

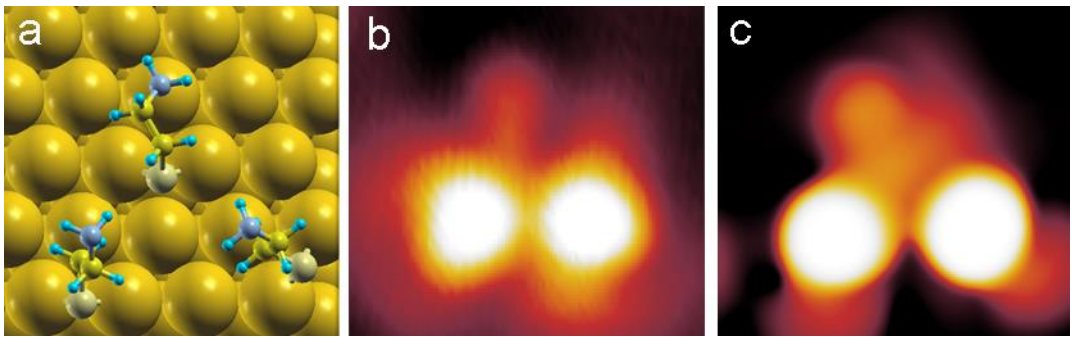

Figure 6.7: (a) stick and ball model for DFT-optimised *A-complex* and its relative (b) experimental and (c) simulated STM images. *A-complex* is composed by two *trans* and one *gauche* CA.

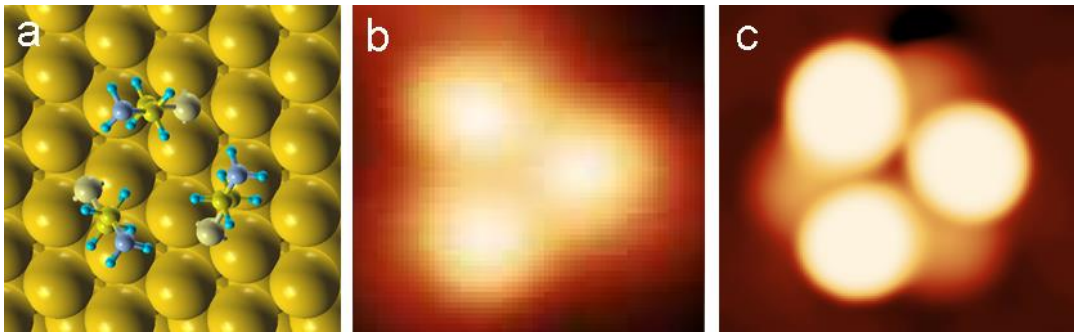

Figure 6.8: (a) stick and ball model for DFT-optimised *B-complex* and its relative (b) experimental and (c) simulated STM images. *B-complex* is composed by two *trans* and one *gauche* CA.

The *A-complex* is composed by two *trans* and a *gauche* molecule. In Figure 6.7a is proposed a probable adsorption configuration, but it's to be notice that the cysteamine has several degrees of freedom, especially concerning the orientation of the amine terminal group. This characteristic could justify the appearance variance experimentally observed for this family of complexes. The same considerations are useable also for the *B-complex*, that is composed by three trans molecules (Figure 6.8). Although the simulated STM images (Figure 6.7c and 6.8c) are in quite agreement with the experimental ones (Figure 6.7b and 6.8b), more calculations are planned in the near future to fully comprehend the adsorption and coordination mechanism.

6.4.4 **The "chiral" complexes**

Also the *chiral* complexes seems to be composed by three lobes, but behaves in a completely different way. They have only three possible and clearly distinct variants: the "*E*", the "*S*" and "*Z*" shapes, all symmetric. After having searched an explanation to this behaviour in the literature, the hypothesis of a coordinating gold adatom has been taken into account. Indeed, in two different works thiols, adsorbed in UHV conditions [37],[134], found structures, coordinated by a gold adatom, comparable with the *chiral* complexes (Figure 6.9). Also in that cases three different chirality have been identified.

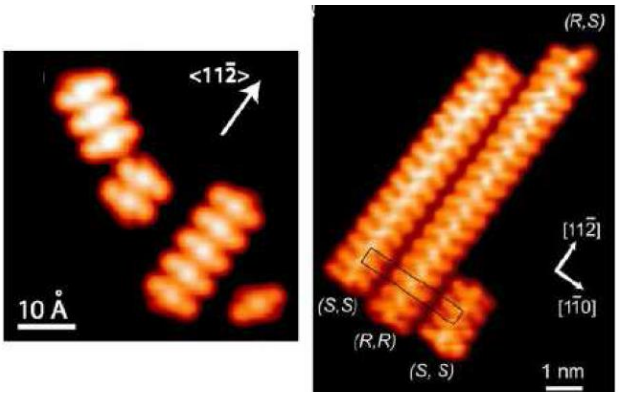

Figure 6.9: STM images of (left panel) CH_3S on Au(111) [37] and (right panel) C_3H_7SH on Au(111) [134].

Starting from these assumptions, a DFT model has been proposed and optimised for the "*E*", the "*S*" and "*Z*" variants (Figure 6.10, 6.11 and 6.12 respectively). The *chiral* complex is composed by two *gauche* molecules covalently bonded to an *on-top* site of the surface and to a gold adatom between them. The adatom is adsorbed on a *bridge* site. The relative orientation of the complex, with respect to the surface, is in good agreement with the experimental data. Moreover the simulated STM images are comparable with the experimental ones. Also in this case, more calculations have been planned to confirm the model.

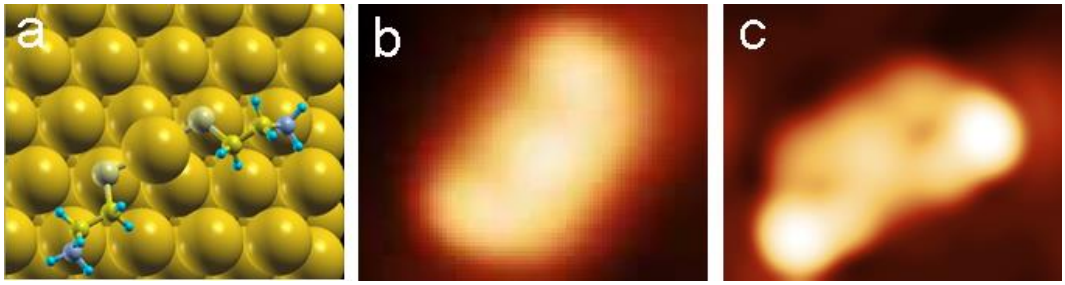

Figure 6.10: (a) stick and ball model for DFT-optimised "E" *chiral* complex and its relative (b) experimental and (c) simulated STM images.

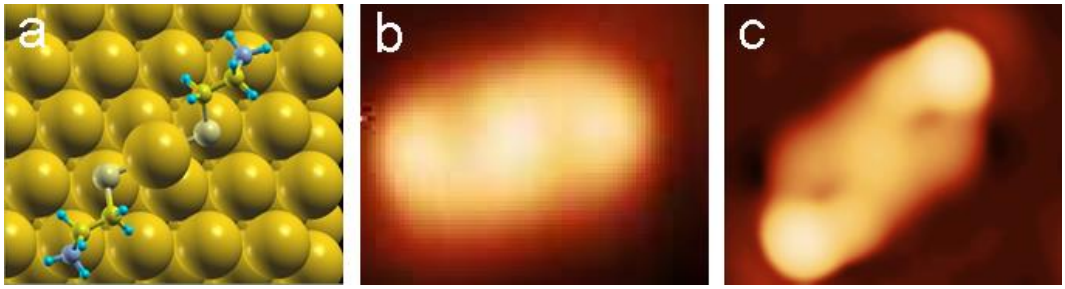

Figure 6.11: (a) stick and ball model for DFT-optimised "S" *chiral* complex and its relative (b) experimental and (c) simulated STM images.

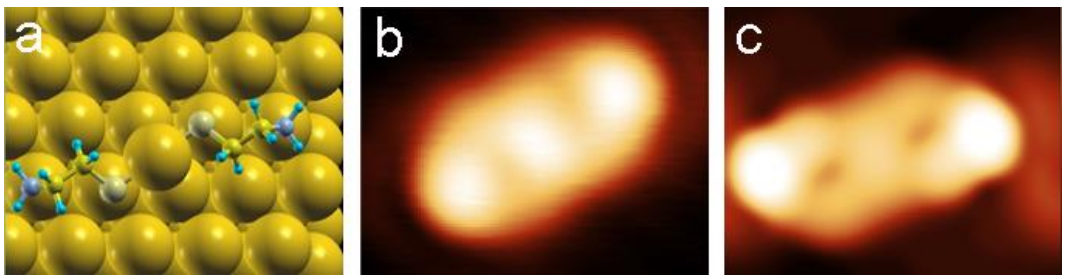

Figure 6.12: (a) stick and ball model for DFT-optimised "Z" *chiral* complex and its relative (b) experimental and (c) simulated STM images.

6.4.5 **Conclusions**

In this chapter the focus has been moved on the characterization of the adsorption of cysteamine (CA) on Au(111), a molecule that has been recently used to functionalise the surface by exposing its amino terminations out of the surface plane and strongly binding to the gold substrate via its sulfur atom. The monolayer phase had been already studied in literature, whereas STM investigations highlighted the existence, at low coverage, of some interesting structures composed by two or three molecules, never reported before. The theoretical study started with the adsorption of a single CA molecule on a gold (111) substrate and has confirmed the existence of two competitive adsorption configurations: *trans*, that adsorbs only throw the thiol group and *gauche*, that interact with the substrate with both terminal groups. Three different cluster species have been experimentally observed end theoretically modelled. The most common cluster is composed by two nearby *trans* and one *gauche* molecules. Another cluster is formed by three *trans* molecules and has a triangular shape. But the most interesting one is composed by two *gauche* molecules linked through a single gold adatom, adsorbed in a *bridge* site. This symmetric structure turns out to be chiral and can be found in three different shapes, the "S", the "Z" and the "E" conformation. In this case the presence of gold adatoms forces the symmetric adsorption geometry, not observed in the other two typologies of clusters.

CONCLUSIONS

In this thesis the gold (111) surface has been used as substrate for different self-assembly systems. In all of them, the surface itself and the native gold adatoms play a central role. They are spontaneously generated by the steps edges and the "soliton" of the herringbone reconstructions.

First, it has been shown that there is a mutual stabilization between a common, polar molecule, DMSO, and native, positively charged adatoms on the Au(111) surface. The existence of these adatoms, for which no directly related features are visible in the experimental data, is demonstrated by the agreement between the measured and simulated STM images, as well as by the observed stability of the complexes, that would have otherwise remained unexplained. These adatoms act as ionic linkers between the molecules, and this behaviour has been reported up to now only for alkali metal linkers. The observed mutual stabilization of DMSO and Au is likely related to the strong dipole moment of the molecule and the strong electronegativity of its constituents.

After that, the study of an amino-functionalized porphyrin (TAPP) on Au(111) is reported. At high coverage, the classic monolayer, already observed for other porphyrins, has been found. At low coverage instead, the surface is dominated by chain structures, stabilized by the interplay between the amino-amino and amino-gold interaction. Inside a chain each TAPP forms four hydrogen bonds and behaves alternately as H-acceptor or H-donor as a whole. Moreover, in STM images, most acceptors show at their centre a bright protrusion, which has been demonstrated to be induced by a gold adatom trapped beneath the molecule. This adatom coordinates the TAPP via two pyrroles and stabilises the

H-pyrroles preventing their deprotonation via voltage pulse. Moreover, studies at high annealing temperature of the monolayer reveal probably for the first time a self-metalation of a porphyrin on a gold substrate.

In the last chapter the adsorption at low coverage of cysteamine (CA) on Au(111) is reported. STM investigations highlighted indeed the existence of some interesting structures composed by two or three molecules. Three different cluster species have been experimentally observed end theoretically modelled. The most common one is composed by two nearby *trans* molecules and one *gauche*. Another cluster is formed by three *trans* molecules, adsorbed in a triangular shape. But the most interesting one is composed by two *gauche* molecules, bonded through a single gold adatom, adsorbed in a *bridge* site. This last structure is chiral and can be found in three different variants, the "S", the "Z" and the "E" conformation. In this case the presence of gold adatoms forces symmetric adsorption geometry, not observed in the other two types of clusters.

BIBLIOGRAPHY

[1] Born, M. and Oppenheimer R., Annalen der Physik **84**, 457 (1927).

[2] Hohenberg, P. and Kohn W. Phys. Rev. **136**, B864 (1964).

[3] Kohn, W. and Sham, L. J. Phys. Rev. **140**, A1133 (1965).

[4] Hartree, D. R., Proc. Cam. Phil. Soc. **24**, 89 (1928).

[5] Fock, V. Z., Z. Med. Phys **61**, 209 (1930).

[6] Ceperley, D. M. and Alder, B. J., Phys. Rev. Let. **45**, 566 (1980).

[7] Vosko, S. H.; Wilk, L. and Nusair, M. Can. J. Phys **58**, 1200 (1980).

[8] Perdew, J. P. and Zunger, A. Phys. Rev. B **23**, 5048 (1981).

[9] Perdew, J. P. Chevary, J. A.; Vosko, S. H.; Jackson, K. A.; Pederson, M. R.; Singh, D. J. and Fiolhais, C. Phys Rev. B **46**, 6671 (1992).

[10] Perdew, J. P.; and Wang, Y. Phys. Rev. B **45**, 13244 (1992).

[11] Perdew, J. P.; Burke, K. and Ernzerhof, M. Phys. Rev Let. **77**, 3865 (1996).

[12] Becke, A. D. Phys. Rev. A, **38**, 3098 (1988).

[13] Lee, C.; Yang, W.; Parr, R. G. Phys. Rev. B, **37**, 785 (1988).

[14] Dion, M.; Rydberg, H.; Schroeder, E.; Langreth, D. C. and Lundqvist, B. I. Phys. Rev. Lett. **92**, 246401 (2004).

[15] Thonhauser, T.; Cooper, V. R.; Li, S.; Puzder, A.; Hyldgaard, P. and Langreth, D. C. Phys. Rev. B **76**, 125112 (2007).

[16] Roman-Perez, G. and Soler, J.M. Phys. Rev. Let. **103**, 096102, (2009).

[17] Vydrov, O. A. and Voorhis, T. V. Phys. Rev. Let. **103**, 063004 (2009)

[18] Grimme, S. J. Comput. Chem. **27**, 1787 (2006).

[19] Grimme, S.; Antony, J. ; Ehrlich, S. and Krieg, H., J. Chem. Phys. **132**, 154104 (2010).

[20] Wu, Q. and Yang, W., J. Chem. Phys. **116**, 515 (2002)

[21] Ortmann, F.; Bechstedt, F. and Schmidt, W. G. Phys. Rev. B **73**, 205101 (2006)

[22] Tkatchenko, A. and Scheffler, M., Phys. Rev. Let. **102**, 073005 (2009)

[23] Monkhorst, H. J. and Pack, J. D., Phys. Rev. B **13**, 5188 (1976).

[24] Giannozzi, P.; Baroni, S.; Bonini, N.; Calandra, M.; Car, R.; Cavazzoni, C.; Ceresoli, D.; Chiarotti, G. L.; Cococcioni, M.; Dabo, I.; et al. J. Phys.: Condens. Matter **21**, 395502 (2009).

[25] Kokalj, A. Comput. Mat. Sci. **28**, 155 (2003)

[26] Binnig, G.; Rohrer, H.; Gerber, C. and Weibel, E. Phys. Rev. Let. **49**, 57 (1982).

[27] Bardeen, J. ; Phys. Rev. Let. **6**, 57 (1961).

[28] Tersoff, J. and Hamann, D. R., Phys. Rev. Let. **50**, 1998 (1983).

[29] Tersoff, J. and Hamann, D. R., Phys. Rev. B **31**, 805 (1985).

[30] Christmann, K. in Introduction to surface physical chemistry, cured by H. Baumgärtel, E. Franck, e W. Grunbein (Springer-Verlag, New York, 1991).

[31] Woodruff & Delchar, Modern techniques of surface science (1994).

[32] Love, J. C.; Estroff, L. A.; Kriebel, J. K.; Nuzzo, R. G. and Whitesides, G. M. Chem. Rev. **105**, 1103 (2005).

[33] Ulman, A. Chem. Rev. **96,** 1533, (1996).

[34] Selmo, S. Caratterizzazione dell'adsorbimento della cisteammina sulla superficie (111) dell'oro tramite microscopia a scansione a effetto tunnel a bassa temperatura, UniTs, Tesi di Laurea (2013)

[35] Barth, J. V.; Brune, H.; Ertl, G. and Behm, R. J. Phys. Rev. B, **42**, 15, 9307 (1990).

[36] Nasarimhan, S.; Vanderbilt, D. Phys. Rev. Let. **69**, 1564 (1992).

[37] Maksymovych, P.; Voznyy, O.; Dougherty, D. B.; Sorescu, D. C. and Yates Jr, J. T. Prog. Surf. Sci. **85**(5), 206 (2010).

[38] Zhu, R.; Pan, E.; Chung, P. W.; Cai, X.; Liew, K. M.; Buldum, A. Department of Civil Engineering, University of Akron, Akron (USA), 2006

[39] Gaylord Chemical Corporation. Dimethyl Sulfoxide (DMSO) Physical Properties. Technical report, 2005.

[40] David, N. A., Ann. Rev. of Pharm. **12,** 353 (1972).

[41] Santos, N. C. and Saldanha, C. Biochem. Pharm. **65**, 1035, (2003).

[42] Gaylord Chemical Corporation. Dimethyl Sulfoxide (DMSO) Health and Safety Information. Technical report, 2007.

[43] Yu, Z. W. and Quinn, P. J., Bio. Rep., **14**(6), (1995).

[44] Kvakovszky, G.; Mckim, A. and Moore. J. A Review of Microelectronic Manufacturing Applications Using DMSO-Based Chemistries. 2006.

[45] Heo, V; Song, K.W.; Choi, M.H.; Sung, T.H. and Moon, D.K. Sol. En. Mat. Sol. Cel. **95**(12), 3564 (2011).

[46] Keawprajak, A.; Koetniyom, W. and Piyakulawat, P., Org. Elec. **14**(1), 402 (2013).

[47] Senaratne, W.; Andruzzi, L. and Ober, C. K. Biomacromolecules **6**(5), 2427 (2005).

[48] Park, J.; Lee, S. and Lee, H. H. Org. Elec. **7**(5), 256 (2006).

[49] A. Jaworek, J. Mat. Sci. **42**(1), 266 (2006).

[50] Yang, Y. and Wang, C., Current Opinion in Colloid and Interface Science **14**(2), 135 (2009).

[51] Mamdouh, W.; Uji, H.; Ladislaw, J. S.; Dulcey, A. E.; Percec, V.; De Schryver, F. C.; De Feyter, S.; Leu, V. and Vagelos, D. J. Am. Chem. Soc. **128**(5), 317 (2006).

[52] Hodgson, A. and Haq, S. Surf. Sci. Rep. **64**(9), 381 (2009).

[53] Thiel, P. A. and Madey, T. E. Surf. Sci. Rep. **7,** 211 (1987).

[54] Sexton, B. A.; Avery, N. R. and Turney T. W., Surf. Sci. **124**, 162 (1983).

[55] Roelfs, B. et al., Surf. Sci. **380**, 441 (1997).

[56] Strader, M. L.; Garrett-roe, S.; Szymanski, P.; Shipman, S. T.; Johns, J. E.; Yang, A.; Muller E. and Harris, C. B., J. Phys. Chem. C **111**, 6880 (2008).

[57] Si, S. K. and Gewirth, A. A., J. Phys. Chem. B **111,** 10775 (2000).

[58] Ikemiya, N. and Gewirth, A. A. J. Phys. Chem. B **111,** 873 (2000).

[59] Schröter, C.; Roelfs, B.; Solomun, T., Surf. Sci. **380**, L441 (1997).

[60] Garwood, G. A., Jr; Hubbard, A. T., Surf. Sci. **118**, 223 (1982).

[61] Si, S. K.; Gewirth, A. A., Phys. Chem. Chem. Phys. **3**, 3325 (2001).

[62] Roelfs, B.; Schröter, C.; Solomun, T. A, Phys. Chem. **101**, 1105 (1997).

[63] Su, C.-C.; Faller, J. W., Inorg. Chem. **13**, 1734 (1974).

[64] Thomas, R.; Shoemaker, C. B.; Eriks, K., Acta Crystallog. **21**, 12 (1966).

[65] Leite, T. C. M.; de Barros, A. L. F.; Ferreira, G. B.; Guerra, A. C. O.; Turci, C. C., Int. J. Quantum Chem. **112**, 3421 (2012).

[66] Atak, K.; Engel, N.; Lange, K. M.; Golnak, R.; Gotz, M.; Soldatov, M.; Rubensson, J.-E.; Kosugi, N.; Aziz, E. F., ChemPhysChem **13**, 3106 (2012).

[67] Sze, K. H.; Brion, C. E.; Tronc, M.; Bodeur, S.; Hitchcock, A. P., Chem. Phys. **121**, 279 **(**1988).

[68] Stöhr, J., NEXAFS Spectroscopy, Springer Series in Surface Sciences - Springer-Verlag: Berlin, Vol. 25 (1992).

[69] Vanderbilt, D., Phys. Rev. B **41**, 7892 (1990).

[70] V. Barone, M. Casarin, D. Forrer, M. Pavone, M. Sambi, A Vittadini, J. Comput. Chem. **30**, 934 (2009).

[71] Casarin, M.; Marino, M. D.; Forrer, D.; Sambi, M.; Sedona, F.; Tondello, E.; Vittadini, A.; Barone, V.; Pavone, M., J. Phys. Chem. C **114**, 2144 (2010).

[72] Löwdin, P.-O., Phys. Rev. **97**, 1474 (1955).

[73] Shi, Z.; Lin, N., **131**, J. Am. Chem. Soc. 5376 (2009).

[74] Classen, T.; Fratesi, G.; Costantini, G.; Fabris, S.; Stadler, F. L.; Kim, C.; de Gironcoli, S.; Baroni, S.; Kern, K., Angew. Chem., Int. Ed. **44**, 6142 (2005).

[75] Pawin, G.; Wong, K. L.; Kim, D.; Sun, D.; Bartels, L.; Hong, S.; Rahman, T. S.; Carp, R.; Marsella, M. A, Angew. Chem., Int. Ed. **47**, 8442 (2008).

[76] Bauer, A.; Schier, A.; Schmidbaur, H., Acta Crystallog. C **51**, 2030 (1995).

[77] Knak Jensen, S. J.; Tang, T.-H.; Csizmadia, I. G., J. of Phys. Chem. A **107**, 8975 (2003).

[78] Cepellotti, A.; Peronio, A.; Marchini, S.; Abdurakhmanova, N.; Dri, C.; Africh, C.; Esch, F.; Comelli, G.; Peressi, M., J. of Phys. Chem. C **117**, 21196 (2013).

[79] Desiraju, G. R., Acc. Chem. Res. **29**, 441 (1996).

[80] Kervyn, S.; Kalashnyk, N.; Riello, M.; Moreton, B.; Tasseroul, J.; Wouters, J.; Jones, T. S.; De Vita, A.; Costantini, G.; Bonifazi, D., Angew. Chem., Int. Ed. **52**, 7410 (2013).

[81] Reimers, J.; Lü,X; Crossley, M. and Hush, N., J. Am. Chem. Soc. **117**(10), 2855 (1995).

[82] Auwärter, W.; Écija, D.; Klappenberger, F.; Barth, J. V. Nat. Chem. **7,** 105 (2015).

[83] Jurow, M.; Schuckman, A. E.; Batteas, J. D.; Drain, C. M. Coord. Chem. Rev. **254**, 2297 (2010).

[84] Otsuki, J. Coord. Chem. Rev. **254**, 2311 (2010).

[85] Mohnani, S.; Bonifazi, D. Coord. Chem. Rev. **254**, 2342 (2010).

[86] Yokoyama, T.; Yokoyama, S.; Kamikado, T.; Okuno, Y.; Mashiko, S. Nature **413**, 619 (2001).

[87] Fendt, L. A.; Stöhr, M.; Wintjes, N.; Enache, M.; Jung, T. a.; Diederich, F. Chem. - A Eur. J. **15**, 11139 (2009).

[88] Yokoyama, T.; Kamikado, T.; Yokoyama, S.; Mashiko, S. J. Chem. Phys. **121**, 11993 (2004).

[89] Grill, L.; Dyer, M.; Lafferentz, L.; Persson, M.; Peters, M. V; Hecht, S. Nat. Nanotechnol. **2**, 687 (2007).

[90] Lafferentz, L.; Eberhardt, V.; Dri, C.; Africh, C.; Comelli, G.; Esch, F.; Hecht, S.; Grill, L. Nat. Chem. **4**, 215 (2012).

[91] Heim, D.; Écija, D.; Seufert, K.; Auwärter, W.; Aurisicchio, C.; Fabbro, C.; Bonifazi, D.; Barth, J. V. J. Am. Chem. Soc. **132**, 6783 (2010).

[92] Heim, D.; Seufert, K.; Auwärter, W.; Aurisicchio, C.; Fabbro, C.; Bonifazi, D.; Barth, J. V. Nano Lett. **10**, 122 (2010).

[93] Haq, S.; Hanke, F.; Dyer, M. S.; Persson, M.; Iavicoli, P.; Amabilino, D. B.; Raval, R. J. Am. Chem. Soc. **133**, 12031 (2011).

[94] Pham, T. A.; Song, F.; Alberti, M. N.; Nguyen, M.-T.; Trapp, N.; Thilgen, C.; Diederich, F.; Stöhr, M. Chem. Commun. **51**, 14473 (2015).

[95] Venkataraman, L.; Klare, J. E.; Tam, I. W.; Nuckolls, C.; Hybertsen, M. S.; Steigerwald, M. L. Nano Lett. **6**, 458 (2006).

[96] Venkataraman, L.; Klare, J. E.; Nuckolls, C.; Hybertsen, M. S.; Steigerwald, M. L. Nature **442**, 904 (2006).

[97] Balducci, G.; Romeo, M.; Stener, M.; Fronzoni, G.; Cvetko, D.; Cossaro, A.; Dell'Angela, M.; Kladnik, G.; Venkataraman, L.; Morgante, A. J. Phys. Chem. C **119**, 1988 (2015).

[98] Kladnik, G.; Cvetko, D.; Batra, A.; Dell'Angela, M.; Cossaro, A.; Kamenetska, M.; Venkataraman, L.; Morgante, A. J. Phys. Chem. C **117**, 16477 (2013).

[99] Feng, Z.; Castellarin Cudia, C.; Floreano, L.; Morgante, A.; Comelli, G.; Dri, C.; Cossaro, A. Chem. Commun. **51**, 5739 (2015).

[100] Scudiero, L.; Barlow, D. E.; Hipps, K. W. J. Phys. Chem. B **104**, 11899 (2000).

[101] Yokoyama, T.; Yokoyama, S.; Kamikado, T.; Mashiko, S. J. Chem. Phys. **115**, 3814 (2001).

[102] Moresco, F.; Meyer, G.; Rieder, K.-H.; Ping, J.; Tang, H.; Joachim, C. Surf. Sci. **499**, 94 (2002).

[103] Auwärter, W.; Weber-Bargioni, a; Riemann, a; Schiffrin, a; Gröning, O.; Fasel, R.; Barth, J. V. J. Chem. Phys. **124**, 194708 (2006).

[104] Seufert, K.; Bocquet, M.-L.; Auwärter, W.; Weber-Bargioni, A.; Reichert, J.; Lorente, N.; Barth, J. V. Nat. Chem. **3**, 114 (2011).

[105] Mielke, J.; Hanke, F.; Peters, M. V.; Hecht, S.; Persson, M.; Grill, L. J. Am. Chem. Soc. **137**, 1844 (2015).

[106] Faraggi, M. N.; Jiang, N.; Gonzalez-Lakunza, N.; Langner, A.; Stepanow,

S.; Kern, K.; Arnau, A. J. Phys. Chem. C **116**, 24558 (2012).

[107] Boscoboinik, J. a.; Calaza, F. C.; Habeeb, Z.; Bennett, D. W.; Stacchiola, D. J.; Purino, M. a.; Tysoe, W. T. Phys. Chem. Chem. Phys. **12**, 11624 (2010).

[108] Yang, Z.; Corso, M.; Robles, R.; Lotze, C.; Fitzner, R.; Mena-Osteritz, E.; Bäuerle, P.; Franke, K. J.; Pascual, J. I. Am. Chem. Soc. Nano **8**, 10715 (2014).

[109] Meyer, J.; Nickel, A.; Ohmann, R.; Lokamani, L.; Toher, C.; Ryndyk, D. a.; Garmshausen, Y.; Hecht, S.; Moresco, F.; Cuniberti, G. Chem. Commun. **51**, 12621 (2015).

[110] Bellisario, D. O.; Jewell, A. D.; Tierney, H. L.; Baber, A. E.; Sykes, E. C. H. J. Phys. Chem. C **114**, 14583 (2010).

[111] Jewell, A. D.; Tierney, H. L.; Zenasni, O.; Lee, T. R.; Sykes, E. C. H. Top. Catal. **54**, 1357 (2011).

[112] Klappenberger, F.; Weber-Bargioni, a; Auwärter, W.; Marschall, M.; Schiffrin, A.; Barth, J. V. J. Chem. Phys. **129**, 214702 (2008).

[113] Röckert, M.; Franke, M.; Tariq, Q.; Ditze, S.; Stark, M.; Uffinger, P.; Wechsler, D.; Singh, U.; Xiao, J.; Marbach, H.; Steinrück, H.-P.; Lytken, O. Chemistry **20**, 8948–8953 (2014).

[114] Bürker, C.; Franco-Cañellas, A.; Broch, K.; Lee, T.-L.; Gerlach, A.; Schreiber, F. J. Phys. Chem. C **118**, 13659 (2014).

[115] González-Moreno, R.; Sánchez-Sánchez, C.; Trelka, M.; Otero, R.; Cossaro, A.; Verdini, A.; Floreano, L.; Ruiz-Bermejo, M.; García-Lekue, A.; Martín-Gago, J. A.; Rogero, C. J. Phys. Chem. C **115**, 6849 (2011).

[116] Goldoni, A.; Pignedoli, C. a.; Di Santo, G.; Castellarin-Cudia, C.; Magnano, E.; Bondino, F.; Verdini, A.; Passerone, D. Am. Chem. Soc. Nano **6**, 10800 (2012).

[117] Diller, K.; Klappenberger, F.; Marschall, M.; Hermann, K.; Nefedov, a.; Wöll, C.; Barth, J. V. J. Chem. Phys. **136**, 014705 (2012).

[118] Chen, M.; Feng, X.; Zhang, L.; Ju, H.; Xu, Q.; Zhu, J.; Gottfried, J. M.;

Ibrahim, K.; Qian, H.; Wang, J. J. Phys. Chem. C **114**, 9908 (2010).

[119] Papageorgiou, A. C.; Fischer, S.; Oh, S. C.; Sağlam, O.; Reichert, J.; Wiengarten, A.; Seufert, K.; Vijayaraghavan, S.; Ecija, D.; Auwärter, W.; Allegretti, F.; Acres, R. G.; Prince, K. C.; Diller, K.; Klappenberger, F.; Barth, J. V. ACS Nano **7**, 4520 (2013).

[120] Di Santo, G.; Castellarin-Cudia, C.; Fanetti, M.; Taleatu, B.; Borghetti, P.; Sangaletti, L.; Floreano, L.; Magnano, E.; Bondino, F.; Goldoni, A. J. Phys. Chem. C **115**, 4155 (2011).

[121] Kawasaki, M.; Sato, T.; Yoshimoto, T. Langmuir **16**, 540 (2000).

[122] Yam, C. M.; Pradier, C. M.; Salmain, M.; Marcus, P.; Jaouen, G. J. Colloid Interface Sci. **235**, 183 (2001).

[123] Cossaro, A., Puppin, M., Cvetko, D., Kladnik, G., Verdini, A., Coreno, M., ... & Morgante, A., J. Phys. Chem. Let. **2**(24), 3124 (2011).

[124] Jonkheijm, P.; Weinrich, D.; Schroder, H.; Niemeyer C. M. and Waldmann, H. Angew. Chem., Int. Ed. **47**, 9618 (2008).

[125] Rusmini, F.; Zhong Z. and Feijen, J. Biomacromolecules **8**, 1775 (2007).

[126] Michota, A., Kudelski, A., & Bukowska, J., Surf. Sci. **502**, 214 (2002).

[127] Zhang, J., Bilic̄, A., Reimers, J. R., Hush, N. S., & Ulstrup, J., J. Phys. Chem. B, **109**(32), 15355 (2005).

[128] Lee, S. Y.; Noh, J.; Ito, E.; Lee, H.; Hara, M., Jpn. J. Appl. Phys. **42**, 236 (2003).

[129] Cossaro, A., Dell'Angela, M., Verdini, A., Puppin, M., Kladnik, G., Coreno, M. and Floreano, L., J. Phys. Chem. C, **114**(35), 15011 (2010).

[130] Cossaro, A.; Mazzarello, R.; Rousseau, R.; Casalis, L.; Verdini, A.; Kohlmeyer, A.; Floreano, L.; Scandolo, S.; Morgante, A.; Klein, M. L.; et al. Science **321**, 943 (2008).

[131] Häkkinen, H., Nat. Chem. **4**, 443 (2012).

[132] Olmos-Asar, J. A.; Luduena, M.; Mariscal, M. M., Phys. Chem. Chem. Phys. **16**, 15979 (2014).

[133] Olmos-Asar, J. A.; Rapallo, A.; Mariscal, M. M., Phys. Chem. Chem. Phys. **13**, 6500 (2011).

[134] Voznyy, O., Dubowski, J. J., Yates Jr, J. T., & Maksymovych, P., J. Am. Chem. Soc. **131**(36), 12989 (2009).

[135] Feng, Z.; Velari, S.; Cossaro, A.; Castellarin-Cudia, C.; Verdini, A.; Vesselli, E.; Dri, C.; Peressi, M.; De Vita, A. and Comelli G., Am. Chem. Soc. Nano **9**(9), 8697 (2015).

[136] Feng, Z.; Velari, S.; Dri, C.; De Vita, A. and Comelli, G. "Nano-scale amphoterism of an amino-functionalized porphyrin on Au(111)", - in preparation

[137] Dri, C.; Velari, S.; Vesselli, E.; De Vita, A. and Comelli, G. "Sub-monolayer molecular complexes of cysteamine on Au(111)", – in preparation